Non-linear Interactions between Internal Wave Beams: Beyond the Traditional Approximation

by

Christian Chukwuebuka Ogbonna

A thesis
presented to the University of Waterloo
in fulfillment of the
thesis requirement for the degree of
Master of Mathematics
in
Applied Mathematics

Waterloo, Ontario, Canada, 2017

Abstract

The problem of nonlinear interactions of internal waves is solved using small-amplitude expansions beyond the traditional approximation; that is the horizontal component of the Earth's rotation vector is included in our analysis. It is shown that higher harmonics are generated from the reflection of propagating internal waves from a uniform slope due to the nonlinear interactions between the incident and the reflected first harmonic, this nonlinear interaction is restricted to the region where the two beams meet.

A criterion for critical reflection is derived in 2-D which depends on the horizontal orientation of the bottom slope in the horizontal geographical plane. The inclusion of the non-traditional $\tilde{f}$ term significantly changes the dynamics of internal waves in the ocean particularly for near inertial waves and for weak stratification due largely to the presence of inertial and sub-inertial waves which are absent in the traditional approximation.

We also discuss collisions of two beams with respect to two collision configurations (the same sign horizontal and the same sign vertical group velocity). Secondary beams with frequencies equal to the sum and in some cases the difference of the frequencies of colliding beams are generated in the vicinity of the collision region particularly for the same sign horizontal group velocity configuration. The predictions of the formation rule adopted in this thesis are illustrated by specific examples using Internal Gravity Wave (IGW) adapted numerical simulations.

Acknowledgements

I like to passionately express profound gratitude to my supervisor Prof. Kevin Lamb for his patience, motivation, enthusiasm, and immense knowledge which were vital to the completion of this thesis.

My sincere thanks also goes to Professors Marek Stastna and Michael Waite for being my defense committee and taking the time to read my thesis.

I would also like to thank the African Institute for Mathematical Science for providing foundational support which has been instrumental to my academic journey so far.

Last but not the least, I would like to thank my parents Martins Ogbonna and Celestina Ogbonna for supporting me spiritually throughout my life.

Dedication

To God and my parents.

Table of Contents

List of Figures

Chapter 1

Introduction

Internal waves (IWs) exist in stratified fluids and propagate under the influence of gravitational restoring forces. They are prevalent in the ocean where they are primarily generated by tide-topography interactions and by winds acting on the ocean surface. They occur in regions of rapidly changing water density with increasing depth. These density variations are usually associated with temperature variations. Principal internal tide generation sites are offshore ridges, transverse canyons, gullies, and prominent topography in shelf edges [29]. Internal tides are internal waves of tidal frequency.

Interacting internal gravity waves in stratified fluids have been studied for over a hundred years. They were first discovered by Nansen in the year 1902 [30]. The first property of internal waves to be observed was the presence of dominant frequencies in temperature records. Studies on internal wave spectra have shown that waves of the fundamental frequency are often the first to transport energy from the generation site. These fundamental frequencies are often characterised by distinguished peaks in the wave spectra [32].

Internal waves generated by tide-topography interaction have been observed throughout the world's oceans and they have been studied in detail in many locations, including near the Hawaiian Ridge which is known to be a very effective site for internal tide generation due to steep topography and barotropic tidal flows perpendicular to the ridge [5] and also in the South China Sea [7] and in the southern Bay of Biscay [1]. Internal tide generation in the Bay of Biscay have been studied by Gerkema *et al* [12] using a numerical linear hydrostatic internal-tide generation model, they found that internal-tide generation may occur in the seasonal thermocline and in the deep seasonally independent thermocline, the later is thought to be the main generation site. Laboratory experiments such as the oscillating bar experiment was used to show four columnated outgoing internal gravity wave beams widely known as the St. Andrew's cross (owing to the "X" pattern formed) [28].

A particular area of interest to oceanographers is the reflection of internal waves from ocean floor topography, due to its significant influence on energy transfer and mixing in the ocean. Energy transfer among internal waves contribute significantly to ocean mixing, hence influences climate change and nutrient cycles [9]. Mixing in the deep ocean is a mechanism by which heat from the upper layer of the ocean is transmitted to the abyssal cold waters - this process enhances the meridional overturning circulation [20].

Internal waves aid nutrient transport in the ocean and supports coastal ecosystems, they assist in the movement of nutrients to surface waters, this supports the growth of phytoplankton which is a fundamental component of oceanic food chain [6]. Oxygen circulation in the ocean is enhanced by the propagation of internal waves as is turbulent mixing on the continental shelf [6], [35]. Internal waves contribute significantly to the transport of momentum and energy within the ocean [16], [22].

Lien and Gregg [27] suggested that tide-topography interactions for supercritical topography generally results in the generation of beams along which shear and internal wave energy is highest and turbulence is most intense. Topographic slopes are considered supercritical when the slope of the topography is greater than the beam slope [25]. Other notable literature on this area of study include [13], [11], [26] and [14]. Superposition of individual plane waves propagating in a specified direction are called internal wave beams, they represent spatially compact and coherent regions of energy whose slope depends on frequency [5].

It is common place in the study of internal waves to assume that the rotation vector is parallel to gravity so that the effect of rotation is along the vertical. This is generally known as the Traditional Approximation. If we jettison this assumption, the horizontal component $\tilde{f} = 2\Omega\cos\theta$ (referred to as the non-traditional) is taken into account. This horizontal component of the Coriolis force has been observed (based on theory and numerical simulations) to be most effective for low-frequency internal waves in weakly stratified fluids [13].

With the non-traditional approximation the propagation of finite amplitude (nonlinear) internal gravity-wave beams in a uniformly stratified Boussinesq fluid with constant buoyancy frequency N_c has a dispersion relation

$$\omega^2 = N_c^2\cos^2\nu + (\tilde{f}\cos\nu + f\sin\nu)^2, \tag{1.1}$$

where ν is the angle the beam makes with the vertical and $f = 2\Omega\sin\theta$ [13].

An important consequence of the non-traditional approximation is that waves now exist at inertial ($\omega = |f|$) and sub-inertial frequencies ($\omega < |f|$). That is, the range of possible internal wave frequencies is increased [26]. Also change in the steepness of energy propagation is attributed to the $\tilde{f}$ term since the angle of energy propagation is influenced by the horizontal orientation of the waves in the geographical plane [11].

Non-traditional effects significantly changes the dynamics of near-inertial waves for weak stratification in a vertically bounded ocean, an example is the class of sub-inertial waves which becomes infinitely short as the wave frequency reaches the minimum frequency $\omega_{\min}$ [13]. These sub-inertial waves are dynamically important regardless of the smallness of their frequency range since the bulk of internal wave energy is at the inertial peak (region of transformation from sub-inertial to super-inertial). Fu, (1981) [8] noted that internal wave spectra is characterised by a strong peak at the inertial frequency implying the most energetic part of the spectrum, thus in general high frequency internal waves are the least energetic components of the internal wave spectrum. Graphical illustration of sub-inertial and super-inertial waves shows that the sub-inertial curve forms a direct smooth continuation of the super-inertial curve in the context of the non-traditional approximation [13].

The tendency for occurence of critical reflection in the real ocean was studied in [14], and a non-traditional criterion for critical reflection was determined, the criterion depends on the horizontal orientation of the bottom slope in the horizontal geographical plane. Critical reflection occurs when the group velocity is parallel to the bottom slope. Non-traditional $\tilde{f}$ term increases the steepness of the critical slope at low latitudes and decreases it in regions close to the inertial latitude [14].

An interesting feature in the propagation of internal gravity waves is that of reflection from uniform slopes and colliding beams. Internal waves undergo nonlinear interactions when they collide causing the generation of higher harmonic internal waves. Nonlinear wave-wave interactions transfers energy from large to small scales where wave breaking and mixing occurs hence the interest in these waves [10]. The reflection of beams or interaction of beams is an important mechanism for transferring energy to higher frequencies. Generation of higher harmonics from the nonlinear interaction of internal waves have been studied using numerical experiments [25] and [15] and with laboratory experiments [33] and [38].

A selection rule governing the generation of second harmonics was derived in [19] without considering rotation. A rule governing the generation of higher harmonics from colliding beams with full effect of rotation included was derived in a PhD dissertation by Chung-Hsiang [18]. In this thesis we have made modifications to this rule and extended it to account for cases involving wave beams of different frequencies.

1.1 Thesis Structure and Goals

Using a numerical model, the IGW model, the reflection of internal waves from a slopping bottom is explored. Secondly, interactions by colliding internal wave beams is treated. The primary goal of this thesis is to observe the generation of higher harmonics from the reflection and nonlinear interaction of internal wave beams. Further, this thesis demonstrates an understanding of propagating internal wave beams with the non-traditional approximation in a continuously stratified domain. In Chapter 2 detailed theoretical background which includes the equations of motion (rotated and non-rotated coordinates) and derivation of the dispersion relation, phase speed and group velocity of internal waves with and without the traditional approximation is presented. Brief explanation of the numerical model (IGW) including time stepping strategy, temporal discritization technique will be covered in Chapter 3. Simulation results will be illustrated in Chapter 4. Conclusion and suggestions for future work will be presented in the last chapter.

Chapter 2

Theoretical Background

2.1 Equations of Motion

Newton's second law of motion which relates the rate of change of momentum of a body to the force on it is the principal physical basis for predicting flow in the oceans. This is so because when this law is applied to a mass of fluid, it gives the momentum equation which governs fluid flow. The momentum equation is given by

$$\frac{\mathrm{D}\vec{u}}{\mathrm{D}t} = -\frac{1}{\rho}\vec{\nabla}p + \mathbf{g}, \tag{2.1}$$

where $\vec{u}$ is the velocity of a fluid particle, $\frac{\mathrm{D}\vec{u}}{\mathrm{D}t}$ is its acceleration, $\mathbf{g} = -\nabla(gz)$ is a conservative body force in this case gravity, the pressure gradient force per unit mass (PGF) is represented by the term $-\frac{1}{\rho}\vec{\nabla}p$ where ∇ is the $3D$ gradient operator, p and ρ represent pressure and density perturbations from a state of rest. Equation (2.1) is the momentum equation in a non-rotating reference frame. The material derivative $\frac{\mathrm{D}}{\mathrm{D}t}$ is the rate of change in time of its operand following the fluid element. It is related to the local time derivative $\frac{\partial}{\partial t}$ which describes the rate of change of the operand for a fixed point that coincides with the fluid element at a given instant in time by

$$\frac{\mathrm{D}\vec{u}}{\mathrm{D}t} = \frac{\partial}{\partial t} + \vec{u}\cdot\nabla. \tag{2.2}$$

An important concept in the study of fluid motion is rotation and the most natural frame from which to describe oceanic motions is one which rotates with the angular velocity,

$\vec{\Omega}$. In what follows we establish a relationship between an inertial reference frame and a rotating reference frame. A transformation rule exists between these two reference frames. Following [21], let $\frac{\mathrm{D}}{\mathrm{D}t}$ denote the rate of change in an inertial frame and $\frac{\mathrm{D}}{\mathrm{D}t_\Omega}$ its analogue in a frame rotating with the Earth's angular velocity $\vec{\Omega}$, then for any vector $\vec{A}$

$$\frac{\mathrm{D}\vec{A}}{\mathrm{D}t} = \frac{\mathrm{D}\vec{A}}{\mathrm{D}t_\Omega} + \vec{\Omega} \times \vec{A}, \tag{2.3}$$

Given $\vec{r}$ to be a position vector relative to the Earth's center, the velocities measured in the inertial ($\vec{u}$) and rotating reference frames ($\vec{u}_\Omega$) are then related by

$$\vec{u} = \vec{u}_\Omega + \vec{\Omega} \times \vec{r}, \tag{2.4}$$

this means that the velocity in the inertial frame $\vec{u}$ is equal to the sum of the velocity in the rotating frame and the velocity of the location of the fluid particle in the rotating frame relative to the non-rotating frame $\vec{\Omega} \times \vec{r}$, we have assumed that $\vec{u} = \frac{\mathrm{D}\vec{r}}{\mathrm{D}t}$ and $\vec{u}_\Omega = \frac{\mathrm{D}\vec{r}}{\mathrm{D}t_\Omega}$. Substituting $\vec{u}$ for $\vec{A}$ in equation (2.3) and using (2.4) gives

$$\frac{\mathrm{D}\vec{u}}{\mathrm{D}t} = \frac{\mathrm{D}\vec{u}_\Omega}{\mathrm{D}t_\Omega} + 2\vec{\Omega} \times \vec{u}_\Omega + \vec{\Omega} \times (\vec{\Omega} \times \vec{r}) + \frac{\mathrm{D}\vec{\Omega}}{\mathrm{D}t} \times \vec{r}. \tag{2.5}$$

The difference in the two reference frames consist of the three additional terms on the right-hand side of (2.5), Coriolis acceleration $2\vec{\Omega} \times \vec{u}_\Omega$, centrifugal force $\vec{\Omega} \times (\vec{\Omega} \times \vec{r})$ and the acceleration due to variations in the rotation rate $\frac{\mathrm{D}\vec{\Omega}}{\mathrm{D}t} \times \vec{r}$ (which is not regarded as significant for most oceanographic phenomena hence we ignore it going forward). With the aid of equation (2.5), we obtain the equation of motion in terms of the velocity $\vec{u_\Omega}$ and acceleration $\frac{\mathrm{D}\vec{u}_\Omega}{\mathrm{D}t_\Omega}$ with respect to the rotating frame of reference

$$\frac{\mathrm{D}\vec{u}_\Omega}{\mathrm{D}t_\Omega} + 2\vec{\Omega} \times \vec{u}_\Omega = -\frac{1}{\rho}\vec{\nabla}p + \mathbf{g} - \vec{\Omega} \times (\vec{\Omega} \times \vec{r})[21]. \tag{2.6}$$

The Centrifugal force is an apparent outward force that acts in planes perpendicular to the axis of rotation of the Earth and depends solely on the perpendicular distance from the rotation axis. It is a conservative force hence can be expressed as the gradient of a potential,

$$\vec{\Omega} \times (\vec{\Omega} \times \vec{r}) = \nabla \left(\frac{\Omega^2 r^2}{2} \right), \tag{2.7}$$

we absorb it in the gravity term (which we can now refer to as effective gravity $-\nabla\Pi$), so that

$$\Pi = gz - \frac{\Omega^2 r^2}{2}. \tag{2.8}$$

Equation (2.6) may now be expressed in the form

$$\frac{\mathrm{D}\vec{u}_\Omega}{\mathrm{D}t_\Omega} + 2\vec{\Omega} \times \vec{u}_\Omega = -\frac{1}{\rho}\vec{\nabla}p - \nabla\Pi. \tag{2.9}$$

Hence forth the subscript Ω is dropped and all equations are in the rotating reference.

2.1.1 Boussinesq Approximation

The Boussinesq approximation is useful in the analysis of many commonly occuring flows in nature, for instance the flow in the ocean. A major assumption of this approximation is that density does not vary significantly from a constant reference density ρ_0,

$$\rho = \rho_0 + \rho_v(x, y, z, t) \qquad |\rho_v| \ll \rho_0, \tag{2.10}$$

hence can be ignored except where ρ_v is multiplied by acceleration due to gravity g. Applying the Boussinnesq approximation to (2.9), let ρ_0 and $p_0(z)$ be the hypothetical static reference state of the density and pressure respectively, so that

$$\frac{dp_0(z)}{dz} = -\rho_0 g, \tag{2.11}$$

and define the pressure and density as the sum of an equilibrium value and a perturbation,

$$\begin{cases} \rho(\vec{x}, t) = \rho_0 + \rho_v(\vec{x}, t), \\ p(\vec{x}, t) = p_0(z) + p_v(\vec{x}, t), \end{cases} \tag{2.12}$$

where ρ_v and p_v are variations from the equilibrium state. With equations (2.11) and (2.12), the two terms on the right-hand side of the momentum equation (2.9) gives

$$-\frac{1}{\rho_0}\vec{\nabla}p - g\frac{\rho}{\rho_0}\mathbf{e}_z = -\frac{1}{\rho_0}\vec{\nabla}(p_0 + p_v) - \frac{g}{\rho_0}(\rho_0 + \rho_v)\mathbf{e}_z = -\frac{1}{\rho_0}\left[\frac{dp_0(z)}{dz}\mathbf{e}_z + \vec{\nabla}p_v\right] - \frac{g}{\rho_0}(\rho_0 + \rho_v)\mathbf{e}_z. \tag{2.13}$$

Subtracting the hydrostatic state (2.11) gives

$$-\frac{1}{\rho_0}\vec{\nabla}p - g\frac{\rho}{\rho_0}\mathbf{e}_z = -\frac{1}{\rho_0}\vec{\nabla}p_v - g\frac{\rho_v}{\rho_0}\mathbf{e}_z, \tag{2.14}$$

this is an indication that we can in fact replace ρ and p in equation (2.9) by the perturbation quantities ρ_v and p_v respectively. Since $\rho_v \ll \rho_0$, the left hand side of (2.9) gives

$$\rho\left[\frac{\mathrm{D}\vec{u}}{\mathrm{D}t} + 2\vec{\Omega}\times\vec{u}\right] \approx \rho_0\left[\frac{\mathrm{D}\vec{u}}{\mathrm{D}t} + 2\vec{\Omega}\times\vec{u}\right], \tag{2.15}$$

hence

$$\begin{aligned}\rho_0\left[\frac{\mathrm{D}\vec{u}}{\mathrm{D}t} + 2\vec{\Omega}\times\vec{u}\right] &= -\vec{\nabla}p - \rho g\mathbf{e}_z \\ &= -\vec{\nabla}p - \rho g\mathbf{e}_z.\end{aligned}$$

Equation (2.9) can now be expressed as

$$\frac{\mathrm{D}\vec{u}}{\mathrm{D}t} + 2\vec{\Omega}\times\vec{u} = -\vec{\nabla}p - \rho g, \tag{2.16}$$

where p and ρ have been divided by ρ_0 and the v subscripts have been dropped. See [31] and [21] for details.

Because of the need to balance any expansion or compression of fluid and the divergence or convergence of the velocity field we introduce the conservation of mass equation also known as the continuity equation

$$\frac{1}{\rho}\frac{\mathrm{D}\rho}{\mathrm{D}t} + \vec{\nabla}\cdot\vec{u} = 0. \tag{2.17}$$

Making the incompressibility approximation replaces equation (2.17) with

$$\vec{\nabla}\cdot\vec{u} = 0,$$

which says that the relative density changes $\frac{1}{\rho}\frac{\mathrm{D}\rho}{\mathrm{D}t}$ following a fluid particle are negligible compared to the velocity gradient terms.

Equations governing the motion of an incompressible, inviscid, continuously stratified fluid under the Boussinesq approximation on a rotating reference frame are,

$$\begin{cases} \nabla \cdot \vec{u} = 0 \\ \dfrac{\mathrm{D}\vec{u}}{\mathrm{D}t} + 2\vec{\Omega} \times \vec{u} = -\dfrac{1}{\rho_0}\vec{\nabla} p - g\dfrac{\rho}{\rho_0}\mathbf{e}_z \\ \dfrac{\mathrm{D}\rho}{\mathrm{D}t} = 0 \end{cases} \tag{2.18}$$

where $\vec{u} = (u, v, w)$, is the pressure, ρ_0 being the constant reference density, ρ and p are the departure of density and pressure from their constant reference state ρ_0 and $p(z)_0$. The density equation $\frac{\mathrm{D}\rho}{\mathrm{D}t} = 0$ comes from the non-diffusive heat equation and an incompressible equation of state [21].

2.1.2 Hydrostatic Approximation

The term hydrostatic approximation is a concept in geophysical fluid dynamics that is dependent on the thin sheet approximation that is, that the horizontal scale is large compared to the vertical scale, so that it is possible to express the vertical pressure gradient as the product of density times the gravitational acceleration.

For a more concrete explanation, consider the linearized equations of motion in two dimensions in terms of the pressure and density perturbation in a non-rotating frame given by

$$u_t = -p_x \tag{2.19}$$

$$w_t = -p_z - \rho g, \tag{2.20}$$

where p and ρ are the pressure and density perturbation and the pressure has been divided by a constant reference density. From equation (2.19) we find that

$$\frac{U}{T} = \frac{P}{L}, \tag{2.21}$$

where P is a scale for the pressure. If $H \ll L$ and from the thin sheet approximation $W \ll U$ we have

$$\frac{W}{T} \ll \frac{U}{T} = \frac{P}{L}. \tag{2.22}$$

Using $\frac{L}{H} \gg 1$ on the r.h.s of equation (2.22) (which does not change the order of the inequality) we find that

$$\frac{W}{T} \ll \frac{P}{L}\frac{L}{H} = \frac{P}{H}.$$

This means that the vertical acceleration term in equation (2.20) can be neglected since from the scaling analysis it is very small compared to the vertical pressure gradient term.

The hydrostatic approximation is thus

$$\frac{dp}{dz} = -\rho g, \tag{2.23}$$

for a constant density the pressure is given by

$$p(z) = p_{\text{atm}} + \rho g(\eta - z),$$

where $z = 0$ is the undisturbed surface and η represents the surface displacement. In the ocean where density varies with depth $p(z)$ is given by

$$p(z) = p_{\text{atm}} + \int_z^\eta \rho(z) g \, \mathrm{d}z. \tag{2.24}$$

Note that the pressure is equal to the atmospheric pressure p_{atm} at the free surface $z = \eta$.

2.2 f $\mathbf{f}_h$-plane

The Earth rotates from the west towards the east once in about 23 hours and 56 minutes with respect to the sun and has angular frequency

$$\Omega = \frac{2\pi}{23\text{hr}\,56\text{min}} \approx 7.31 \times 10^{-5} \text{ rad s}^{-1}. \tag{2.25}$$

We include the full effect of Coriolis forces and acceleration due to the vertical and horizontal component of the Earth's rotation, see figure (2.1). Let θ be the latitude and ϕ be the angle the x-axis is rotated with respect to the west-east direction. The z-axis is oriented vertically upwards with the origin at the unperturbed ocean surface and stays constant with respect to ϕ. The Coriolis parameters are given by

$$2\vec{\Omega} = 2\Omega(\cos\theta \sin\phi, \cos\theta\cos\phi, \sin\theta) = (f_h, f_g, f), \tag{2.26}$$

where

$$(2\vec{\Omega} \times \vec{u})_x = f_g w - f v \tag{2.27}$$

$$(2\vec{\Omega} \times \vec{u})_y = f u - f_h w \tag{2.28}$$

$$(2\vec{\Omega} \times \vec{u})_z = f_h v - f_g u \tag{2.29}$$

$f_g = 2\Omega\cos\theta\cos\phi$, $f_h = 2\Omega\cos\theta\sin\phi$, and $f = 2\Omega\sin\theta$. At $\phi = \frac{\pi}{2}$ and $\theta = \frac{\pi}{4}$, $f_g = 0, f = f_h = 1.0338 \times 10^{-4}$ rad s^{-1}. We will assume a small enough horizontal domain so that the curvature of the Earth is ignored. With this assumption we use the non-traditional approximation with no beta terms (ff_h-plane approximation).

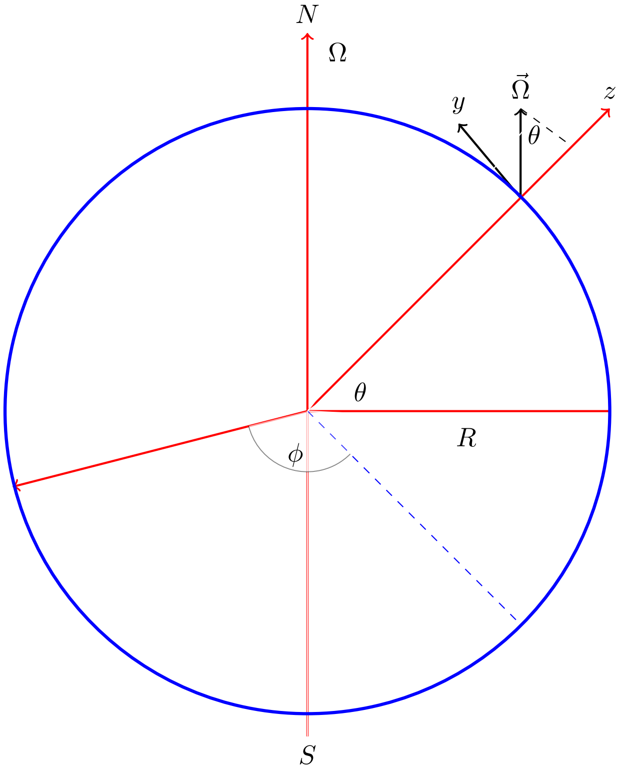

Figure 2.1: Local reference frame. The x-axis is perpendicular to the plane of the paper

2.3 Internal Gravity Waves

Internal gravity waves are waves that exist in density stratified fluid because of gravitational restoring forces acting on vertically displaced fluids. Barotropic or surface tides are driven by gravitational forces from the sun and moon, currents from these tides are independent of depth. They are ubiquitous in the ocean and are responsible for sea level rising and falling in the ocean. When barotropic currents interact with sloping bathymetry, fluid is forced to move in an up and down manner. These oscillations or disturbances occuring within the fluid medium propagate away as internal tides, that is internal waves of tidal frequency.

In what follows equations governing linear internal plane waves with and without the traditional approximation is derived. We also discuss properties of internal waves such as dispersion relation, phase speed, group velocity, and the nature of flow along surfaces of constant phase for the two regimes. We conclude the section by considering the more complex full nonlinear model (on a sphere) with the non-traditional approximation.

2.3.1 Phase Velocity and Group Velocity

In a continuously stratified fluid propagation of internal waves in the horizontal and vertical differ because the vertical direction is the direction the gravitational force acts in hence they are anisotropic. Dispersive waves lead to more complex phenomena precisely due to dispersion. In one-dimension waves are non-dispersive if the group velocity is independent of $|\vec{\kappa}|$ which implies that if $\frac{\mathrm{d}^2\omega}{\mathrm{d}k^2} = 0$ then we can have $\omega = ak + b$. If $b = 0$ the phase speed is also independent of k. In two and three dimensions the condition is more complicated as the group velocity has a direction and the requirement for non-dispersiveness is that $|\omega_{k_i k_j}| = 0$.

Wave energy travels with the group velocity not the phase velocity.

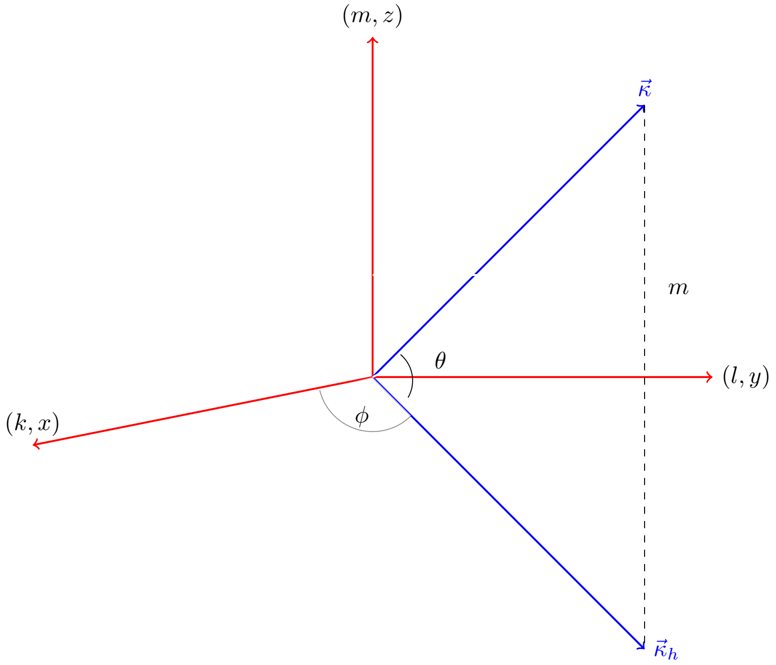

Figure 2.2: Schematic of wave numbers (k,l,m) and their projection on the x,y,z-plane, $\vec{\kappa} = (k,l,m)$, $\vec{\kappa}_h = (k,l), \theta =$ latitude, $\phi =$angle of rotation along the west-east direction.

2.3.2 Linear Internal Waves - Traditional Approximation

Following [21], the linearized equations of motion for a fluid on a rotating Earth with the Boussinesq approximation, assuming waves are propagating in the x direction so they are independent of y and with the traditional approximation are

$$u_t - fv = -p_x, \tag{2.30}$$

$$v_t + fu = 0, \tag{2.31}$$

$$w_t = -p_z + b, \tag{2.32}$$

$$u_x + w_z = 0, \tag{2.33}$$

$$b_t + N(z)^2 w = 0, \tag{2.34}$$

where p is the departure of pressure from its hydrostatic value (divided by the reference density), b is the buoyancy, $N(z)$ is the Brunt-Vaisala frequency, f is the Coriolis parameter, $\vec{u} = (u,v,w)$ is the fluid velocity.

Subtracting $\frac{\partial}{\partial x} \times$ (2.32) from $\frac{\partial}{\partial z} \times$ (2.30) gives

$$u_{tz} - fv_z - w_{tx} + b_x = 0. \tag{2.35}$$

Now taking $\frac{\partial}{\partial t} \times$ (2.35), gives

$$u_{ttz} - fv_{tz} - w_{ttx} + b_{tx} = 0. \tag{2.36}$$

Substituting (2.31) into (2.36) and differentiating by x we find that

$$u_{ttxz} + f^2 u_{xz} - w_{ttxx} + b_{txx} = 0. \tag{2.37}$$

Finally replacing u with w using the continuity equation and substituting for b from (2.34) gives the equations of motion in terms of the vertical velocity

$$\nabla^2 w_{tt} + f^2 w_{zz} + N(z)^2 w_{xx} = 0, \tag{2.38}$$

where the Laplacian is defined as $\nabla^2 = \frac{\partial^2}{\partial x^2} + \frac{\partial^2}{\partial z^2}$. Equation (2.38) is the wave equation for the vertical velocity in a continuously stratified rotating fluid.

If $N(z)$ is constant, the equation for w is linear we can look for plane wave solutions in an unbounded domain with amplitude parameter w_0 of the form,

$$w = w_0 \exp i(kx + mz - \omega t) = w_0 \exp i(\vec{\kappa} \cdot \vec{x} - \omega t), \tag{2.39}$$

where the real(or imaginary) part of (2.39) is intended. Substituting equation (2.39) into (2.38) we find that

$$m^2 = k^2 \frac{N^2 - \omega^2}{\omega^2 - f^2}, \tag{2.40}$$

where $\vec{\kappa} = (k, m)$, its magnitude $\kappa^2 = k^2 + m^2$. For bounded solutions in an infinite domain m and k must be real so that there are two possibilities either $f^2 < \omega^2 < N^2$ or $N^2 < \omega^2 < f^2$, thus giving a bounded range of possible internal wave frequencies.

Solving this expression for ω we obtain the dispersion relation

$$\omega^2 = \frac{N^2 k^2 + f^2 m^2}{k^2 + m^2} \tag{2.41}$$

which in terms of trigonometric expression can be expressed as

$$\omega^2 = N^2 \sin^2 \nu + f^2 \cos^2 \nu, \tag{2.42}$$

where ν is the angle the wave vector makes with the vertical, see figure (2.3). Thus the frequency of internal waves in a stratified fluid depends solely on the direction of the wavenumber vector.

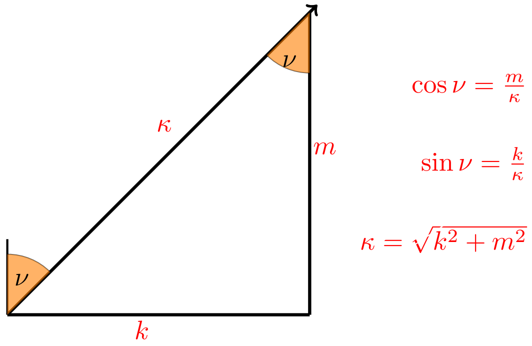

Figure 2.3: Schematic showing the relationship between the horizontal and vertical wave numbers in relation to the angle ν.

The phase velocity representing the velocity with which the phase of the wave propagates in space may be obtained from the diepsersion relation (2.41) as

$$\vec{v}_p = \frac{\omega}{\kappa}\frac{\vec{\kappa}}{\kappa} = \left(\frac{1}{k^2+m^2}\right)\left(\frac{N^2k^2+f^2m^2}{k^2+m^2}\right)^{\frac{1}{2}}(k,m). \tag{2.43}$$

Group velocity $\vec{v}_g$, the velocity at which wave packets (groups of waves) or wave energy propagates through space may be obtained from (2.41) as follows,

$$\vec{v}_g = \frac{\partial\omega}{\partial\vec{\kappa}} = (\omega_k, \omega_m) = (N^2-f^2)\frac{mk}{\omega(k^2+m^2)^2}(m,-k). \tag{2.44}$$

Notice that $\vec{\kappa}\cdot v_g = 0$, hence the group velocity is perpendicular to the wave vector. Also taking the dot product of equations (2.43) and (2.44) gives

$$\vec{v}_p \cdot \vec{v}_g = 0. \tag{2.45}$$

Thus energy traveling with the group velocity is perpendicular to the phase speed.

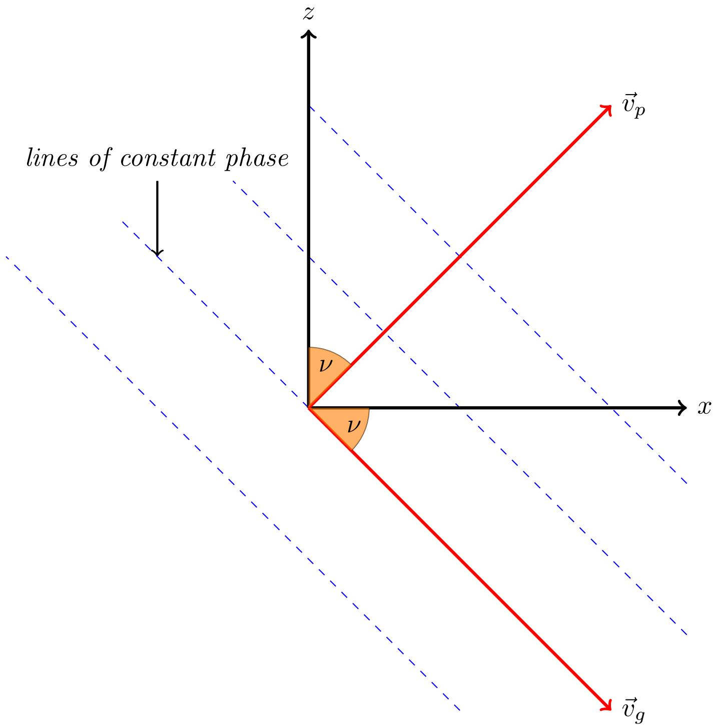

Figure 2.4: Schematic of an internal plane wave showing that the phase and group velocities are orthogonal and have opposite vertical components. The lines of constant phase lie at an angle ν to the horizontal and are parallel to the group velocity $\vec{v}_g$.

By assuming plane wave solution for the horizontal and vertical velocities and substituting same into the continuity equation (2.33) we see that the wave vector is perpendicular to the displacement of the particles (velocity vector), that is

$$\vec{\kappa} \cdot \vec{u} = 0 \tag{2.46}$$

this means that at any time, the fluid velocity is along the direction of the troughs and crests along which there is no perturbation pressure gradient, that is, these waves are transverse waves.

Further, if we make the hydrostatic approximation which is equivalent to assuming that the wave frequency ω is small compared to N then the dispersion relation (2.41) reduces to

$$\omega^2 = \frac{N^2 k^2 + f^2 m^2}{m^2}. \tag{2.47}$$

2.3.3 Nonlinear Internal Waves - Traditional Approximation

The goal of this section is to discuss the solutions of the linear equations from the previous section in relation to the nonlinear equations. Firstly, we show that the linear plane wave solution in an unbounded domain is an exact solution of the full nonlinear equations. Secondly, we show that a superposition of plane waves with parallel wave vectors is also a solution. The buoyancy frequency is assumed constant. Let u, v, w be the fluid velocity components. For a plane wave solution to the linear equations let

$$\begin{aligned} u &= u_0 \cos(kx + mz - \omega t + \alpha) \\ v &= f\frac{u_0}{\omega} \sin(kx + mz - \omega t + \alpha) \\ w &= -\frac{ku_0}{m} \cos(kx + mz - \omega t + \alpha) \end{aligned}$$

where u_0, v_0, w_0 are amplitude parameters, α is a phase shift.

Consider the full nonlinear equations

$$u_t + (\vec{u} \cdot \nabla)u - fv = -p_x \tag{2.48}$$

$$v_t + (\vec{u} \cdot \nabla)v + fu = 0 \tag{2.49}$$

$$w_t + (\vec{u} \cdot \nabla)w = -p_z + b \tag{2.50}$$

$$u_x + w_z = 0 \tag{2.51}$$

$$b_t + (\vec{u} \cdot \nabla)b + N^2 w = 0, \tag{2.52}$$

where u,v and w are the fluid velocity components in the x, y and z directions respectively, $b = -\rho g$ is the buoyancy, p is the departure of pressure from its background state divided by a constant reference density ρ_0 and $N^2 = -\frac{g}{\rho_0}\frac{\mathrm{d}\bar{\rho}}{\mathrm{d}z}$ is a constant. To show that the solution of the linear equations are also solutions of the nonlinear equations suffices to show that the nonlinear terms in equations (2.48) - (2.52) are equal to zero.

Now $\vec{u}$ is proportional to $\cos(kx + mz - \omega t + \alpha)$ and $\vec{\nabla} u$ is proportional to $\vec{k}\sin(kx + mz - \omega t + \alpha)$, we saw from equation (2.46) that $\vec{u}$ is perpendicular to $\vec{k}$. We thus have that $\vec{u} \cdot \vec{\nabla} u = 0$. Similarly $\vec{u} \cdot \vec{\nabla} v = 0$ and $\vec{u} \cdot \vec{\nabla} w = 0$. The buoyancy b like the fluid velocity is constant along lines of constant phase so that the nonlinear term in the density equation is again zero.

To show that a superposition of plane waves with parallel wave vectors is also a solution, we first note that parallel wave vectors implies the same wave frequency. Let

$$u = a_1 \cos(\vec{k}_1 \cdot \vec{x} - \omega t + \alpha) + a_2 \cos(k_2 \cdot \vec{x} - \omega t + \alpha) \tag{2.53}$$

and

$$\vec{\nabla} u = a_1 \vec{k}_1 \sin(\vec{k}_1 \cdot \vec{x} - \omega t + \alpha) + a_2 \vec{k}_2 \sin(\vec{k}_2 \cdot \vec{x} - \omega t + \alpha). \tag{2.54}$$

From equations (2.53) and (2.54) we find that

$$\vec{u} \cdot \vec{\nabla} u = \vec{u} \cdot a_1 \vec{k}_1 \sin(\vec{k}_1 \cdot \vec{x} - \omega t + \alpha) + \vec{u} \cdot a_2 \vec{k}_2 \sin(\vec{k}_2 \cdot \vec{x} - \omega t + \alpha) = 0, \tag{2.55}$$

because $u = \sum a_j \exp i(\vec{k}_j \vec{x} - \omega t)$ we similarly have $\vec{u} \cdot \vec{\nabla} u = 0$, provided all the k_j are parallel. This is also true for v, $w = \sum a_j \exp i(\vec{k}_j \vec{x} - \omega t)$. Thus exact solutions of the linear equations are also solutions of the nonlinear equations.

2.3.4 Linear Rotated Coordinates - Traditional Approximation

To introduce the general expression for an internal wave beam we consider two-dimensional plane waves in a coordinate system with the x-z axis rotated counterclockwise by an angle ϕ which is the angle the wave vector makes with the vertical, see figure (2.5). With this rotated coordinate we are on a reference frame in which the flow is along the x-axis so that z is perpendicular to the phase lines. Based on this the linearized equations of motion for a fluid on a rotating Earth with the Boussinesq approximation and with the traditional approximation are [21],

$$u_t - f \cos\phi \, v = -p_x + b \sin\phi, \tag{2.56}$$

$$v_t + f \cos\phi \, u - f \sin\phi \, w = -p_y, \tag{2.57}$$

$$w_t + f \sin\phi \, v = -p_z + b \cos\phi, \tag{2.58}$$

$$u_x + v_y + w_z = 0, \tag{2.59}$$

$$b_t + N(z)^2 \sin\phi \, u + N(z)^2 \cos\phi \, w = 0, \tag{2.60}$$

where p is the departure of pressure from its hydrostatic value (divided by reference density), b is the buoyancy, $N(x, z)$ is the Brunt-Vaisala frequency, f is the Coriolis parameter, $\vec{u} = (u, v, w)$ is the fluid velocity.

To eliminate the pressure from equations (2.56) and (2.58) we subtract $\frac{\partial}{\partial x} \times$ (2.58) from $\frac{\partial}{\partial z} \times$ (2.56), to get

$$u_{tz} - w_{tx} - f\cos\phi\, v_z - f\sin\phi\, v_x = b_z\sin\phi - b_x\cos\phi. \tag{2.61}$$

Taking the time derivative of equation (2.61) gives

$$u_{ttz} - w_{ttx} - f\cos\phi\, v_{zt} - f\sin\phi\, v_{xt} = b_{zt}\sin\phi - b_{xt}\cos\phi. \tag{2.62}$$

To eliminate v and b we substitute equations (2.57) and (2.60) into (2.62) and simplify to get

$$\begin{aligned} &u_{ttz} - w_{ttx} - f^2\cos\phi\sin\phi(w_z - u_x) + N^2\cos\phi\sin\phi(w_z - u_x) \\ &+ f^2(\cos^2\phi\, u_z - \sin^2\phi\, w_x) - N^2(\cos^2\phi\, w_x - \sin^2\phi\, u_z) = 0 \end{aligned} \tag{2.63}$$

Taking the x-derivative of (2.63) and using the incompressibility condition by letting $u_x = -w_z$ we get an equation for the vertical velocity in a continuously stratified rotating fluid,

$$\nabla^2 w_{tt} + 2\cos\phi\sin\phi(f^2 - N^2)w_{xz} + (N^2\cos^2\phi + f^2\sin^2\phi)w_{xx} + (N^2\sin^2\phi + f^2\cos^2\phi)w_{zz} = 0 \tag{2.64}$$

where the Laplacian is defined as $\nabla^2 = \frac{\partial^2}{\partial x} + \frac{\partial^2}{\partial z}$. Simplifying further we obtain

$$\nabla^2 w_{tt} + f^2\left[\cos\phi\frac{\partial}{\partial x} + \sin\phi\frac{\partial}{\partial z}\right]^2 w + N^2\left[\sin\phi\frac{\partial}{\partial z} - \cos\phi\frac{\partial}{\partial x}\right]^2 w = 0. \tag{2.65}$$

If $N(x, z)$ is constant then in an unbounded domain, we can assume plane wave solution and taking $\phi = \nu$ so that $k = 0$ and the x-axis is oriented along the phase lines,

$$w = w_0 \exp i(mz - \omega t). \tag{2.66}$$

Substituting equation (2.66) into (2.65) we find that

$$\omega^2 = N^2\sin^2\nu + f^2\cos^2\nu, \tag{2.67}$$

where ν is the angle the beam makes with the horizontal, from equation (2.67) we observe that if $\nu = 0$ the wave frequency ω is $|f|$ and if $\nu = \frac{\pi}{2}$ frequency is N, in this case the wave vector is horizontal so fluid parcels are oscillating up and down with frequency N where "up" is in the direction opposite to gravity. Notice that this is the same equation given by (2.42), thus rotating the coordinates does not change the dispersion relation.

2.3.5 Internal Wave Beams under the Traditional Approximation

Consider the case for which $k = 0$ so that the x-axis is oriented along lines of constant phase then the flow is independent of x. Assuming the flow is independent of y then from incompressibilty assumption we find that $w = 0$, this is so because the fluid velocity is along phase lines and the coordinate system has x lying along the lines of constant phase. In this section the buoyancy frequency is taken constant. The full nonlinear equations of motion with the traditional approximation under the afforementioned conditions are

$$u_t + (\vec{u} \cdot \nabla)u - f \cos\phi \, v = b \sin\phi, \tag{2.68}$$

$$v_t + (\vec{u} \cdot \nabla)v + f \cos\phi \, u = 0, \tag{2.69}$$

$$f \sin\phi \, v = -p_z + b \cos\phi, \tag{2.70}$$

$$b_t + (\vec{u} \cdot \nabla)b + N^2 \sin\phi \, u = 0, \tag{2.71}$$

Under these assumptions the nonlinear terms are zero, to see this

$$(\vec{u} \cdot \nabla)u = uu_x + vu_y + wu_z \tag{2.72}$$

$$= 0 \text{ (since the flow is independent of } x \text{ and } y\text{, and } w = 0). \tag{2.73}$$

Similarly $(\vec{u} \cdot \nabla)v = 0$ and $(\vec{u} \cdot \nabla)b = 0$. Thus the nonlinear equations are given by

$$u_t - f \cos\phi \, v = b \sin\phi, \tag{2.74}$$

$$v_t + f \cos\phi \, u = 0, \tag{2.75}$$

$$f \sin\phi \, v = -p_z + b \cos\phi, \tag{2.76}$$

$$b_t + N^2 \sin\phi \, u = 0, \tag{2.77}$$

To obtain an equation in terms of u from (2.74)-(2.77) we proceed as follows: Take $\frac{\partial}{\partial t} \times$ (2.74) to get

$$u_{tt} - f \cos\phi \, v_t - b_t \sin\phi = 0, \tag{2.78}$$

Substituting the expressions for v_t and b_t from equations (2.75) and (2.77) respectively into (2.78) gives

$$u_{tt} + (N^2 \sin^2\phi + f^2 \cos^2\phi)u = 0. \tag{2.79}$$

This has solutions of the form

$$u(z, t) = F(z) \cos(mz - \omega t), \tag{2.80}$$

where $F(z)$ is an arbitrary function representing internal wave beam envelope. So, the fluid horizontal velocity varies along the vertical but is fixed along the horizontal direction which coincides with the direction of fluid flow (constant phase lines). Substituting (2.80) into (2.79) gives the dispersion relation

$$\omega^2 = N^2 \sin^2 \phi + f^2 \cos^2 \phi, \tag{2.81}$$

where ϕ is the angle the beam makes with the horizontal, which is the same as in the linear case. The frequency and wave numbers are independent of one another and the wave frequency determines the propagation angle of the waves. Internal wave beams are superposition of plane waves with parallel wave vectors propagating in a specified direction, they represent spatially compact and coherent regions of energy whose slope depends on frequency. The plane waves that make up a wave beam all possess the same frequency otherwise different wave components will travel in different directions (since the slope of the beams depends on frequency) resulting in a scattered wave profile.

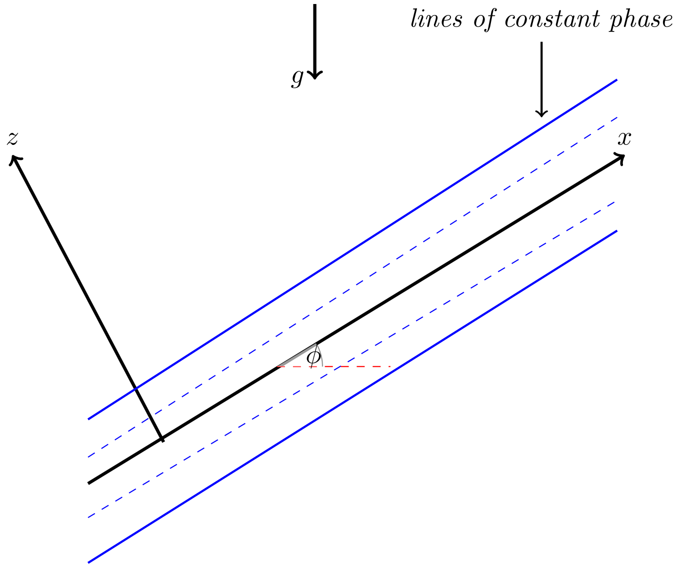

Figure 2.5: A coordinate system with the x-z axis rotated counterclockwise by an angle ϕ, the fluid particle velocity is along lines of constant phase parallel to the x-axis .

2.3.6 Linear Internal Waves - Non-traditional Approximation

In this section and the next we focus on linear and nonlinear equations of motion involving the horizontal component of rotation $\tilde{f}$ known as the non-traditional approximation. From these equations of motion we will derive expressions for the phase and group velocity of wave beams. As stated in [13] the linear internal wave equation representing the motion of a density-stratified fluid on the non-traditional ff_h-plane under the Boussinesq approximation is given by

$$u_t - fv + \tilde{f}w = -p_x, \tag{2.82}$$

$$v_t + fu = -p_y, \tag{2.83}$$

$$w_t - \tilde{f}u = -p_z + b, \tag{2.84}$$

$$u_x + v_y + w_z = 0, \tag{2.85}$$

$$b_t + N^2 w = 0, \tag{2.86}$$

where N, p, ρ, b, f, u, v, w all retain their usual meaning, x, y represent the west-east and south-north directions respectively and z is the positive upward vertical and has its origin at the unperturbed ocean surface. Here $\tilde{f}$ represents the horizontal component of the Coriolis parameter. Following [13] we try to reduce equations (2.82) - (2.86) to an equation for w.

Taking $\partial_t \times$ (2.84) and using (2.86) we find that

$$w_{tt} + N^2 w - \tilde{f}u_t = -p_{zt}. \tag{2.87}$$

Taking $\partial_t \times$ (2.85) and using $\partial_x \times$ (2.82) and $\partial_y \times$ (2.83) we obtain

$$w_{zt} = \nabla_h^2 p - fv_x + \tilde{f}w_x + fu_y. \tag{2.88}$$

Taking $\partial_{tz} \times$ (2.88) and substituting for p from (2.87) gives

$$\nabla^2 w_{tt} + N^2 \nabla_h^2 w = \tilde{f}\nabla_h^2 u_t - f(v_{xtz} - u_{ytz}) + \tilde{f}w_{xtz}, \tag{2.89}$$

substituting for v_t and u_t from (2.82) and (2.83) we find that

$$\begin{aligned}
\text{L.H.S} &= \tilde{f}\nabla_h^2 u_t - f[(-p_y - fu)_{xz} - (-p_x + fv - \tilde{f}w)_{yz}] + \tilde{f}w_{xtz}, \\
&= \tilde{f}\nabla_h^2 u_t + f^2(u_x + v_y)_z - f\tilde{f}w_{yz} + \tilde{f}w_{xtz} \\
&= \tilde{f}\nabla_h^2 u_t + \tilde{f}w_{xtz} - f^2 w_{zz} - f\tilde{f}w_{yz} \\
&= \tilde{f}u_{yyt} - \tilde{f}v_{xyt} - f^2 w_{zz} - f\tilde{f}w_{yz} \qquad \text{after applying (2.85)} \\
&= \tilde{f}(-p_{xy} + fv_y - \tilde{f}w_y)_y - \tilde{f}(-p_{yx} - fu_x)_y - f^2 w_{zz} - f\tilde{f}w_{yz} \\
&= \tilde{f}f(v_{yy} + u_{xy}) - \tilde{f}^2 w_{yy} - f^2 w_{zz} - f\tilde{f}w_{yz} \\
&= -(\tilde{f}^2 w_{yy} + f^2 w_{zz} + 2\tilde{f}f w_{yz}) \\
&= -(\vec{f}\cdot\nabla)^2 w,
\end{aligned}$$

we now have an equation for w given by

$$\nabla^2 w_{tt} + (\vec{f}\cdot\nabla)^2 w + N^2\nabla_h^2 w = 0, \tag{2.90}$$

where $\vec{f} = (0, \tilde{f}, f)$.

We again assume plane wave solutions with amplitude parameter w_0 and with all the properties previously considered

$$w = w_0 \exp i(kx + ly + mz - \omega t) = w_0 \exp i(\vec{\kappa}\cdot\vec{x} - \omega t)$$

substituting into equation (2.90) we find that

$$\omega^2 = \frac{N^2\kappa_h^2 + (l\tilde{f} + mf)^2}{\kappa^2} = \frac{N^2\kappa_h^2 + 2f\tilde{f}lm + f^2m^2 + \tilde{f}^2l^2}{\kappa^2} \tag{2.91}$$

Assuming that the y-axis is oriented in the direction of the horizontal component of the wave vector this gives

$$\omega^2 = \frac{N^2l^2 + 2f\tilde{f}lm + f^2m^2 + \tilde{f}^2l^2}{l^2 + m^2}. \tag{2.92}$$

If $l = 0$ that is the wave is propagating in the east-west direction, then the $\tilde{f}$ terms drop out, that is the non-traditional terms have no effect, and hence the non-traditional terms has the largest effect on waves that are propagating in the north-south direction.

For purpose of uniformity we suppose that the x-axis is oriented in the north-south direction and the y-axis is along the east-west direction we can then interchange the roles of k and l in equation (2.92) so that the dispersion relation becomes

$$\omega^2 = \frac{N^2k^2 + 2f\tilde{f}km + f^2m^2 + \tilde{f}^2k^2}{k^2+m^2} = N^2\sin^2\nu + (\tilde{f}\sin\nu + f\cos\nu)^2, \tag{2.93}$$

where ν is the angle the beam makes with the horizontal. Again we see that it is possible to express the dispersion relation independent of the wave numbers, thus frequency is dependent on direction and not the wavenumber vector. The group velocity is given by

$$\vec{v}_g = (\omega_k, \omega_m) = \frac{1}{\omega(k^2+m^2)^2}\big((N^2 + \tilde{f}^2 - f^2)mk + f\tilde{f}(m^2-k^2)\big)(m, -k), \tag{2.94}$$

and the phase velocity is

$$\vec{v}_p = \frac{1}{(k^2+m^2)}\left(\frac{N^2k^2 + 2f\tilde{f}km + f^2m^2 + \tilde{f}^2k^2}{k^2+m^2}\right)^{\frac{1}{2}}(k, m) \tag{2.95}$$

Figure (2.6) shows the difference between the traditional and non-traditional regime, while the traditional branch is symmetric about the x-axis, the non-traditional branch is not. The non-traditional branch is seen to extend a little further to the left than the traditional branch suggesting the presence of inertial and sub-inertial frequencies. In the traditional regime $|f|$ is the lower bound of the frequency domain. While in the non-traditional regime $\omega_{\text{min}} < f$ constitutes the lower bound.

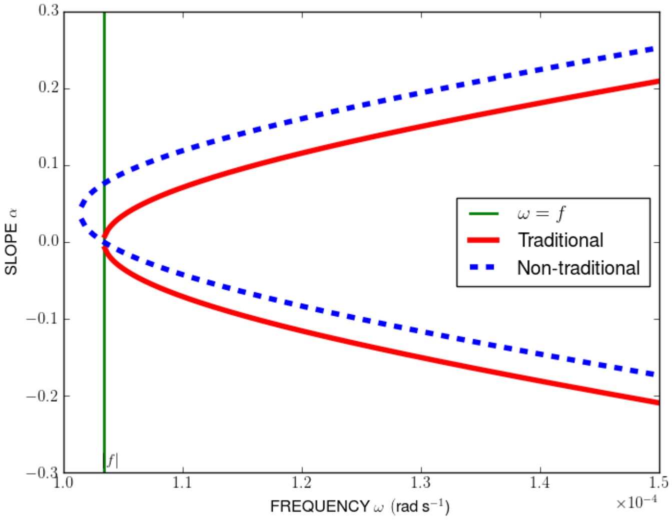

Figure 2.6: Schematic illustrating the difference between the dispersion relation with and without the traditional approximation for the following parameter values $N = 5.4 \times 10^{-4}$ rad s^{-1}, $\theta = \frac{\pi}{4}$, $f = f_h = 1.0338 \times 10^{-4}$ rad s^{-1}. The upper half represents slopes oriented northward and the lower half are slopes oriented southward. The green line seperates super-inertial and sub-inertial frequencies.

2.3.7 Full Nonlinear Wave Equation

In this section we introduce a perturbation expansion up to order ϵ^2 which is used to determine expression for primary wave, mean field and second harmonic internal wave beams. The section starts off with the full nonlinear equations, we then consider a two-dimensional incompressible flow which makes it possible to introduce a stream function. With these equations we will study the interaction of two beams propagating in different directions which includes a beam reflecting off a boundary.

We make use of a coordinate system with the x-axis in the direction of propagation so in this coordinate system the wave field is independent of y. The Coriolis parameters are

$$(f_h, f_g, f) = 2\Omega(\cos\theta \sin\phi,\, \cos\theta\cos\phi,\, \sin\theta), \tag{2.96}$$

where f_g and f_h are proportional to $\tilde{f}$, we assume the f-plane approximation so that latitude θ is fixed.

Following [11], the full nonlinear equations of motion for an incompressible continuously stratified fluid under the Boussinesq approximation on the non-traditional ff_h-plane taking into account the spherical nature of the Earth are

$$u_t + (\vec{u}\cdot\nabla)u - fv + f_g w = -p_x \tag{2.97}$$
$$v_t + (\vec{u}\cdot\nabla)v + fu - f_h w = 0 \tag{2.98}$$
$$w_t + (\vec{u}\cdot\nabla)w + f_h v - f_g u = -p_z + b \tag{2.99}$$
$$u_x + w_z = 0 \tag{2.100}$$
$$b_t + (\vec{u}\cdot\nabla)b + N^2 w = 0, \tag{2.101}$$

where u,v and w are the fluid velocity components in the x, y and z directions respectively, $b = -\rho g$ is the buoyancy, p is the departure of pressure from its hydrostatic value divided by a constant reference density ρ_0 and $N^2 = -\frac{g}{\rho_0}\frac{\mathrm{d}\bar{\rho}}{\mathrm{d}z}$ is assumed to be constant.

Two-dimensional incompressible flow assumption makes it possible to introduce a stream function Ψ such that $(u, w) = (\Psi_z, -\Psi_x)$. Applying this to equations (2.97) - (2.101) we find that

$$\Psi_{zt} + \Psi_z\Psi_{xz} - \Psi_x\Psi_{zz} - fv - f_g\Psi_x = -p_x \tag{2.102}$$
$$v_t + \Psi_z v_x - \Psi_x v_z + f\Psi_z + f_h\Psi_x = 0 \tag{2.103}$$
$$-\Psi_{xt} - \Psi_z\Psi_{xx} + \Psi_x\Psi_{xz} + f_h v - f_g\Psi_z = -p_z + b \tag{2.104}$$
$$b_t + b_x\Psi_z - b_z\Psi_z - N^2\Psi_x = 0. \tag{2.105}$$

To obtain a vorticity equation from equations (2.102) and (2.104) we substract $\partial_x \times$ (2.104) from $\partial_z \times$ (2.102) so that the governing equations (2.97) - (2.101) now become

$$\nabla^2\Psi_t + \mathbf{J}(\nabla^2\Psi, \Psi) - f_h v_x - f v_z + b_x = 0 \tag{2.106}$$
$$v_t + \mathbf{J}(v, \Psi) + f_h\Psi_x + f\Psi_z = 0 \tag{2.107}$$
$$b_t + \mathbf{J}(b, \Psi) - N^2\Psi_x = 0, \tag{2.108}$$

where the Jacobian is defined as $\mathbf{J}(A, B) = A_xB_z - A_zB_x$ and $\nabla^2 = \partial_x^2 + \partial_z^2$. In the course of reducing the model equations the terms involving f_g were eliminated from the equations of motion , also f_g can be removed by replacing p by $p - f_g\psi$ in equations (2.102) and (2.104). This means that while the linear dispersion relation, ψ and b are not affected by f_g the pressure is. Thus non-traditional effects are now present only via f_h. As in the linear case, section (2.3.6), for waves propagating in the east-west direction the non-traditional term does not modify the dispersion relation.

Introducing a Perturbation Expansion

To treat the reflection of weakly nonlinear waves that is monochromatic at lowest order and has frequency ω, we will express the fields in terms of an amplitude parameter $\epsilon \ll 1$ (representing the intensity of the wave) and expand Ψ, b and t as follows:

$$\Psi = \epsilon\{\Psi_1 \exp(-i\omega t) + \text{c.c.}\} + \epsilon^2\{\Psi_0 + [\Psi_2 \exp(-2i\omega t) + \text{c.c.}]\} + \cdots \tag{2.109}$$

$$v = \epsilon\{V_1 \exp(-i\omega t) + \text{c.c.}\} + \epsilon^2\{V_0 + [V_2 \exp(-2i\omega t) + \text{c.c.}]\} + \cdots \tag{2.110}$$

$$b = \epsilon\{\Gamma_1 \exp(-i\omega t) + \text{c.c.}\} + \epsilon^2\{\Gamma_0 + [\Gamma_2 \exp(-2i\omega t) + \text{c.c.}]\} + \cdots \tag{2.111}$$

where the mean fields (time independent) are associated with index 0, the primary waves (frequency ω) with index 1 and second harmonic (frequency 2ω) with index 2. The mean fields and second harmonic will be accounted for at order ϵ^2. Complex conjugates (c.c.) do not appear in the mean field. Similar expansion method was used in [11] and [36].

To obtain equations representing the primary waves, mean field and second harmonic we substitute equations (2.109) - (2.111) into equations (2.106) - (2.108) to obtain

$$\begin{aligned}&\epsilon\Big\{-i\omega\Psi_{1,xx}\exp(-i\omega t) + \text{c.c.} - i\omega\Psi_{1,zz}\exp(-i\omega t) + \text{c.c.} - f(V_{1,z}\exp(-i\omega t) + \text{c.c.})\\&- f_h(V_{1,x}\exp(-i\omega t) + \text{c.c.}) + (\Gamma_{1,x}\exp(-i\omega t) + \text{c.c.})\Big\} + \epsilon^2\Big\{(-2i\omega\Psi_{2,xx}\exp(-2i\omega t) + \text{c.c.})\\&+ (\mathbf{J}(\nabla^2\Psi_1, \Psi_1^*) + \mathbf{J}(\nabla^2\Psi_1^*, \Psi_1)) - f(V_{2,z}\exp(-2i\omega t) + \text{c.c.} + V_{0,z})\\&- f_h(V_{2,x}\exp(-2i\omega t) + \text{c.c.} + V_{0,x}) + (\Gamma_{2,x}\exp(-2i\omega t) + \text{c.c.} + \Gamma_{0,x})\Big\} + \cdots = 0\end{aligned} \tag{2.112}$$

$$\begin{aligned}&\epsilon\Big\{-i\omega V_1\exp(-i\omega t) + \text{c.c.} + f(\Psi_{1,z}\exp(-i\omega t) + \text{c.c.}) + f_h(\Psi_{1,x}\exp(-i\omega t) + \text{c.c.})\Big\}\\&+ \epsilon^2\Big\{-2i\omega V_2\exp(-2i\omega t) + \text{c.c.} + f(\Psi_{0,z} + \Psi_{2,z}\exp(-2i\omega t) + \text{c.c.})\\&+ f_h(\Psi_{0,x} + \Psi_{2,x}\exp(-2i\omega t) + \text{c.c.}) + (\mathbf{J}(V_1, \Psi_1^*) + \text{c.c.})\Big\} + \cdots = 0,\end{aligned} \tag{2.113}$$

and

$$\begin{aligned}&\epsilon\Big\{-i\omega\Gamma_1\exp(-i\omega t) + \text{c.c.} - N^2(\Psi_{1,x}\exp(-i\omega t) + \text{c.c.})\Big\} + \epsilon^2\Big\{(-2i\omega\Gamma_2\exp(-2i\omega t) + \text{c.c.})\\&+ (\mathbf{J}(\Gamma_1, \Psi_1^*) + \text{c.c.}) - N^2(\Psi_{0,x} + \Psi_{2,x}\exp(-2i\omega t) + \text{c.c.})\Big\} + \cdots = 0,\end{aligned} \tag{2.114}$$

Primary Wave - order ϵ

Collecting the terms of order ϵ, the equations representing the primary waves are given by [11]

$$-i\omega\nabla^2\Psi_1 - f_h V_{1,x} - fV_{1,z} + \Gamma_{1,x} = 0 \tag{2.115}$$

$$-i\omega V_1 + f_h\Psi_{1,x} + f\Psi_{1,z} = 0 \tag{2.116}$$

$$-i\omega\Gamma_1 - N^2\Psi_{1,x} = 0. \tag{2.117}$$

From equations (2.116) and (2.117) we obtain

$$\begin{cases} V_1 = \frac{1}{i\omega}(f_h\Psi_{1,x} + f\Psi_{1,z}) \\ \Gamma_1 = \frac{i}{\omega}N^2\Psi_{1,x}. \end{cases} \tag{2.118}$$

Taking the x-derivative of equation (2.118), substituting same in equation (2.115) and after doing some algebra we obtain

$$A\Psi_{1,xx} + 2B\Psi_{1,xz} + C\Psi_{1,zz} = 0 \tag{2.119}$$

where $A = N^2 - \omega^2 + f_h^2,\ B = ff_h,\ C = f^2 - \omega^2$ are all constant. Looking for solutions proportional to $\exp i(kx + mz)$ gives

$$-\frac{k}{m} = \frac{B \pm (B^2 - AC)^{\frac{1}{2}}}{A}, \tag{2.120}$$

where $-\frac{k}{m}$ is the slope of the beam.

Characteristic Coordinate

Our next goal is to transform equation (2.119) into characteristic coordinates. Consider the operator

$$\mathsf{L}[\Psi_1] := A\Psi_{1,xx} + 2B\Psi_{1,xz} + C\Psi_{1,zz} \tag{2.121}$$

whose discriminant is defined by

$$\Delta(\mathsf{L}) = \det\begin{bmatrix} B & A \\ C & B \end{bmatrix} = B^2 - AC. \tag{2.122}$$

Assuming that Ψ_1 is the solution of equation (2.119), we can define

$$W(\xi,\eta) = \Psi_1(x(\xi,\eta), z(\xi,\eta)), \tag{2.123}$$

where ξ and η are the characteristic coordinates. They represent curves along which

$$\frac{dz}{dx} = \frac{B \pm (B^2 - AC)^{\frac{1}{2}}}{A} \equiv \mu_\pm. \tag{2.124}$$

This is useful for determining qualitative behaviour of solutions. For $f_h = 0$, equation (2.124) reduces to

$$\frac{dz}{dx} = \pm\sqrt{\frac{\omega^2 - f^2}{N^2 - \omega^2}}. \tag{2.125}$$

We introduce the characteristic coordinates via,

$$\begin{cases} \xi = x - \int_{z_0}^{z} \frac{d\tilde{z}}{\mu_+} \\ \\ \eta = x - \int_{z_0}^{z} \frac{d\tilde{z}}{\mu_-} \end{cases} \tag{2.126}$$

where z_0 is an arbitrary constant (possibly zero). In [2] it was pointed out that the orientation of $\eta =$ const depends on the sign of C that is depending on whether or not the waves are super-inertial, inertial or sub-inertial. Thus there are three different cases to consider. In the case of super-inertial waves ($\omega > |f|$), the two characteristics $\xi =$ const and $\eta =$ const always have different orientation, this is the case for both the traditional and non-traditional approximation, although the steepness of the two characteristics differ in the non-traditional approximation. For inertial waves ($\omega = |f|$), $\eta =$ const has a horizontal orientation, the other characteristic $\xi =$const which does not exist for the traditional approximation maintains its orientation and its steepness depends on the buoyancy frequency N. Lastly, for the sub-inertial waves the two characteristics have the same orientation and their steepness tends to the same limit as $\omega \to \omega_{\min}$. See figure (2.7).

By the inverse function theorem we can re-write (2.123) to be in the form

$$\Psi_1(x, z) = W(\xi(x, z), \eta(x, z)). \tag{2.127}$$

Applying chain rule of differentiation gives,

$$\begin{cases} \Psi_{1,x} = W_\xi \xi_x + W_\eta \eta_x \\ \Psi_{1,z} = W_\xi \xi_z + W_\eta \eta_z \\ \Psi_{1,xx} = W_{\xi\xi}(\xi_x)^2 + 2W_{\xi\eta}\xi_x\eta_x + W_{\eta\eta}(\eta_x)^2 + W_\xi \xi_{xx} + W_\eta \eta_{xx} \\ \Psi_{1,zz} = W_{\xi\xi}(\xi_z)^2 + 2W_{\xi\eta}\xi_z\eta_z + W_{\eta\eta}(\eta_z)^2 + W_\xi \xi_{zz} + W_\eta \eta_{zz} \\ \Psi_{1,xz} = W_{\xi\xi}\xi_x\xi_z + W_{\xi\eta}(\xi_x\eta_z + \eta_x\xi_z) + W_{\eta\eta}\xi_x\eta_z + W_\xi \xi_{xz} + W_\eta \eta_{xz}. \end{cases} \tag{2.128}$$

Substituting equation (2.128) into equation (2.119) we obtain

$$\tilde{\mathsf{L}}[W] = \bar{A}W_{\xi\xi} + 2\bar{B}W_{\xi\eta} + \bar{C}W_{\eta\eta} = 0 \tag{2.129}$$

where

$$\begin{cases} \bar{A}(\xi,\eta) = A\xi_x^2 + 2B\xi_x\xi_z + C\xi_z^2 \\ \bar{B}(\xi,\eta) = A\xi_x\eta_x + B(\xi_x\eta_z + \xi_z\eta_x) + C\xi_z\eta_z \\ \bar{C}(\xi,\eta) = A\eta_x^2 + 2B\eta_x\eta_z + C\eta_z^2 \end{cases} \tag{2.130}$$

Suppose that equation (2.119) is hyperbolic so that wave propagation is possible then $B^2 - AC > 0$. For constant N the two characteristics ξ and η may be expressed as

$$\begin{cases} \xi = \left(\dfrac{B + (B^2 - AC)^{\frac{1}{2}}}{A}\right) x - z \\ \eta = \left(\dfrac{B - (B^2 - AC)^{\frac{1}{2}}}{A}\right) x - z \end{cases} \tag{2.131}$$

then $\bar{A} = \bar{C} = 0$. With the change of coordinates (2.131), dividing by $2\bar{B}$ the hyperbolic equation (2.119) takes the canonical form

$$\tilde{\mathsf{L}}[W] = W_{\xi\eta} = 0, \tag{2.132}$$

which we can writen as $(W_\xi)_\eta = 0$. Let

$$W_\xi = F'(\xi), \tag{2.133}$$

where $F(\xi)$ is the primitive of W_ξ this implies that

$$(W - F(\xi))_\xi = 0 \;\Rightarrow\; W - F(\xi) = G(\eta). \tag{2.134}$$

General solution to the primary wave equation is given by

$$\Psi_1(x,z) = W(\xi,\eta) = F(\xi) + G(\eta), \tag{2.135}$$

where G and F are arbitrary functions describing the propagation of wave-energy along one of the two characteristic coordinates [11]. Equations (2.118) and (2.135) represents a complete solution of the order-ϵ problem. For convenience let

$$\begin{cases} \mu_+ = \dfrac{B + (B^2 - AC)^{\frac{1}{2}}}{A}, \\ \mu_- = \dfrac{B - (B^2 - AC)^{\frac{1}{2}}}{A}, \end{cases} \tag{2.136}$$

and note that in the special case of a horizontal bottom and under the traditional approximation we have $\mu_+ = -\mu_-$ which implies that the characteristics (ξ, η) are equally steep which is not the case in the non-traditional approximation where $\mu_+ \neq -\mu_-$. A wave of frequency ω propagating along a particular characteristic say ξ creates at each point it passes reflected waves which will propagate along the other characteristic say η. The slopes of the characteristics is given by $-\frac{k}{m} = \mu_\pm$ where $\mu_\pm$ is defined in equation (2.136). Making the non-traditional approximation gives $\mu_+ \neq -\mu_-$ hence the incident and reflected beams are not equally steep. In the case of interaction of two beams, each of the two interacting beams represent one of two characteristics ξ or η. See figure (2.7) showing the orientations of the characteristics in terms of waves of super-inertial, inertial and sub-inertial frequencies.

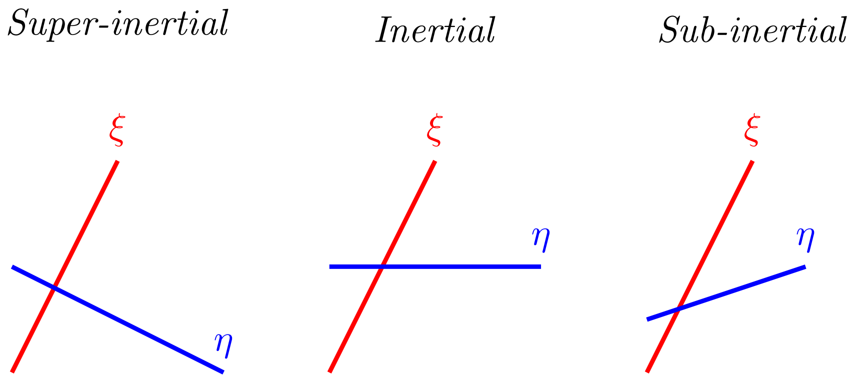

Figure 2.7: Schematic illustrating the different orientations of the characteristics $\xi = \text{const}$ and $\eta = \text{const}$.

Derivation of Maximum and Minimum frequency

In furtherance of reflection of internal waves from a uniform slope, let F and G represent the incident and reflected beams respectively. [36] and [11] derived coupling equations for the two wave beams. We assume a uniform slope $z = \beta x$ and require that $\Psi_1 = 0$ at the slope so that for all x

$$F([\mu_+ - \beta]x) + G([\mu_- - \beta]x) = 0. \tag{2.137}$$

Using equation (2.137) in (2.135) we obtain

$$G(\eta) = -F(\xi) = -F([\mu_+ - \beta]x). \tag{2.138}$$

Hence at the slope we get

$$\Psi_1 = F(\xi) - F\left(\frac{\mu_+ - \beta}{\mu_- - \beta}\eta\right) = 0. \tag{2.139}$$

Continuing the discussion on wave beams, we note that for energy to propagate in one direction we require a uni-directional beam which involves plane waves with wavenumbers of the same sign only [36]. Thus we will be concerned with plane waves having strictly positive or strictly negative wavenumbers. Consider a wave beam of frequency $\omega > 0$ and $(k, m) = \kappa(\sin\theta, \cos\theta)$ with $0 < \theta < \frac{\pi}{2}$, let $F(\xi)$ and $G(\eta)$ be superposition of plane waves with $k > 0$,

$$F(\xi) = \int_0^\infty A(k)\exp(ik\xi)\mathrm{d}k \qquad \text{and} \qquad G(\eta) = \int_0^\infty A(k)\exp(ik\lambda\eta)\mathrm{d}k, \tag{2.140}$$

where $A(k)$ is the Fourier transform of $\Psi(\xi, t = 0)$ or $\Psi(\eta, t = 0)$. Equation (2.140) gives wave beams for which energy travels along the positive ξ or η-direction. If however $k < 0$ then

$$F(\xi) = \int_{-\infty}^0 A(k)\exp(ik\xi)\mathrm{d}k \qquad \text{and} \qquad G(\eta) = \int_{-\infty}^0 A(k)\exp(ik\lambda\eta)\mathrm{d}k, \tag{2.141}$$

for this energy travels in the negative ξ or η-direction. Substituting equation (2.140) for Ψ_1 gives,

$$\Psi_1 = F(\xi) + G(\eta) = \int_0^\infty A(k)[\exp(ik\xi) - \exp(ik\lambda\eta)]\mathrm{d}k, \tag{2.142}$$

where $\lambda = \frac{\mu_+ - \beta}{\mu_- - \beta}$.

To derive expressions for the maximum and minimum possible internal wave frequencies for wave propagation, we recall equation (2.119) where for hyperbolicity it is required that

$$B^2 - AC > 0,$$

now,

$$B^2 - AC = f^2 f_h^2 - (N^2 - \omega^2 + f_h^2)(f^2 - \omega^2) > 0,$$

requires that

$$\omega^4 - \omega^2\lambda + N^2 f^2 < 0 \tag{2.143}$$

where $\lambda = N^2 + f^2 + f_h^2$. This is a quadratic equation for ω^2 and solving we get

$$\omega^2 = \frac{\lambda \pm \sqrt{\lambda^2 - 4N^2 f^2}}{2}, \tag{2.144}$$

hence we find that,

$$\begin{cases} \omega_{\text{min}} = \left(\dfrac{\lambda - \sqrt{\lambda^2 - 4N^2 f^2}}{2} \right)^{\frac{1}{2}} \\ \omega_{\text{max}} = \left(\dfrac{\lambda + \sqrt{\lambda^2 - 4N^2 f^2}}{2} \right)^{\frac{1}{2}} \end{cases} \tag{2.145}$$

thus verifying results earlier obtained by [13] for a bounded range of possible internal wave frequencies.

Under the traditional approximation ($f_h = 0$) (2.145) reduces to

$$\begin{cases} \omega_{\text{min}} = \left(\dfrac{(N^2 + f^2) - \sqrt{(N^2 + f^2)^2 - 4N^2 f^2}}{2} \right)^{\frac{1}{2}} \\ \omega_{\text{max}} = \left(\dfrac{(N^2 + f^2) + \sqrt{(N^2 + f^2)^2 - 4N^2 f^2}}{2} \right)^{\frac{1}{2}}, \end{cases} \tag{2.146}$$

which further simplifies to

$$\begin{cases} \omega_{\text{min}}^2 = f^2 \\ \omega_{\text{max}}^2 = N^2, \end{cases} \tag{2.147}$$

from equation (2.147) we recover the range $f^2 < \omega^2 < N^2$.

Mean Field - order ϵ^2

The time-independent terms in the expansion (2.112)-(2.114) are associated with the mean field, putting this terms together gives the system of equations

$$[\mathbf{J}(\nabla^2\Psi_1, \Psi_1^*) + \text{c.c.}] - f_h V_{0,x} - f V_{0,z} + \Gamma_{0,x} = 0 \tag{2.148}$$

$$[\mathbf{J}(V_1, \Psi_1^*) + \text{c.c.}] + f_h \Psi_{0,x} + f \Psi_{0,z} = 0 \tag{2.149}$$

$$[\mathbf{J}(\Gamma_1, \Psi_1^*) + \text{c.c.}] - N^2 \Psi_{0,x} = 0. \tag{2.150}$$

Using the identity $i\mathbf{J}(P_x, P^*) + \text{c.c.} = i\mathbf{J}(P, P^*)_x$ and $\Gamma_1 = \frac{i}{\omega} N^2 \Psi_{1,x}$ from equation (2.118) in equation (2.150) we get

$$\mathbf{J}\left(\frac{i}{\omega} N^2 \Psi_{1,x}, \Psi_1^*\right) + \mathbf{J}\left(\frac{i}{\omega} N^2 \Psi_{1,x}^*, \Psi_1\right) = N^2 \Psi_{0,x},$$

which implies that

$$\frac{i}{\omega}N^2\mathbf{J}(\Psi_1, \Psi_1^*)_x = N^2\Psi_{0,x},$$

upon integrating with respect to x we find that

$$\Psi_0 = \frac{i}{\omega}\mathbf{J}(\Psi_1, \Psi_1^*). \tag{2.151}$$

Using equations (2.135) and (2.151) we show that no nonlinear effects is produced from the interaction of one plane internal wave with itself. Consider the right side of (2.151),

$$\begin{aligned}
\mathbf{J}(\Psi_1, \Psi_1^*) &= \Psi_{1,x}\Psi_{1,z}^* - \Psi_{1,z}\Psi_{1,x}^* \\
&= \big[F_\xi\xi_x + G_\eta\eta_x\big]\big[F_\xi^*\xi_z + G_\eta^*\eta_z\big] - \big[F_\xi^*\xi_z + G_\eta^*\eta_z\big]\big[F_\xi^*\xi_x + G_\eta^*\eta_x\big] \\
&= \big[F_\xi G_\eta^*\xi_x\eta_z + G_\eta\eta_x F_\xi^*\xi_z\big] - \big[F_\xi G_\eta^*\xi_z\eta_x - G_\eta\eta_z F_\xi^*\xi_x\big] \\
&= F_\xi G_\eta^*\big[\xi_x\eta_z - \xi_z\eta_x\big] + F_\xi^* G_\eta\big[\xi_x\eta_x - \xi_x\eta_z\big] \\
&= F_\xi G_\eta^*\big[\mu_+(-1) - (-1)\mu_-\big] + F_\xi^* G_\eta\big[(-1)\mu_- - (-1)(\mu_+)\big] \\
&= (\mu_+ - \mu_-)\big[F_\xi^* G_\eta - F_\xi G_\eta^*\big] \\
&= 2(\mu_+ - \mu_-)F_\xi G_\eta^*.
\end{aligned}$$

Thus

$$\Psi_0 = \frac{i}{\omega}\mathbf{J}(\Psi_1, \Psi_1^*) = \frac{2}{\omega}(\mu_+ - \mu_-)\mathbf{Im}\underbrace{\big[F'(\xi)G'(\eta)^*\big]}_{}, \tag{2.152}$$

which is an indication that only intersections of plane waves with different directions provide nonlinear terms as indicated by the terms marked by underbraces.

As in [11], a solution of the mean field for reflection from a uniform slope is obtained from equation (2.152) and (2.140) and using the fact that $G(\eta) = -F(\lambda\eta)$ to obtain

$$\Psi_0 = -\frac{2\lambda}{\omega}(\mu_+ - \mu_-)\int\int[A(k)A(k')kk'\sin(k\xi - k'\lambda\eta)]\mathrm{d}k\mathrm{d}k'. \tag{2.153}$$

From (2.153) Ψ_0 is zero at the slope satisfied. This can be seen by expanding the sine function using the double angle formular and interchanging the roles of k and k' in the second term of the expansion.

Second Harmonic - order ϵ^2

Collecting terms involving second harmonics gives the system of equations

$$-2i\omega\nabla^2\Psi_2 + \mathbf{J}(\nabla^2\Psi_1, \Psi_1) - f_h V_{2,x} - fV_{2,z} + \Gamma_{2,x} = 0 \tag{2.154}$$

$$-2i\omega V_2 + \mathbf{J}(V_1, \Psi_1) + f_h\Psi_{2,x} + f\Psi_{2,z} = 0 \tag{2.155}$$

$$-2i\omega\Gamma_2 + \mathbf{J}(\Gamma_1, \Psi_1) - N^2\Psi_{2,x} = 0, \tag{2.156}$$

from equations (2.155) and (2.156) we get

$$\begin{cases} V_2 = \frac{1}{2i\omega}(\mathbf{J}(V_1, \Psi_1) + f_h\Psi_{2,x} + f\Psi_{2,z}) \\ \Gamma_{2,x} = \frac{1}{2i\omega}(\mathbf{J}(\Gamma_1\Psi_1)_x - N^2\Psi_{2,xx}). \end{cases} \tag{2.157}$$

Substituting equation (2.157) into equation (2.154), multiplying through by $2i\omega$ and simplifying gives

$$\begin{aligned}(N^2 + f_h^2 - 4\omega^2)\Psi_{2,xx} + 2ff_h\Psi_{2,xz} + (f^2 - 4\omega^2)\Psi_{2,zz} \\ = \mathbf{J}(\Gamma_1, \Psi_1)_x - (f_h\partial_x + f\partial_z)\mathbf{J}(V_1, \Psi_1) + 2i\omega\mathbf{J}(\nabla^2\Psi_1, \Psi_1).\end{aligned} \tag{2.158}$$

Further, simplifying the R.H.S of equation (2.158) by substituting the lowest order solutions we obtain

$$A_2\Psi_{2,xx} + 2B\Psi_{2,xz} + C_2\Psi_{2,zz} = 3i\omega\mathbf{J}(\nabla^2\Psi_1, \Psi_1), \tag{2.159}$$

which is a forced version of the equation for Ψ_1, where A_2 and C_2 are the same as the previous A and C but for frequency 2ω. For the second harmonics we have the following

$$\begin{cases} A_2 = N^2 + f_h^2 - (2\omega)^2 \\ B = ff_h \\ C_2 = f^2 - (2\omega)^2 \\ \xi_2 = \left(\dfrac{B + (B^2 - A_2C_2)^{\frac{1}{2}}}{A_2}\right) x - z \\ \eta_2 = \left(\dfrac{B - (B^2 - A_2C_2)^{\frac{1}{2}}}{A_2}\right) x - z. \end{cases} \tag{2.160}$$

where ξ_2 and η_2 are characteristics representing beams formed by the nonlinear interaction between the beams of ξ_1 and η_1 characteristics.

The general solution to the second harmonic equation (2.159) is

$$\Psi_2 = F_2(\xi_2) + G_2(\eta_2) + \Psi_{2,p}, \tag{2.161}$$

where F_2 and G_2 are arbitary functions in the absence of forcing and $\Psi_{2,p}$ represents a particular solution to the non-homogeneous equation (2.159) which takes care of the forcing term $3i\omega\mathbf{J}(\nabla^2\Psi_1, \Psi_1)$. The particular solution can be expressed in terms of the general solution (2.135) using

$$\mathbf{J}(\nabla^2\Psi_1, \Psi_1) = -(\mu_+ - \mu_-)[(1+\mu_+^2)F'''(\xi)G'(\eta) - (1+\mu_-^2)G'''(\eta)F'(\xi)], \tag{2.162}$$

this is again an afirmation that nonlinear interactions occur in regions where internal waves propagating in different directions overlap.

Using (2.140), equation (2.162) may be expressed as

$$\mathbf{J}(\nabla^2\Psi_1, \Psi_1) = \lambda(\mu_+ - \mu_-)\int\int \mathrm{d}k\mathrm{d}k' A(k)A(k')kk'[(1+\mu_+^2)k^2 - (1+\mu_-^2)k'^2\lambda^2]\exp(i(k\xi + k'\lambda\eta)). \tag{2.163}$$

A complete solution to (2.159) (as stated in [11]) is given by

$$\Psi_2 = 3i\omega\lambda(\mu_+ - \mu_-)\int\int \mathrm{d}k\mathrm{d}k' S(k,k')[\exp(i(k\xi + k'\lambda\eta)) - \exp(i(R(k,k')\eta_2))], \tag{2.164}$$

where η_2 is found from (2.160) and

$$\begin{cases} S(k,k') = \dfrac{A(k)A(k')kk'[(1+\mu_+^2)k^2 - (1+\mu_-^2)k'^2\lambda^2]}{A_2(k\mu_+ + k'\lambda\mu_-)^2 - 2B(k\mu_+ + k'\lambda\mu_-)(k+k'\lambda) + C_2(k+k'\lambda)^2} \\ \\ R(k,k') = \dfrac{\mu_+ - \gamma}{\mu_{2,-} - \gamma}(k+k'). \end{cases} \tag{2.165}$$

The terms involving $R(k,k')$ represent solution to the homogeneous part of (2.159) and incoporated in such a fashion that enables the boundary condition of zero normal velocity at the slope to be satisfied, Gerkema [14].

2.4 Near Inertial Behaviour of the Primary Wave

We continue the treatment of the primary wave equation (2.119) derived in section (2.3.7) by describing its behaviour near the inertial frequency via the disperson relation in a vertically bounded and horizontally uniform domain. It is important to note that the primary wave equation cannot be solved by the separable method except in the traditional approximation where $f_h = 0$. A way to get around this is to try to reduce the equation to a boundary value problem using the ansatz

$$\Psi_1 = \psi(z) \exp i(kx + \delta z), \tag{2.166}$$

to equation (2.119), where $\delta = -\frac{kB}{C}$, with rigid lid approximation ($\Psi_1(0) = 0$) at the surface and varnishing normal velocity at the bottom ($\Psi_1(-H) = 0$). This ansatz was first introduced by [34] where it was used to treat the influence of uniform currents on a fluid layer bounded by two rigid surfaces. It was later on adopted by [13] to show that sub-inertial waves become infinitely short as the wave frequency ω tends to the minimum frequency ω_{min} for any model of stratification.

The aim of this section which was adapted from [13] is to show the existence of super-inertial and sub-inertial waves in the non-traditional approximation using a near inertial wave arguement. We proceed by substituting (2.166) into (2.119), taking real part and applying the boundary conditions to get

$$\psi''(z) + k^2 \left[\frac{N^2 - \omega^2}{\omega^2 - f^2} + \left(\frac{\omega f_h}{\omega^2 - f^2} \right)^2 \right] \psi = 0; \qquad \psi(0) = \psi(-H) = 0. \tag{2.167}$$

As was noted in [13], the behaviour of the singularity when $\omega = |f|$ is modified by the presence of the additional constant due to the non-traditional f_h term. Let k^2 be the eigenvalue of the Sturm-Liouville problem to be determined and assuming constant bouyancy frequency N_c

$$\varrho^2 = k^2 \left[\frac{N_c^2 - \omega^2}{\omega^2 - f^2} + \left(\frac{\omega f_h}{\omega^2 - f^2} \right)^2 \right]. \tag{2.168}$$

Solving the second-order ODE and using the boundary conditions specified in equation (2.167) the eigenfunction is found to be

$$\psi_n = \sin \varrho_n z, \tag{2.169}$$

where $\varrho_n = \frac{n\pi}{H} (n \in \mathbb{Z})$.

From equation (2.168) the dispersion relation gives

$$k_n = \pm \frac{\varrho_n}{\left[\frac{N_c^2 - \omega^2}{\omega^2 - f^2} + \left(\frac{\omega f_h}{\omega^2 - f^2} \right)^2 \right]^{\frac{1}{2}}}. \tag{2.170}$$

Consider the special case where the wave frequency is very close to the inertial frequency then the second (quadratic) term in square bracket in equation (2.167) is the dominant term, hence the first approximation of the dispersion relation (2.170) reads

$$k_n = \pm \frac{\varrho_n}{\left(\dfrac{\omega f_h}{\omega^2 - f^2}\right)}. \tag{2.171}$$

We can exploit the limit as $\omega \to f$ even further, notice that

$$\pm\, k_n \frac{\omega f_h}{\omega^2 - f^2} = \varrho_n \tag{2.172}$$

expanding the denominator on the LHS with respect to ω we find that

$$\pm\, k_n \frac{f_h}{\left[\omega\left(1 - \frac{f}{\omega}\right)\left(1 + \frac{f}{\omega}\right)\right]} = \varrho_n. \tag{2.173}$$

Taking the limit as $\omega \to f$ equation (2.173) becomes

$$\pm\, k_n \frac{f_h}{2(\omega - f)} = \varrho_n. \tag{2.174}$$

The second approximation to the dispersion relation becomes

$$\omega = |f| \pm k_n \frac{f_h H}{2n\pi}, \tag{2.175}$$

where $\varrho_n = \dfrac{n\pi}{H}$. Equation (2.175) indicates the existence of super-inertial and sub-inertial wave modes. These two families tend to the inertial frequency in the long wave limit [13].

2.5 Reflection from a Uniform Slope

Gerkema and Shrira [14] treated reflection of internal waves from a uniform slope $z = \alpha x + \beta y$ in 3-D. They obtained an expression for the amplitude of the reflected beam in terms of the incident beam and derived condition for critical reflection. Because the IGW model is a 2-D model we will duplicate the work done in [14] by deriving a 2-D analogue of the critical reflection criterion. The section begins with a general view of wave reflection. Using a two-dimensional uniform slope defined by $z = \beta x$ we establish a relationship between the wave numbers of the incident and reflected beams.

Consider wave propagation in the x-z plane. Using the continuity equation $u_x + w_z = 0$ we introduce a stream function Ψ such that

$$u = \Psi_z \qquad \text{and} \qquad w = -\Psi_x.$$

The total wave field comprising the incident and reflected waves is given by

$$\Psi = \Psi_I + \Psi_R = a_I \exp i(k_I x + m_I z - \omega_I t) + a_R \exp i(k_R x + m_R z - \omega_R t), \tag{2.176}$$

where I and R subscripts represents incident and reflected, a_I and a_R are the wave amplitudes which are in general complex numbers but we will restrict our study to the domain of real numbers.

For the boundary condition (zero normal velocity at the slope) to be satisfied we must have $\Psi = 0$ for x and t at the slope. This requires that

$$k_I x + \beta m_I x - \omega_I t = k_R x + \beta m_R x - \omega_R t, \tag{2.177}$$

which requires that

$$\omega_I = \omega_R \qquad \text{and} \qquad k_I + \beta m_I = k_R + \beta m_R. \tag{2.178}$$

$\Psi = 0$ on $z = \beta x$ also means that $\Psi_R = -\Psi_I$.

The properties of internal waves that are relevant for the present analysis are as follows [?]: the frequency of the first harmonic reflected wave is equal to that of the incident wave. Secondly, the frequency is given by $\omega^2 = N^2 \sin^2 \nu + (f_h \sin \nu + f \cos \nu)^2$ where ν is the angle the wave number vector makes with the vertical, see figure (2.3), thus because of the $f_h \cos \theta$ term the angle of the reflected wave with respect to the horizontal is not in general equal to that of the incident wave. Thirdly, the component of the wave vector along the slope of the reflected wave and incident wave are equal.

We need to find a way to represent the reflected wave in terms of the incident wave. Let

$$m_R = \wp m_I \tag{2.179}$$

where $\wp$ is an unknown variable to be determined, then from equation (2.178)

$$k_R = k_I + \beta(1 - \wp)m_I. \tag{2.180}$$

The requirement that the incident wave with wave vector (k_I, m_I) satisfy the dispersion relation (2.93) means that,

$$Ak_I^2 + 2Bk_I m_I + Cm^2 = 0. \tag{2.181}$$

Equation (2.181) was obtained from (2.119) by substituting the plane wave equation representing the incident wave beam. A, B and C retain their usual meaning. The wave vectors of the reflected wave has to satisfy the dispersion relation also, hence we substitute the incident equivalent of (k_R, m_R) into equation (2.181)

$$A(k_I + \beta(1 - \wp)m_I)^2 + 2B(k_I + \beta(1 - \wp)m_I)(\wp m_I) + C(\wp^2 m_I^2) = 0, \tag{2.182}$$

resulting in a quadratic equation for $\wp$,

$$\begin{aligned}(A\beta^2 m_I^2 - 2B\beta m_I^2 + Cm_I^2)\wp^2 - (2Ak_I\beta m_I + 2A\beta^2 m_I^2 - 2Bk_I m_I - 2B\beta^2 m_I)\wp \\ + (Ak^2 + 2Ak_I\beta m_I + A\beta^2 m_I^2) = 0.\end{aligned} \tag{2.183}$$

Solving and simplifying the algebra gives,

$$\wp^{\pm} = \frac{(\beta^2 m_I + \beta k_I)A - (\beta^2 + k_I)B \pm \sqrt{\nabla^D}}{m_I(A\beta^2 - 2\,B\beta + C)}, \tag{2.184}$$

where

$$\begin{aligned}\nabla^D =& 2\,\left(\beta^3 m_I^2 - \beta^3 k_I - \left(\beta^4 - \beta^2 k_I\right)m_I\right)AB + \left(\beta^4 + 2\,\beta^2 k_I + k_I^2\right)B^2 \\ &- \left(\beta^2 m_I^2 + 2\,\beta k_I m_I + k_I^2\right)AC.\end{aligned}$$

Along the ξ characteristic coordinate $\wp^+$ gives the reflected beam while $\wp^-$ represents beams going through the η characteristic coordinate.

The criterion for critical reflection is that the denominator of (2.184) varnishes. That is,

$$A\beta^2 - 2\,B\beta + C = 0. \tag{2.185}$$

This is the condition required for $|\wp|$ to become infinite, as $\wp \to \infty$ so does m_R and k_R and hence the wavelength goes to zero. The condition for critical reflection can also be interpreted as the condition in which the slope is parallel to one of the characteristics for waves of frequency ω. Solving this quadratic equation for β we obtain an expression for the critical slope,

$$\beta = \frac{B \pm [B^2 - AC]^{\frac{1}{2}}}{A}. \tag{2.186}$$

Under the traditional approximation ($f_h = 0$) we would have $B = 0$ and equation (2.186) becomes

$$\beta = \left(\frac{\omega^2 - f^2}{N^2 - \omega^2}\right)^{\frac{1}{2}} \tag{2.187}$$

which is a well known traditional criterion. Thus we see that for critical reflection to occur the slope of the topography β must equal that of the beam α. Equations (2.179) and (2.180) were used in plotting the group velocities of incident and reflected beams (figures (4.2a)–(4.2b)) in Chapter (4).

2.6 Energy Equation

In this section we derive equations governing the mechanical energy associated with the propagation of internal waves. To achieve this we make reference to the momentum equations in section (2.3.7). Multiplying equations (2.97), (2.98) and (2.99) by u, v and w respectively we find that

$$\frac{D}{Dt}\left(\frac{1}{2}u^2\right) - fvu + f_g wu = -up_x \tag{2.188}$$

$$\frac{D}{Dt}\left(\frac{1}{2}v^2\right) + fvu - f_h vw = -vp_y \tag{2.189}$$

$$\frac{D}{Dt}\left(\frac{1}{2}w^2\right) + f_h vw - f_g u = -wp_z + bw, \tag{2.190}$$

$$\tag{2.191}$$

where the pressure has been divided by a constant reference density ρ_0 and $b = -g\frac{\rho}{\rho_0}$. Summing the resulting equations we obtain

$$\frac{D}{Dt}\left(\frac{1}{2}\vec{u}\cdot\vec{u}\right) = up_x + vp_y + wp_z + bw. \tag{2.192}$$

Notice that the Coriolis terms are eliminated from the equations due to the fact that $\vec{u}\cdot(\vec{\Omega}\times\vec{u}) = 0$. Since the flow is incompressible we get

$$\frac{D}{Dt}\left(\frac{1}{2}\vec{u}\cdot\vec{u}\right) = \vec{\nabla}\cdot(\vec{u}p) + bw. \tag{2.193}$$

Multiplying the density equation (2.101) by $\frac{b}{N^2}$ gives

$$\frac{1}{N^2}\frac{D}{Dt}\left(\frac{1}{2}b^2\right) + bw = 0. \tag{2.194}$$

Combining equations (2.193) and (2.194) and assuming that N is constant we find that

$$\frac{D}{Dt}\left[\frac{1}{2}(u^2+v^2+w^2) + \frac{1}{2}\frac{b^2}{N^2}\right] + \partial_x(pu) + \partial_y(pv) + \partial_z(pw) = 0. \tag{2.195}$$

Expressing this in terms of kinetic and potential energy gives,

$$\partial_t(KE + PE) + \nabla\cdot(\vec{u}(KE + PE + p)) = 0. \tag{2.196}$$

The kinetic energy per unit mass is given by $\frac{1}{2}(u^2+v^2+w^2)$ and the available potential energy is given by $\frac{1}{2}\frac{b^2}{N^2}$. The total mechanical energy is the sum of the potential and kinetic energy.

2.7 Fourier Based Time Series Analysis

Time series analysis is a technique used in obtaining meaningful information from a trend or time series. They may be grouped into frequency domain and time domain methods. Our focus however is on the frequency domain Fourier time series analysis which involves spectral analysis. Spectral methods are an important computational tool used in research to gain information about a physical or natural occurrence involving data manipulations, they are most successful in problems with periodic geometries. In Chapter (4) we considered a particular case of wave beam reflection from a flat bottom and some cases of colliding beams where moorings were used to obtain data in a series of particular time intervals and at marked locations. The aim was to obtain information about dominant frequencies in the time series using the fast Fourier transform. Physical processes can be described in the time domain by a function $h(t)$ or in the frequency domain by specifying its amplitude H as a function of frequency ω. In general H is a complex number which provides information about the phase of the signal being studied. Here we will introduce the basic ingredients of Fourier time series analysis.

The Fourier transform of a function $h(t)$, $t \in \mathbb{R}$ is the function $H(\omega)$ defined by

$$H(\omega) = \int_{-\infty}^{\infty} h(t)\exp(-i\omega t)\ \mathrm{d}t, \tag{2.197}$$

$h(t)$ can be obtained from $H(\omega)$ by taking the inverse Fourier transform

$$h(t) = \frac{1}{2\pi}\int_{-\infty}^{\infty} H(\omega)\exp(i\omega t)\ \mathrm{d}\omega. \tag{2.198}$$

2.7.1 Power Spectral Density

The Power spectral density (PSD) of a signal $h(t)$ describes the power present in the signal as a function of frequency. In theory this may be found from the Fourier transform in frequency space by taking the square of the magnitude of the Fourier transform. There are several methods to compute PSD of a signal and they are generally classified as parametric and non-parametric methods. We adopt the periodogram based approach which is an example of non-parametric method and is computationally less complex when compared with the parametric methods due to the availability of efficient algorithms. Another advantage of the non-parametic methods is that no prior knowledge of the parameters of the time series is needed to use this method, also non-parametric methods are efficient and reliable as the estimated PSDs do not contain invalid frequency peaks as is the case in the parametric methods when a wrong model is used. In this thesis we adopt the Welch PSD which is a well known non-parametric method which relies on averaging periodograms to reduce the variance of the power spectrum estimate. It was developed by Peter D. Welch and published in 1967, the methodology involves segmenting the data sets into smaller pieces and finding the spectrum for each piece (taking modified periodograms of each section) and averaging these modified periodograms [37].

2.8 Resonant Triads

In internal wave theory three waves form what is known as resonant triads if the sum of the frequencies and wave numbers of two of the waves equals those of the third, each of the three waves satisfy the dispersion relation. Thus they can be described as sets of three waves for which nonlinear interactions of any two resonantly forces the third. Consider a small amplitude wave of the form

$$a_j \exp\{-i(\vec{\kappa} \cdot \vec{x} - \omega_j t)\}, \qquad j = 1, 2, 3 \tag{2.199}$$

where a_j is the constant wave amplitude. Nonlinear interactions of any of the two waves above, for example nonlinear interactions of the $j = 1$ and $j = 2$ waves gives rise to

$$a_1 a_2 \exp\{-i(\vec{\kappa}_1 + \vec{\kappa}_2) \cdot \vec{x} + (\omega_1 + \omega_2)t\}. \tag{2.200}$$

When equation (2.200) acts as the forcing term, then resonance will occur if the following triad relationships are satisfied,

$$\vec{\kappa}_1 \pm \vec{\kappa}_2 \pm \vec{\kappa}_3 = 0 \tag{2.201}$$

$$\omega_1(\vec{\kappa}_1) \pm \omega_2(\vec{\kappa}_2) \pm \omega_3(\vec{\kappa}_3) = 0, \tag{2.202}$$

where $(k_j,\ j = 1, 2, 3)$ and $(\omega_j,\ j = 1, 2, 3)$ are the wave number and frequency of the resonant triads satisfying the dispersion relation of the system.

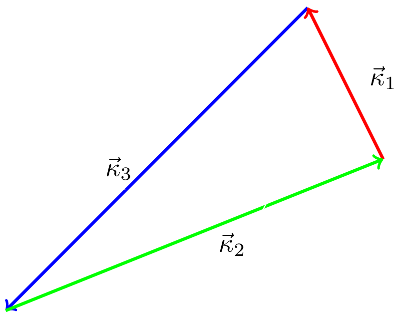

Figure 2.8: Schematic showing a resonant triad of interacting plane waves. In order for two waves to force a third resonantly, the frequencies and wave numbers of two of the waves must equal the third.

Chapter 3

Numerical Model and Computational Methods

This thesis uses a numerical model called the Internal Gravity Wave (IGW) Model to investigate the reflection of internal wave beams from a uniform slope and the collision of internal wave beams and consequent generation of higher harmonics. The model was introduced by Lamb in 1994, [22] and [23]. This chapter describes the model, grid, time stepping strategy and generation of internal wave beam.

3.1 IGW - Internal Gravity Wave Model

The Internal Gravity Wave Model is a 2-D, nonlinear, non-hydrostatic, incompressible, Boussinesq, sigma-coordinate model for simulating stratified flow phenomena. It solves the full nonlinear Navier-Stokes equations for flows with finite amplitude density variation. The numerical method adopted in IGW is based on the second-order projection methods developed by Bell, Colella and Glaz (1989), [3] and Bell and Marcus (1992), [4].

To demonstrate that the model is set up correctly, we ensured that the slope of the beams generated agrees with theoretical predictions and earlier work done in the field.

The IGW model solves the model equations

$$\vec{U}_t + \vec{U} \cdot \vec{\nabla}\vec{U} + 2\vec{\Omega} \times \vec{U} = -\vec{\nabla}p - \rho g\hat{k} \tag{3.1}$$

$$v_t + (\vec{U} \cdot \nabla)v + fu - f_h w = 0 \tag{3.2}$$

$$\vec{\nabla} \cdot \vec{U} = 0 \tag{3.3}$$

$$\frac{D\rho}{Dt} = 0 \tag{3.4}$$

where $\vec{U} = (u, w), 2\vec{\Omega} = 2\Omega(\cos\theta\sin\phi, \cos\theta\cos\phi, \sin\theta)$ and the equations are assumed to be independent of y. The variables in equations (3.1) - (3.4) retain their usual meaning. These equations are solved by specifying initial values for the velocity, density and pressure gradients and imposing the rigid lid approximation on the water surface.

In the IGW model the pressure can be eliminated from equations of motion by applying the Helmholtz decomposition which states that a vector field $\vec{V}$ can be uniquely decomposed into the sum of a divergence-free component $\vec{V}^D$ and the multiple of a strictly positive scalar function $a(x, z)$ and a gradient,

$$\vec{V} = \vec{V}^D + a\vec{\nabla}\phi, \tag{3.5}$$

where $a(x, z)$ is a known given function. Then a projection operator P that maps the vector $\vec{V}$ onto its divergence free part is defined by,

$$P(\vec{V}) = \vec{V}^D, \tag{3.6}$$

where P depends on both the function a and the boundary conditions. Note that when the Boussinesq approximation is made $a = 1$ otherwise $a = \frac{1}{\rho}$

3.2 Grid and Transformed Equations

IGW model uses terrain-following coordinates (σ-coordinates) with a computational grid comprising of I cells in the horizontal and J cells in the vertical. The grid is divided into an inner or central domain and an outer domain. The length of the inner domain is specified by the parameter L. The parameters I_l and I_r determine how many grid points will be used for the left and right side of the central domain respectively. We can compute the grid size of the central domain from the total horizontal and vertical grid points. The horizontal grid spacing of the central domain is approximately uniform and is given by

$$dx_{\text{central}} \approx \frac{L}{(I - I_l - I_r)}, \tag{3.7}$$

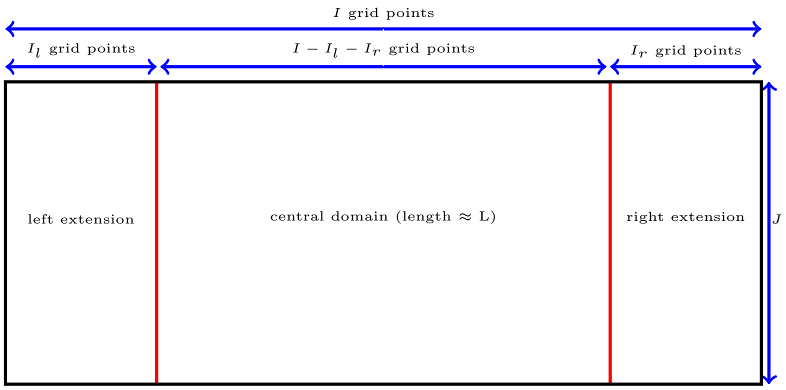

Figure 3.1: Schematic showing the partitioning of the computational grid. The central domain has length L. Horizontal grid spacing is given by $dx \approx \frac{L}{I-I_l-I_r}$, stretching the grid means that dx increases as we move away from the central domain

which allows equally spaced increments in the x-direction. There are three more parameters of interest in the Grid configuration they are: **grpar1**-which specifies the stretching factor of the grid to give the size of the grid in the outer domain as a multiple of the grid size in the central domain, **grpar2**-indicates the starting point of the stretching in terms of grid points away from the central domain, **grpar3**-represents the number of grid points over which to stretch the grid from the central domain grid size to the outer domain grid size. With these parameters the grid stretching in IGW is modelled using the sum of two hyperbolic tanh functions, the horizontal grid spacing along the x-axis is computed via

$$\begin{aligned} dx(i) = dx_{\text{central}} &* (1 + 0.5 * (\mathbf{grpar1} - 1) \\ &* (1 - \tanh((i - (I_l - \mathbf{grpar2}))/\mathbf{grpar3}) \\ &+ 1 + \tanh((i - (I - I_r + \mathbf{grpar2}))/\mathbf{grpar3}))). \end{aligned}$$

Figure (3.1) shows the partitioning of the computational grid. The choice of parameters is dependent on the choice of appropriate inner grid size, outer grid size, central domain size and outer domain size. To construct the grid the physical domain with coordinates (x, z) is mapped to the computational domain with coordinates (ξ, ζ) using the transformation

$$(\xi, \zeta) = (\xi(x, z), \zeta(x, z)). \tag{3.8}$$

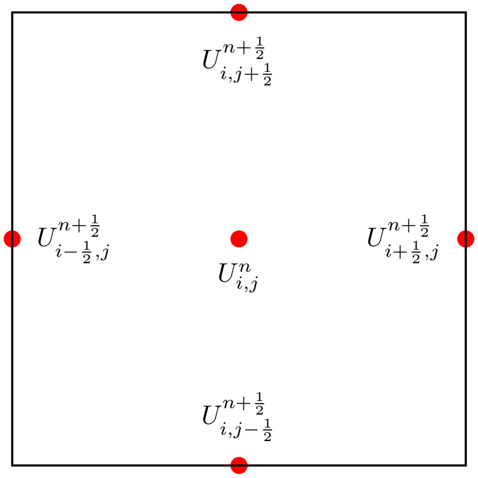

Figure 3.2: A grid cell. All the grid cells in the model set-up are unit squares.

3.3 Temporal Discretization

In this section we describe the time stepping strategy for the projection method used in IGW. For simplicity we will work in the physical space and assume a flat bottom domain. Applying the projection method requires that the momentum equation (3.1) be reorganised to give

$$\vec{U}_t + \vec{\nabla} p = -\vec{U} \cdot \vec{\nabla} \vec{U} - 2\vec{\Omega} \times \vec{U} - \rho g \hat{k}. \tag{3.9}$$

Now assuming temporal smoothness and divergence free nature of $\vec{U}_t$, applying the projection $\mathbb{P}$ to equation (3.9) gives

$$\vec{U}_t = P(\vec{V}), \tag{3.10}$$

where

$$\vec{V} = -\vec{U} \cdot \vec{\nabla} \vec{U} - 2\vec{\Omega} \times \vec{U} - \rho g \hat{k}. \tag{3.11}$$

Notice that the pressure have been removed from the equations. The projection method is only applicable if appropriate boundary conditions are specified and the fluid is incompressible. The projection operator $\mathbb{P}$ is independent of time, without the Boussinesq approximation we would have $\vec{U}_t + \frac{1}{\rho}\nabla p = \vec{V}$ and because the density ρ is a function of time t the projection operator which now depends on ρ, will also be a function of time.

To discuss how the projection method is applied to the equations of motion, we reintroduce the equations of motion in component form

$$u_t + (\vec{u} \cdot \nabla)u - fv + f_g w = -p_x \tag{3.12}$$
$$v_t + (\vec{u} \cdot \nabla)v + fu - f_h w = 0 \tag{3.13}$$
$$w_t + (\vec{u} \cdot \nabla)w + f_h v - f_g u = -p_z + b \tag{3.14}$$
$$u_x + w_z = 0 \tag{3.15}$$
$$\rho_t + (\vec{u} \cdot \nabla)\rho = 0, \tag{3.16}$$

where all variables retain their usual meaning. The values of u and w at the cell edges at time $n + \frac{1}{2}$ are obtained via extrapolation from the values of u and w at the cell centre at time $n + \frac{1}{2}$ respectively. u and w are then updated via the projection. Equations (3.12) and (3.14) may be written as

$$(u_t, w_t) + \nabla p = V^{n+\frac{1}{2}}, \tag{3.17}$$

where $V^{n+\frac{1}{2}}$ is given by equation (3.11) at time $n + \frac{1}{2}$. Applying the projection gives

$$(u_t, w_t) = P\left(V^{n+\frac{1}{2}}\right), \tag{3.18}$$

this gives the values of u_t and w_t at time $n + \frac{1}{2}$ that is $u_t^{n+\frac{1}{2}}$ and $w_t^{n+\frac{1}{2}}$, u and w are then updated via

$$u^{n+1} = u^n + \Delta t\left(u_t^{n+\frac{1}{2}}\right), \tag{3.19}$$

and

$$w^{n+1} = w^n + \Delta t\left(w_t^{n+\frac{1}{2}}\right), \tag{3.20}$$

We now turn to the equations for v and ρ given by (3.13) and (3.16). Firstly, v and ρ are updated using the extrapolated values, these updated values are then used in the equations for u and w. To update v IGW uses $\vec{u} \cdot \nabla v$, fu and $f_h w$ at time $n + \frac{1}{2}$. The estimates of u and w at the cell centre at time $n + \frac{1}{2}$ are also used in the v equation (3.13) to obtain v at time $n + 1$,

$$v^{n+1} = v^n - \Delta t\Big((\vec{U} \cdot \vec{\nabla} v)^{n+\frac{1}{2}} - fu^{n+\frac{1}{2}} + f_h w^{n+\frac{1}{2}}\Big). \tag{3.21}$$

The ρ equation is solved to get ρ at $n + 1$,

$$\rho^{n+1} = \rho^n - \Delta t(\vec{U} \cdot \vec{\nabla}\rho)^{n+\frac{1}{2}}. \tag{3.22}$$

The values of v and ρ at time n and $n+1$ are averaged to estimate v and ρ at time $n+\frac{1}{2}$.

$$v^{n+\frac{1}{2}} = \frac{v^n + v^{n+1}}{2}. \tag{3.23}$$

$$\rho^{n+\frac{1}{2}} = \frac{\rho^n + \rho^{n+1}}{2}, \tag{3.24}$$

These values from (3.23) and (3.24) are applied to equations (3.12) and (3.14).

In the time stepping scheme, a maximum time step is set and a CFL condition is imposed such that a fluid particle does not travel more than $\frac{1}{2}$ a grid cell in one time step.

3.4 Approximation of Nonlinear Advection Terms

We continue our discussion of discretization by describing the methods for approximating the nonlinear advection terms at time $n+\frac{1}{2}$. Description of how terms like fu and $g\rho$ at $n+\frac{1}{2}$ are estimated is also presented here. In the IGW model, the advective terms are approximated at time $t^{n+\frac{1}{2}}$ up to second-order in space and time using an explicit predictor-corrector scheme. This computation process is based on a second-order upwind

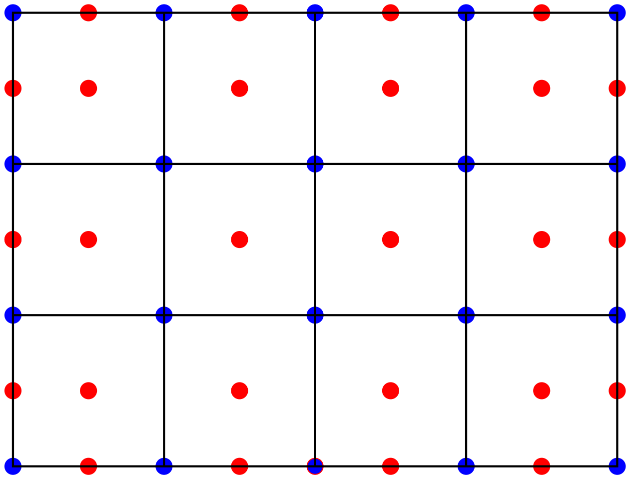

Figure 3.3: Schematic showing collection of cells comprising the scalar grid points (blue circles) located at the cell corners and vector grid points (red circles).

method first introduced by Bell and Collela, [3], [4] which requires the use of a 2nd-order Taylor series expansion. Quantities $\vec{U}$, ρ, and ∇p are given at the vector grid points, while the others such as $\nabla \cdot \vec{U}$, p, and a stream function, Ψ are defined on the scalar grid points. Using the 2nd-order centered difference scheme we approximate $[\vec{U} \cdot \vec{\nabla} U]^{n+\frac{1}{2}}$ as follows

$$\begin{aligned}
[\vec{U} \cdot \vec{\nabla} U]^{n+\frac{1}{2}} &= (uU_x + wU_z)^{n+\frac{1}{2}} \\
&\text{we suppress } n+\frac{1}{2} \text{ superscripts to obtain} \\
&= \frac{u_{i+\frac{1}{2},j} + u_{i-\frac{1}{2},j}}{2} \cdot \frac{U_{i+\frac{1}{2},j} - U_{i-\frac{1}{2},j}}{\Delta x} \\
&+ \frac{w_{i,j+\frac{1}{2}} + w_{i,j-\frac{1}{2}}}{2} \cdot \frac{U_{i,j+\frac{1}{2}} - U_{i,j-\frac{1}{2}}}{\Delta z}.
\end{aligned} \tag{3.25}$$

The values of U on the cell edges at time $t^{n+\frac{1}{2}}$ are determined via extrapolation of U^n. Consider the edge $i+\frac{1}{2}, j$, extrapolating from the left and right of the edge i.e, extrapolating values from (i, j) and $(i+1, j)$ yields two values for $U^{n+\frac{1}{2}}$. Extrapolating from the left and using equation (3.9) gives

$$\begin{aligned}
U^{n+\frac{1}{2},L}_{i+\frac{1}{2},j} &= U_{i,j}(x_i + \frac{\Delta x}{2}, z_j, t^n + \frac{\Delta t}{2}) \\
&= U^n_{ij} + \frac{\Delta x}{2} U^n_{x,ij} + \frac{\Delta t}{2} U^n_{t,ij} \\
&= U^n_{ij} + \frac{\Delta x}{2} U^n_{x,ij} + \frac{\Delta t}{2} (-[\vec{U} \cdot \vec{\nabla} U]^n - \nabla p^n) \\
&= \left[U^n + \left(\frac{\Delta x}{2} - \frac{\Delta t}{2} u^n \right) U^n_x - \frac{\Delta t}{2} (wU_z)^n - \frac{\Delta t}{2} \nabla p^n \right]_{ij}
\end{aligned} \tag{3.26}$$

Extrapolating from the right, that is from $i+1, j$ gives

$$U^{n+\frac{1}{2},R}_{i+\frac{1}{2},j} = \left[U^n - \left(\frac{\Delta x}{2} + \frac{\Delta t}{2} u^n \right) U^n_x - \frac{\Delta t}{2} (wU_z)^n - \frac{\Delta t}{2} \nabla p^n \right]_{i+1,j}. \tag{3.27}$$

This procedure is similar for other edges. Details of how to determine $U^{n+\frac{1}{2}}_{i+\frac{1}{2},j}$ from $U^{n+\frac{1}{2},L}_{i+\frac{1}{2},j}$ and $U^{n+\frac{1}{2},R}_{i+\frac{1}{2},j}$ using the upwinding scheme can be found in an unpublished manuscript by Lamb KG.

Solving for U_x^n requires the use of a second order centered difference scheme which provides the initial approximation

$$U_{x,ij} = \frac{U_{i+1,j} - U_{i-1,j}}{2\Delta x}. \tag{3.28}$$

To ensure that no new maxima or minima is added to the velocity field, the following condition on $U_{x,ij}$ is imposed,

$$U_{x,ij} \leq \frac{2}{\Delta x} \cdot \max(|U_{i+1,j} - U_{i,j}|, |U_{i,j} - U_{i-1,j}|), \tag{3.29}$$

or $U_{x,ij}$ is set to 0 if

$$(U_{i+1,j} - U_{i,j}) \cdot (U_{i,j} - U_{i-1,j}) \leq 0. \tag{3.30}$$

The process of determining solution form for ∇p^n involves iteration of the initial data U^n and $\nabla p^{n-\frac{1}{2}}$. First the pressure is initialized by assuming $\nabla p \approx \nabla p^{n-\frac{1}{2}}$, $\nabla p^{n+\frac{1}{2}}$ is then obtained using U^{n+1}. The procedure for this iteration is of the form

$$\nabla p^{n,k} = \frac{1}{2}(\nabla p^{n-\frac{1}{2}} + \nabla p^{n+\frac{1}{2},k}).$$

The tranverse derivatives are estimated using the upwind scheme, for $w \geq 0$, $(U_z)_{ij}$ is obtained from U_{ij} and $U_{i,j-1}$ and for $w < 0$, $(U_z)_{ij}$ is obtained from U_{ij} and $U_{i,j+1}$.

3.5 Generation of Internal Wave Beams

To generate the wave beams, forcing terms are added to the momentum equations. This was discussed in [24] although the model equation used was two-dimensional and only a single forcing was needed. In the present study two forcing terms F and G will be added to the u and w equations respectively. The model equations with the forcing terms added become,

$$\vec{U}_t + \vec{U} \cdot \vec{\nabla}\vec{U} + 2\vec{\Omega} \times \vec{U} = -\vec{\nabla}p - \rho g\hat{k} + (F, 0, G) \tag{3.31}$$

$$\rho_t + \vec{U} \cdot \vec{\nabla}\rho = 0, \tag{3.32}$$

$$\vec{\nabla} \cdot \vec{U} = 0. \tag{3.33}$$

The velocity vector $\vec{U}$ comprises of all three velocity components, but the flow is dependent on two spatial coordinates, x and z, only. F is the forcing in the u equation and G the forcing in the w equation. To force the beams the model uses

$$(F, G) = a_f\omega(\Psi_z, -\Psi_x), \tag{3.34}$$

where a_f controls the forcing amplitude and ω is the forcing frequency. Note that the forcing (3.34) is divergence free. Ψ is given by

$$\Psi(x,z,t) = \exp\left[-\left(\frac{\xi}{a}\right)^4 - \left(\frac{\zeta}{b}\right)^4\right]\cos(kx+mz-\omega t), \tag{3.35}$$

where ξ and ζ are functions of x and z and represent coordinates perpendicular and along the desired beam.

To generate or force internal wave beams, the location of the forcing is first specified. The orientation of the incident beam is then determined by assigning appropriate signs to the horizontal and vertical wave number vectors. The slope of the beam is set using the ratio $\frac{k}{m}$, m is chosen and k is determined from

$$-\frac{k}{m} = \frac{B \pm [B^2 - AC]^{\frac{1}{2}}}{A}, \tag{3.36}$$

k and m are the horizontal and vertical wave numbers respectively. The values of ξ and ζ are given by

$$\begin{cases} \xi = \frac{k}{\sqrt{k^2+m^2}}(x-x_c) + \frac{m}{\sqrt{k^2+m^2}}(z-z_c) \\ \\ \zeta = -\frac{m}{\sqrt{k^2+m^2}}(x-x_c) + \frac{k}{\sqrt{k^2+m^2}}(z-z_c). \end{cases} \tag{3.37}$$

The variables x_c and z_c specifies the centre of the forcing while a and b controls the size of the forcing region in the cross and along beam direction respectively. We will see examples in simulations done with different values of a and b while keeping other variables constant.

The model uses tanh function to smoothly ramp up the forcing. Define

$$g(t) = \frac{1}{2}\left[1 + \tanh\left(\frac{t-t_0}{c_0}\right)\right], \tag{3.38}$$

the overall forcing Ψ routine for a propagating internal wave beam is given by

$$\Psi(x,z,t) = \exp\left[-\left(\frac{\xi}{a}\right)^4 - \left(\frac{\zeta}{b}\right)^4\right] g(t)\cos(kx+mz-\omega t). \tag{3.39}$$

The forcing in the u equation is thus given by

$$F = -\omega a_f \exp\left[-\left(\frac{\xi}{a}\right)^4 - \left(\frac{\zeta}{b}\right)^4\right] g(t)\big(m\sin(kx+mz-\omega t) + A(\xi,\zeta)\cos(kx+mz-\omega t)\big), \tag{3.40}$$

where

$$A(\xi,\zeta) = \frac{4}{\sqrt{k^2+m^2}}\left[\frac{m}{a}\left(\frac{\xi}{a}\right)^3 + \frac{k}{b}\left(\frac{\zeta}{b}\right)^3\right]$$

while the forcing in the w equation is given by

$$G = \omega a_f \exp\left[-\left(\frac{\xi}{a}\right)^4 - \left(\frac{\zeta}{b}\right)^4\right] g(t)\big(k\sin(kx+mz-\omega t) - B(\xi,\zeta)\cos(kx+mz-\omega t)\big), \tag{3.41}$$

where

$$B(\xi,\zeta) = \frac{4}{\sqrt{k^2+m^2}}\left[\frac{k}{a}\left(\frac{\xi}{a}\right)^3 - \frac{m}{b}\left(\frac{\zeta}{b}\right)^3\right]$$

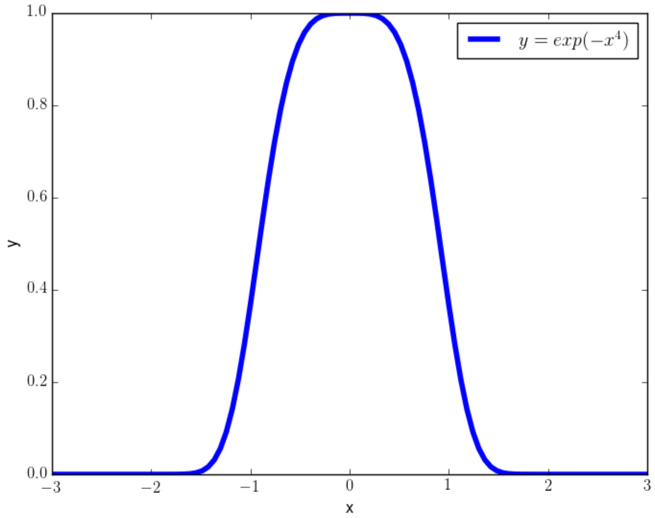

Figure 3.4: Schematic showing the shape of the forcing wave envelope in the along cross or along beam direction.

Figure (3.4) shows the profile of the envelope of an internal wave beam. It shows a cross-section of the shape of the envelope. In performing simulations, the function $y = \exp(-(\frac{x}{a})^4)$ was used to modulate the wave amplitude. If this represents the coefficient of the cosine term in (3.35) then the amplitude of the wave envelope is 1.

Figure (3.5) shows the horizontal velocity field of propagating internal wave beam forced at $(0, -\frac{H}{2})$, the wave beam spreads and reflects off the flat bottom generating second harmonic beam. The parameter settings used for the simulation are $N = 3.0 \times 10^{-4}\,\mathrm{rad}\,s^{-1}$, $\omega = 1.4 \times 10^{-4}\,\mathrm{rad}\,s^{-1}$, $m = \frac{2\pi}{100}\mathrm{m}^{-1}$, $f = f_h \approx 1.0338 \times 10^{-4}\mathrm{rad}\,\mathrm{s}^{-1}$, $a = 50\mathrm{m}$, $b = 100\mathrm{m}$. The time is in the format hh:mm:ss.

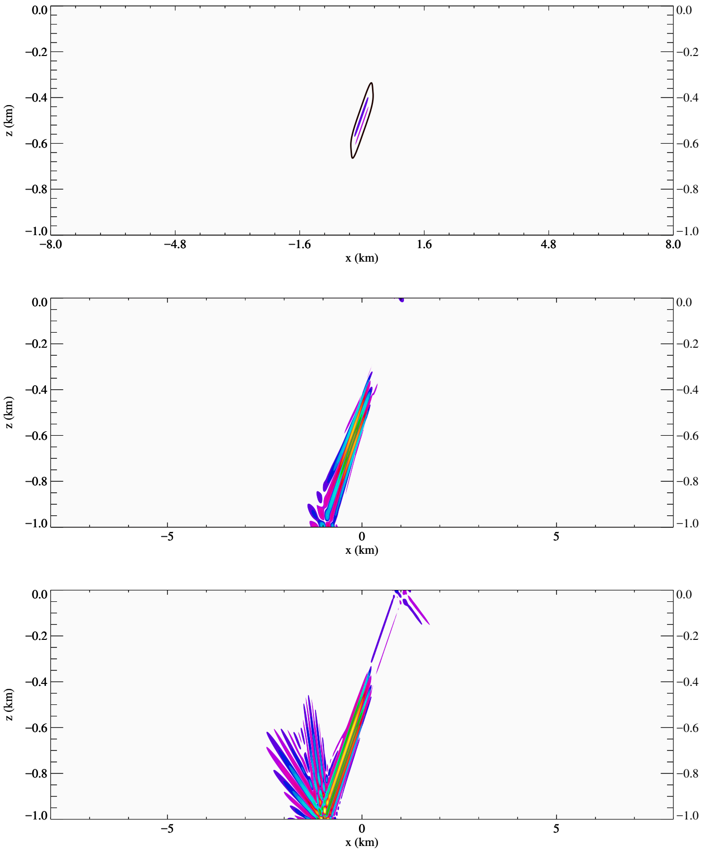

Figure 3.5: Results from a numerical simulation showing the stages of propagation of internal wave beam. The timings starting with the topmost panel are t = 13:20:00, t=83:20:00, and t= 166:40:00

In figures (3.6) – (3.8) showing horizontal velocity profile and its vertical profile we vary the values of a and b while keeping other parameters constant. For each of the numerical simulation done for these cases the vertical profile of the horizontal velocity field is shown. The parameter settings in common to all the simulations are, $N = 3.0 \times 10^{-4}\,\mathrm{rad}\,s^{-1}$, $\omega = 1.4 \times 10^{-4}\,\mathrm{rad}\,s^{-1}$, $m = \frac{2\pi}{100}\mathrm{m}^{-1}$, $\theta = \frac{\pi}{4}$, $\phi = \frac{\pi}{2}$, the vertical profile for each case was taken at $x = -100$ and for frame 1000. Observation shows that the values of a and b modulates the characteristic coordinates in time which in turn affects the way the internal wave propagate. The time format is hh:mm:ss that is hours, minutes and seconds.

We observe that increasing the value of b increases the length of the forcing region in the along beam direction, increasing a increases it in the cross-beam direction. This is apparent from the figures above. From the vertical profile we observe that for $a = 50$ m the vertical wavelength is a bit less than 100m. For $a = 100$m the vertical wavelength in the packet is closer to 100 m in the center of the packet and the packet has a larger vertical extent. In the simulations presented in Chapter (4) we use $a = 50$ m, apparently the value of b does not affect the wavelength of the waves so we use $b = 350$ m for most of the simulations for convenience.

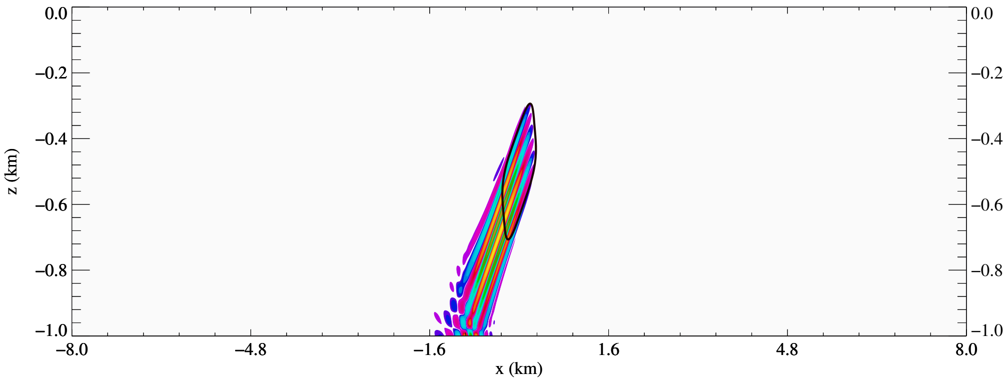

(a) Here $a = 100$m, $b = 100$m, t $=$ 100:00:00 hours.

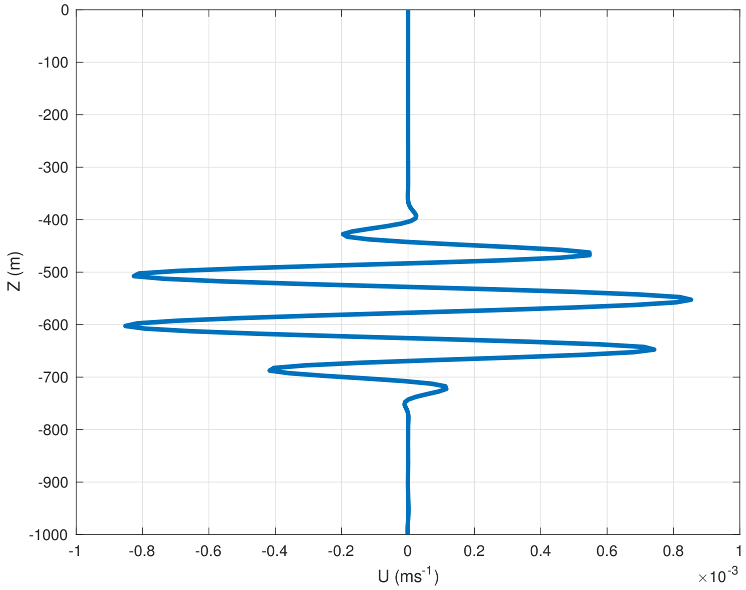

(b) Vertical profile

Figure 3.6: Internal wave beam and corresponding vertical profile.

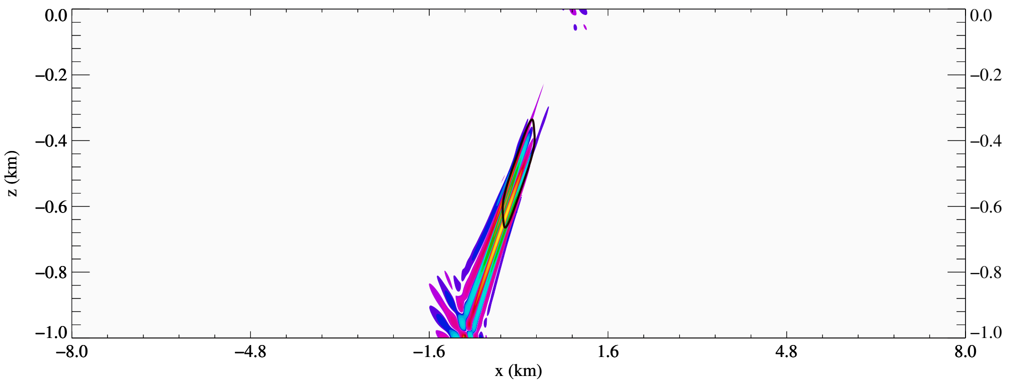

(a) Here a = 50m, b = 100m, t = 100 hours.

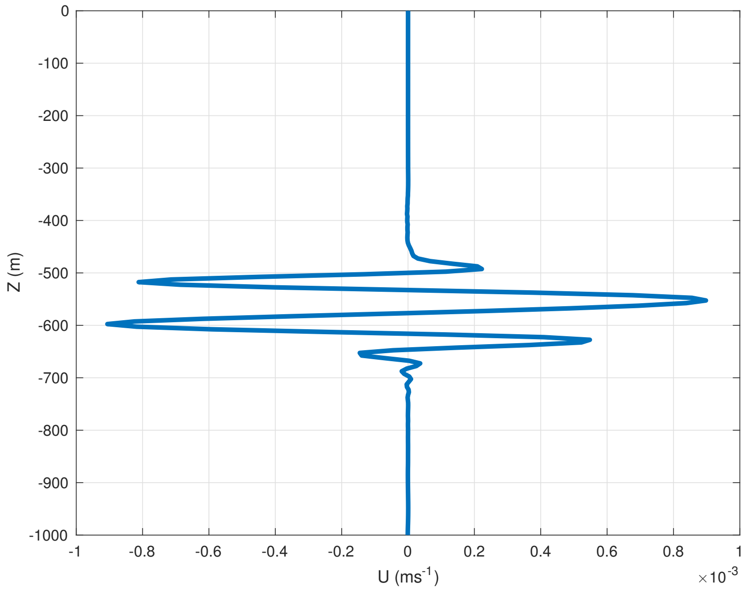

(b) Vertical profile

Figure 3.7: Internal wave beam and corresponding vertical profile.

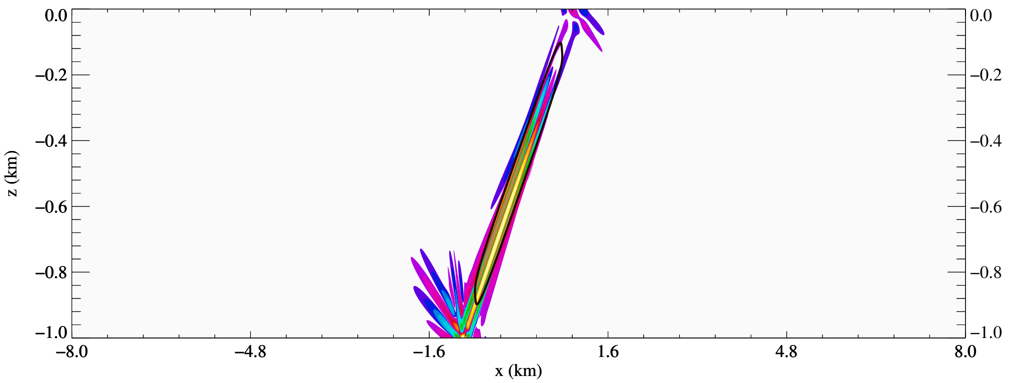

(a) Here a = 50m, b = 700m, t = 100 hours.

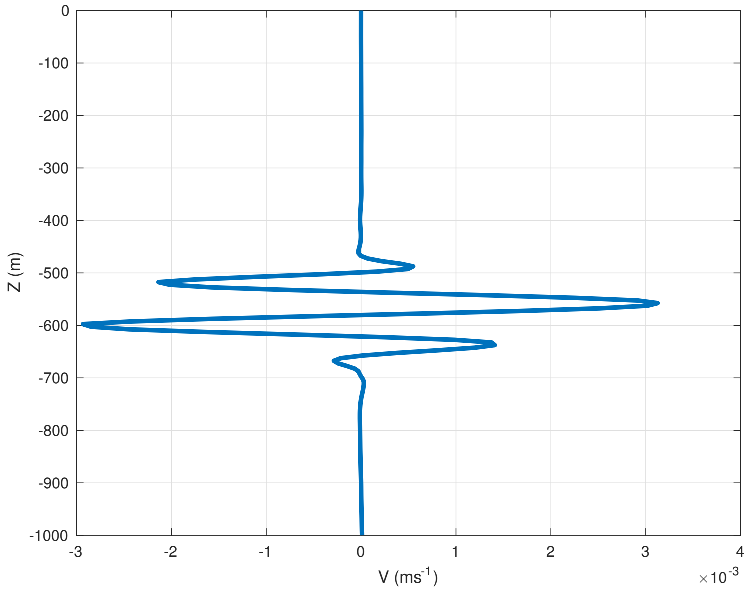

(b) Vertical profile

Figure 3.8: Internal wave beam and corresponding vertical profile.

Chapter 4

Results

This chapter is divided into five sections. Analysis of reflection based on group velocity and phase speed is given in section (4.1). Recall that the dispersion relation is given by

$$\omega^2 = \frac{N^2k^2 + 2f\tilde{f}km + f^2m^2 + \tilde{f}^2k^2}{k^2 + m^2}. \tag{4.1}$$

The group velocity is given by

$$\vec{v}_g = (\omega_k, \omega_m) = \frac{1}{\omega(k^2+m^2)^2}\big((N^2 + \tilde{f}^2 - f^2)mk + f\tilde{f}(m^2 - k^2)\big)(m, -k), , \tag{4.2}$$

and the phase speed is

$$\vec{v}_p = \frac{1}{(k^2+m^2)}\left(\frac{N^2k^2 + 2f\tilde{f}km + f^2m^2 + \tilde{f}^2k^2}{k^2 + m^2}\right)^{\frac{1}{2}}(k, m). \tag{4.3}$$

Section (4.2) contains some results from numerical simulations of reflection of internal waves of super-inertial, inertial and sub-inertial frequencies from constant slope. In section (4.3) we discuss the generation of second harmonics from colliding beams with a rule guiding this process. Spectral analysis of time series obtained from moorings is discussed in sections (4.4) and (4.5), the analysis and discussion is centered on primary and secondary harmonic beams resulting from reflection from a uniform slope and flat bottom and colliding beams. As mentioned in the introduction the analysis of colliding beams done in this thesis is based on the formation rule by Chung-Hsiang which predicts the generation of second harmonics from colliding beams with horizontal group velocity of the same sign. The formation rule does not involve solving PDEs rather it uses the orientation of the colliding beams with respect to the dispersion relation and radiation conditions to predict the generation of higher harmonics. Note that the times presented here are in the format hh:mm:ss that is hours, minute and seconds.

4.1 Analysis of Reflection

Figure (4.1) illustrates the inter-play between the frequencies associated with the incident beam and the reflected beam without the traditional approximation. The effect of the non-traditional approximation is seen by the asymmetry in the graph. An important observation from this plot is that the incident and the reflected beams are not equally steep when the traditional approximation is abandoned. Secondly the sub-inertial frequencies constitute a smooth continuation to the super-inertial branch as the horizontal green line show. In the plots and numerical simulations, vertical wave number of the incident beam is given by

$$m_I = \frac{2\pi}{100}\,\mathrm{m}^{-1}. \tag{4.4}$$

The horizontal wave number may be obtained using

$$\frac{k_I}{m_I} = \frac{-B - \sqrt{B^2 - AC}}{A}. \tag{4.5}$$

The vertical wave number of the reflected beam can be expressed in terms of the incident beam as follows

$$m_R = \wp^{+} m_I, \tag{4.6}$$

where $\wp^{+}$ is defined by equation (2.184). The horizontal wave number of the reflected beam with respect to the topography may then be given by,

$$k_R = k_I + \beta(1 - \wp^{+})m_I, \tag{4.7}$$

if $\beta = 0$, flat bottom is implied. Note that for ξ characteristic coordinate $\wp^{-}$ represents a wave that propagates through the slope and hence not of interest. For all cases presented here f represents the inertial frequency.

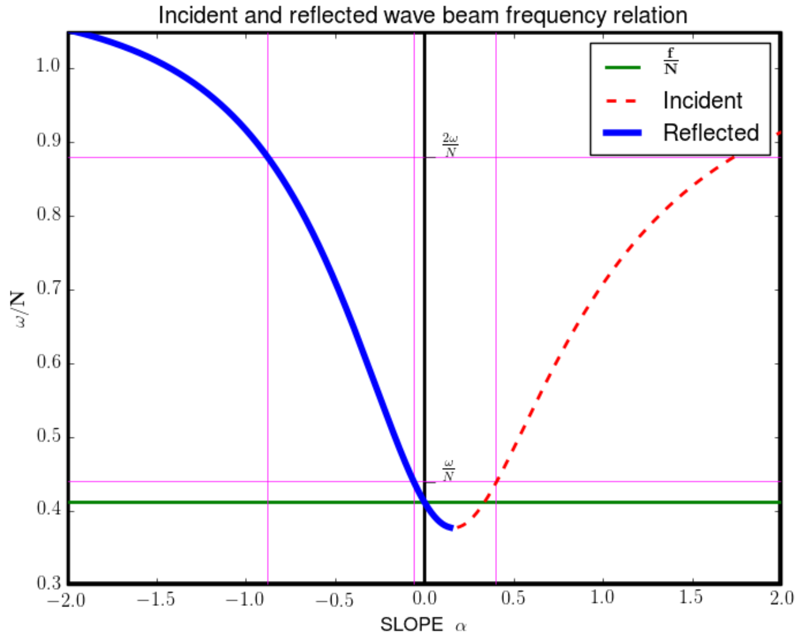

Figure 4.1: Schematic illustrating the relationship between the frequencies of the incident beam and the reflected beam for an arbitrary range of frequencies. Parameter values are $N = 2.5 \times 10^{-4}$ rad s^{-1}, $f = f_h = 1.0338 \times 10^{-4}$ rad s^{-1}. The right branch represents $\alpha = \mu_+$; the left branch represents $\alpha = \mu_-$. The frequencies illustrated here are $\omega = 1.1 \times 10^{-4}$ rad s^{-1} and $\omega = 2.2 \times 10^{-4}$ rad s^{-1}, the green line demarcates the sub-inertial and super-inertial frequencies. Information obtained from the graph shows that the slope of the beams forced at frequency ω are 0.4, -0.06, and -0.9 for the incident, first and second harmonic respectively for reflection off a flat bottom.

In figure (4.2) the relationship between the group velocity and phase speed of an incident wave beam is shown. The parameter settings are listed in table (4.1). The frequencies have been scaled by the buoyancy frequency N while the group velocities and phase speed have been scaled by $U = NH$, $H = 1000$m. Thus on the vertical axis we are plotting $\frac{v_g}{U}$ and $\frac{v_p}{U}$, while $\frac{\omega}{N}$ is on the horizontal axis.

It can be observed from figure (4.2a) which represents the non-traditional μ_+ curve that at sub-inertial frequencies the phase speed is greater than the group velocity. This order reverses at the inertial frequency and the group velocity becomes greater up to the threshold $\frac{\omega}{N} = 0.71$ beyond this threshold the phase speed is again greater than the group

$N(\mathrm{rad\,s^{-1}})$	$f\ (\mathrm{rad\,s^{-1}})$	$f_h\ (\mathrm{rad\,s^{-1}})$	θ (rad)	ϕ (rad)	$m\ (\mathrm{m^{-1}})$
2.5×10^{-4}	1.0338×10^{-4}	1.0338×10^{-4}	$\frac{\pi}{4}$	$\frac{\pi}{2}$	$\frac{2\pi}{100}$

Table 4.1: Parameter settings for figures (4.2) – (4.7).

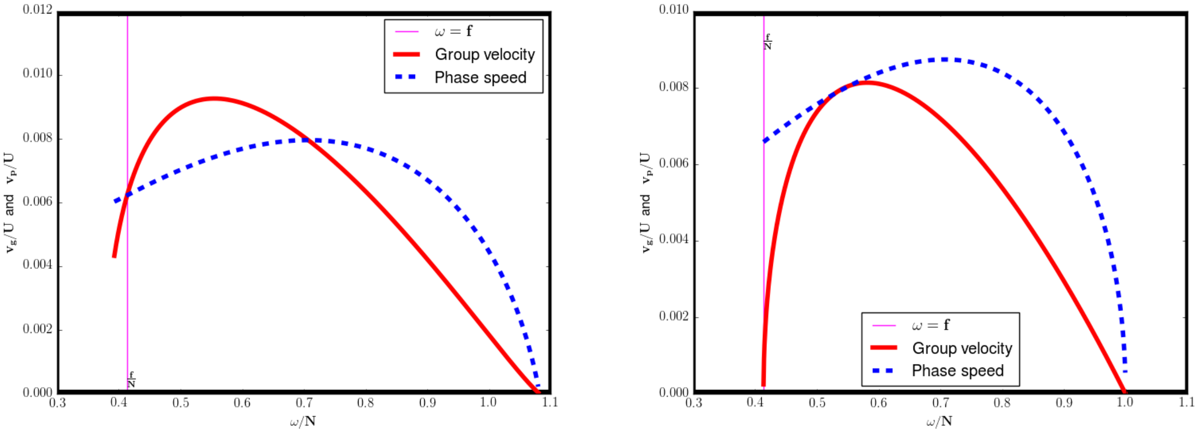

(a) Without the traditional approximation.

(b) With the traditional approximation.

Figure 4.2: Showing the scaled group velocity and phase speed vs scaled wave frequency of incident beam with and without the traditional approximation for ξ characteristics.

velocity and both decrease and tend to zero as ω tends to $\sqrt{N^2 + f_h^2}$. In figure (4.2b) showing the traditional approximation (note that for this case $\mu_+ = \mu_-$ since $f_h = 0$), reflected and incident waves have the same group velocity if the bottom is flat. Inertial and sub-inertial waves are absent for this case and the wave frequency does not exceed the bouyancy frequency. The thin line marks the inertial frequency which is defined by f.

From figure (4.2a) where we showed the plot of the incident beam for ξ characteristics we observed that the group velocity and phase speed decreases for higher frequencies, the vertical wavenumber and buoyancy frequency were fixed, hence the horizontal wavenumber k varies with frequency. Figure (4.3) shows the relationship between the group velocity and phase speed of the reflected beam (reflection of beams propagating along ξ characteristics) as a function of the incident beam. In this case both the horizontal and vertical wavenumbers are varying with wave frequency ω as can be observed from equations (4.6) and (4.7). The group velocity and phase speed of the beams reflecting off a flat bottom decreases to zero as ω tends to f and $\sqrt{N^2 + f_h^2}$.

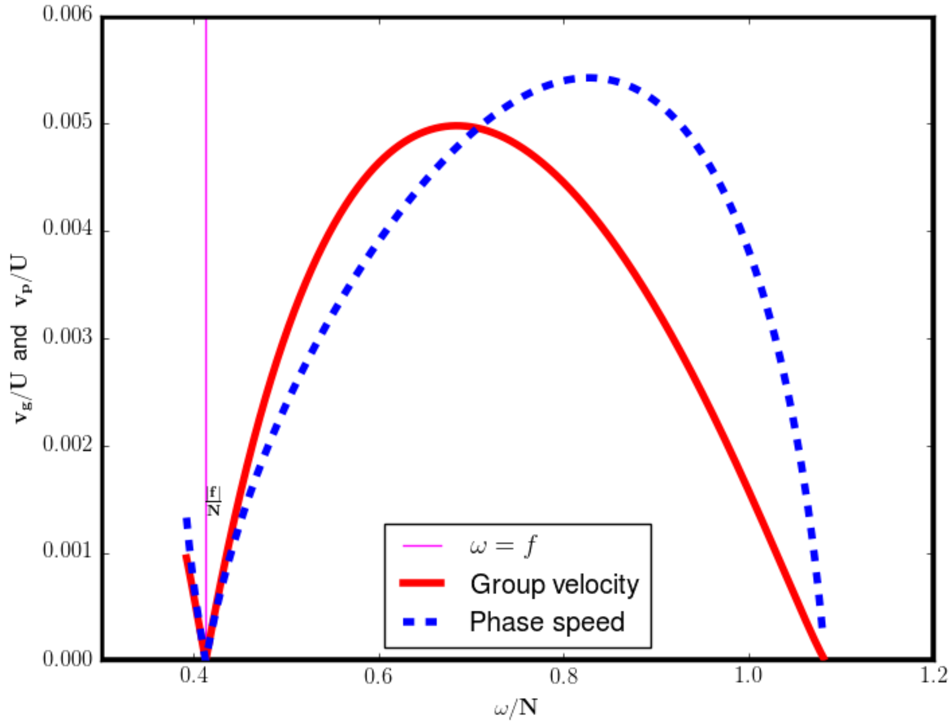

Figure 4.3: Shows the relationship between the group velocity and phase speed of beams reflecting from a flat bottom without the traditional approximation.

The second characteristic η given by equation (4.9) is shown in figure (4.4), note that for this characteristic when $\omega = f$ (that is at the inertial frequency) the slope of the beam is zero since the horizontal wave number k (which is predominantly negative for positive values of m) is zero when $\omega = f$ for any value of the vertical wave number m. With the analysis leading to figures (4.2a) and (4.4) we are able to determine the group velocity and phase speed of second harmonics generated from two colliding wave beams.

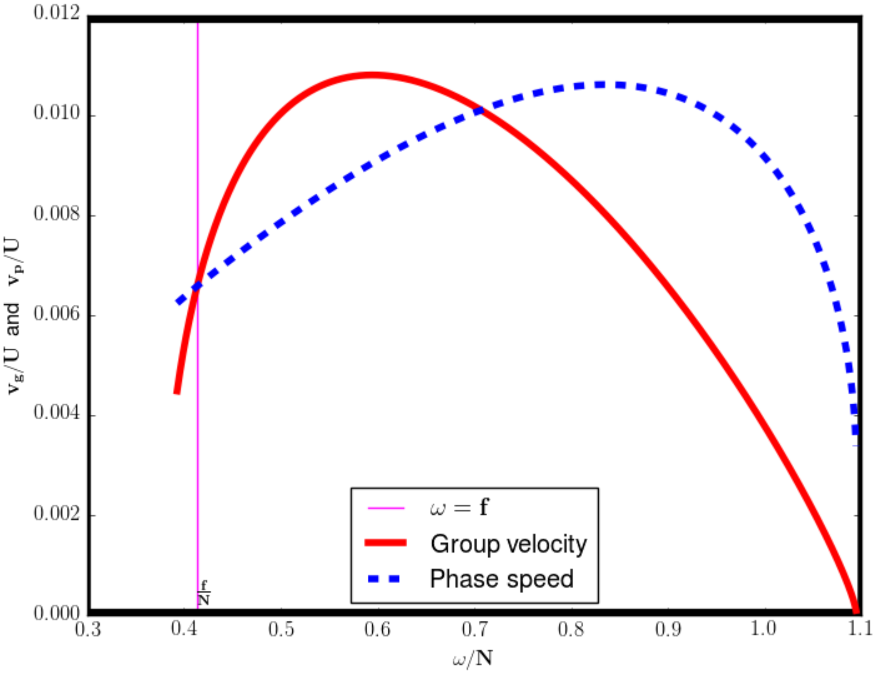

Figure 4.4: Group velocity and phase speed of incident beam for η without the traditional approximation. At sub-inertial frequencies the group velocity is less than the phase speed. This order reverses at the inertial frequancy and the group velocity becomes greater until the threshold $\frac{\omega}{N} = 0.71$ is reached. The group velocity attains maximum at $\frac{\omega}{N} = 0.6$ while the phase speed is maximum at $\frac{\omega}{N} = 0.87$. The group velocity tends to zero as $\frac{\omega}{N}$ tends to $\frac{\omega_{\max}}{N} = 1.1$

In colliding beams the two beams involved in the collision belong to one of two characteristic curves. The first incident beam propagates along ξ characteristic

$$\frac{k_1}{m_1} = \frac{B + \sqrt{B^2 - AC}}{A}, \tag{4.8}$$

while the second incident beam propagates along η characteristic

$$\frac{k_2}{m_2} = \frac{B - \sqrt{B^2 - AC}}{A}, \tag{4.9}$$

the rule governing the generation of the second harmonic beams resulting from the two colliding beams may be determined using (4.8) and (4.9) via

$$\frac{k^H}{m^H} = \frac{k_1 + k_2}{m_1 + m_2} \quad \text{and} \quad \frac{k_1 - k_2}{m_1 + m_2}, \tag{4.10}$$

for the $\omega_1 + \omega_2$ and $\omega_2 - \omega_1$ wave frequencies respectively. This will be discussed in greater detail in section (4.3).

4.1.1 Interplay between f and f_h

In this section we present some plots that show how the magnitudes of the buoyancy frequeny N, the non-traditional term f_h and the inertial frequency f influence the relation between the frequency and slope of internal wave beams. Recall that the range of allowable frequencies in the non-traditional approximation is $\omega^2_{\text{min}} < f^2 < N^2 + f_h^2 < \omega^2_{\text{max}}$ whereas in the traditonal approximation the range of frequencies is $f^2 < \omega^2 < N^2$. We will consider cases for which $f_h = 2f$, $f_h = f, f_h = \frac{f}{2}$ and $f = 0$. The values of the parameters used in producing these plots are given in table (4.1).

For the case with $f_h = 2f$ (Figure (4.5a)) we find that, $\omega_{\text{min}} = 7.8 \times 10^{-5}\text{rad}\,\text{s}^{-1}$, $\sqrt{N^2 + f_h^2} = 3.24 \times 10^{-4}\text{rad}\,\text{s}^{-1}$, $\omega_{\text{max}} = 3.31 \times 10^{-4}\text{rad}\,\text{s}^{-1}$. However when $f_h = f$ (figure (4.5b)) $\omega_{\text{min}} = 9.44 \times 10^{-5}\text{rad}\,\text{s}^{-1}$, $\sqrt{N^2 + f_h^2} = 2.705 \times 10^{-4}\text{rad}\,\text{s}^{-1}$, $\omega_{\text{max}} = 2.738 \times 10^{-4}\text{rad}\,\text{s}^{-1}$.

For the case with $f_h = \frac{f}{2}$ (Figure (4.6a)) $\omega_{\text{min}} = 1.01 \times 10^{-4}\text{rad}\,\text{s}^{-1}$, $\sqrt{N^2 + f_h^2} = 2.55 \times 10^{-4}\text{rad}\,\text{s}^{-1}$, $\omega_{\text{max}} = 2.56 \times 10^{-4}\text{rad}\,\text{s}^{-1}$. When $f = 0$ (Figure (4.6b)) we find that $f = 0, \quad \omega_{\text{min}} = 0, \sqrt{N^2 + f_h^2} = \omega_{\text{max}} = 2.71 \times 10^{-4}\text{rad}\,\text{s}^{-1}$.

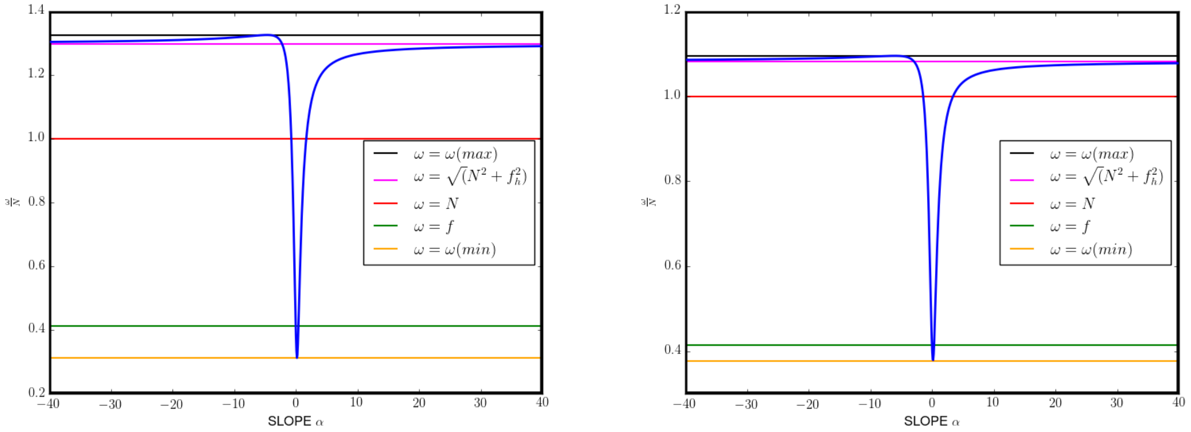

(a) $f_h = 2f$

(b) $f_h = f$

Figure 4.5: Plots of scaled wave frequency $\frac{\omega}{N}$ vs beam slope α for varying values of f and f_h, the values of f and f_h are given in table (4.1).

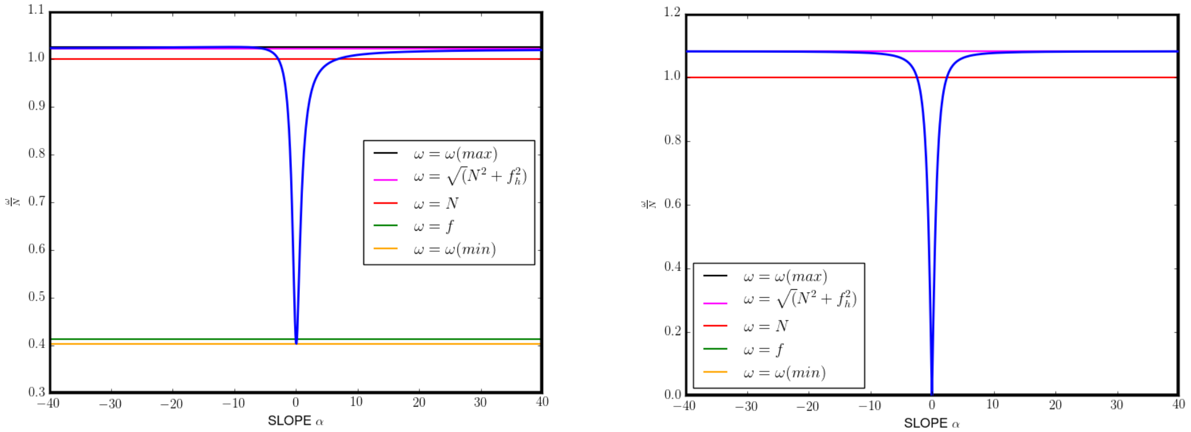

(a) $f_h = \frac{f}{2}$

(b) $f = 0$

Figure 4.6: Plots of scaled wave frequency $\frac{\omega}{N}$ vs beam slope α for $f_h = \frac{f}{2}$ and $f = 0$, see table (4.1) for f and f_h.

In figure (4.7) the buoyancy frequency is increased to twice its original value and now $\omega_{\text{min}} = 1.01 \times 10^{-4}\text{rad}\,\text{s}^{-1}$, $\sqrt{N^2 + f_h^2} = 5.106 \times 10^{-4}\text{rad}\,\text{s}^{-1}$, $\omega_{\text{max}} = 5.11 \times 10^{-4}\text{rad}\,\text{s}^{-1}$.

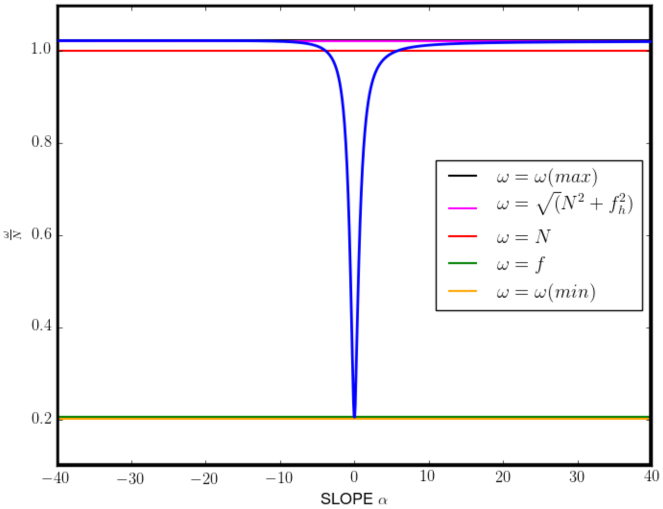

Figure 4.7: $f_h = f$ and $N = 5.0 \times 10^{-4} \mathrm{rad\, s^{-1}}$

We can observe from figures (4.5) – (4.7) that making f_h larger than f generally increases the range of allowable frequencies, that is $\omega_{\min}$ decreases and $\omega_{\max}$ increases. Also notice that $\omega_{\min}$ tends to f and $\omega_{\max}$ tends to N as f_h goes to zero. From figure (4.6b) when $f = 0$, $\omega_{\min} = 0$ and $\omega_{\max} = \sqrt{N^2 + f_h^2}$, thus the effect of the non-traditional approximation is dominant at higher frequencies when the inertial frequency is taken to be zero since the range of allowable frequencies is now $0 < \omega^2 < \sqrt{N^2 + f_h^2}$. Also notice from figure (4.7) that for an increased buoyancy frequency $\omega_{\min}$ tends to f and $\omega_{\max}$ tends to $\sqrt{N^2 + f_h^2}$ therefore the frequency interval is decreased. Hence non-traditional effects are dominant for near inertial waves and for weak stratification. In making the traditional approximation waves exist between the green and red lines that is between the inertial frequency f and the buoyancy frequency N. The right half of the plots cover critical slopes oriented northwards while the left half covers critical slopes oriented southwards.

In section (4.2) we present results from numerical simulations showing horizontal velocity field for cases of reflection of waves of super-inertial, inertial and sub-inertial frequencies from varying slopes typically for $\beta = 0, -0.02, -0.1$. In doing the simulations the following parameter settings defined by table (4.2) were used

N (rad s^{-1})	f (rad s^{-1})	f_h (rad s^{-1})	θ (rad)	ϕ (rad)	mm^{-1}	a (m)	b (m)	a_f (m)
2.5×10^{-4}	1.0338×10^{-4}	1.0338×10^{-4}	$\frac{\pi}{4}$	$\frac{\pi}{2}$	$\frac{2\pi}{100}$	50	350	0.0025

Table 4.2: Parameter settings for the numerical simulation of reflection of internal wave beams (figures (4.8) – (4.15)), m is the vertical wave number of the incident beam, a and b controls the width of the beam in the across beam and along beam direction respectively.

4.2 Reflection from Uniform Slope

Reflected waves carry energy and information away from the slope, this process is controlled by the group velocity which is the velocity of energy propagation. In figures (4.8), (4.9), and (4.10) showing horizontal velocity fields we consider three cases of super-inertial wave beam reflection from boundaries. The interest here is to observe how the propagation of the reflected beams is influenced by the bottom topography. Critical reflection occurs when the angle the incident beam makes with the horizontal is the same as the slope inclination ϕ, for then the group velocity of the reflected wave is directed along the slope, and the wave vector is perpendicular to the slope. For figures (4.8)–(4.10) showing waves of super-inertial frequency the frequency of the incident beam is $\omega = 1.2 \times 10^{-4}$ rad s^{-1} with group velocity 2.17×10^{-3}m s^{-1}.

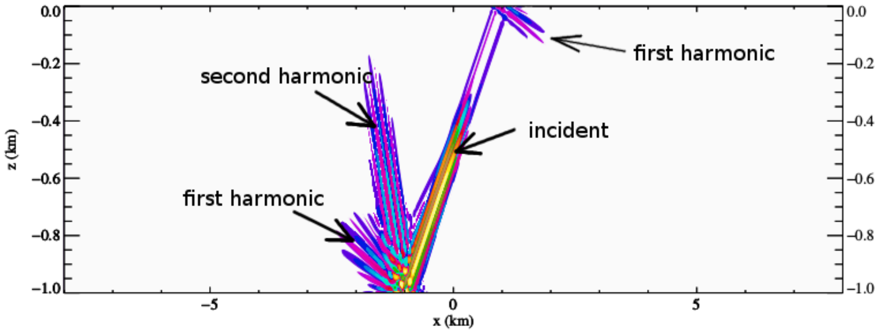

Figure 4.8: Result from a numerical simulation of reflection of internal waves from a flat bottom (and reflection from a flat top) at t=150:40:40. The reflected first harmonic beam propagates with group velocity 6.26×10^{-4}m s^{-1} while the second harmonic propagates with group velocity 5.77×10^{-4}m s^{-1}.

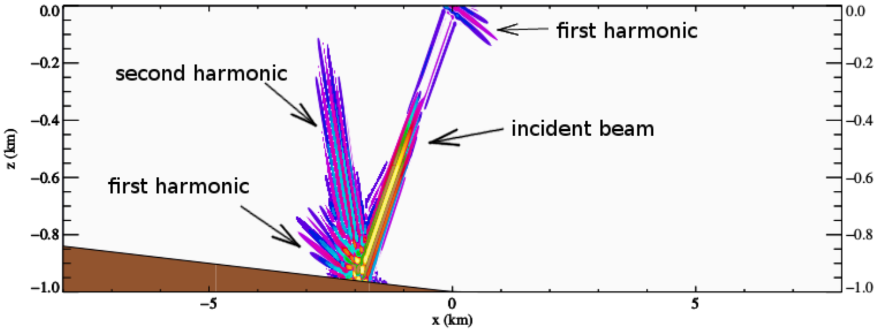

Figure 4.9: Reflection from a uniform slope $\beta = -0.02$ at t=150:40:00. The reflected first harmonic beam propagates with $5.28 \times 10^{-4}\mathrm{m\,s^{-1}}$ group velocity while the second harmonic propagates with group velocity $5.72 \times 10^{-4}\mathrm{m\,s^{-1}}$.

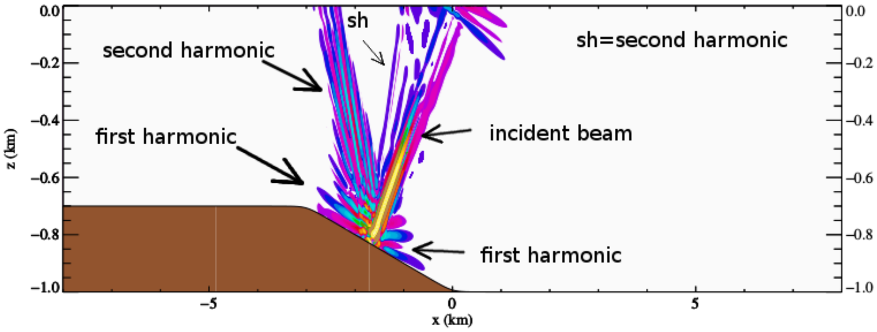

Figure 4.10: Reflection of internal wave beam from a much steeper slope $\beta = -0.1$ at t=150:40:00. The reflected first harmonic beam propagates with $1.22 \times 10^{-4}\mathrm{m\,s^{-1}}$ group velocity while the second harmonic propagates with group velocity $5.5 \times 10^{-4}\mathrm{m\,s^{-1}}$.

Observations from figures (4.8), (4.9), and (4.10) indicate that a uniform slope generally reduces the group velocity of reflected wave beams of super-inertial frequency, this reduction effect is greater for the first harmonic than it is for the second harmonic. Also, the steepness of the bottom slope affects upslope propagation of first harmonic reflected beams by causing some waves to propagate downslope for sufficiently steep bottom. Steep negative slopes enhances the generation of second harmonics.

As already mentioned, the non-traditional approximation enlarges the frequency interval of propagation of internal waves so that waves of inertial and sub-inertial frequencies now exist. Figures (4.11), (4.12) and (4.13) shows reflection of internal wave beams of inertial frequency ($\omega = f$) from a flat bottom and sloping boundaries. At inertial frequencies a flat bottom is critical because reflected inertial waves propagate horizontally thus coincides with the direction of the flat bottom. The incident beam for the three cases propagates with group velocity $1.557 \times 10^{-3}\mathrm{m\,s^{-1}}$.

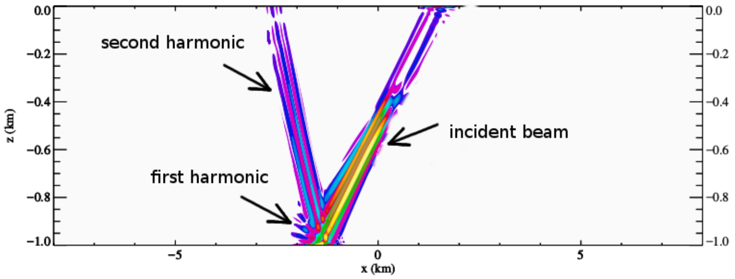

Figure 4.11: Reflection of internal wave of inertial frequency f off a flat bottom at t=321:20:00. The first harmonic reflected beam propagates at $4.6 \times 10^{-8}\mathrm{m\,s^{-1}}$ while the second harmonic propagates with group velocity $1.05 \times 10^{-3}\mathrm{m\,s^{-1}}$.

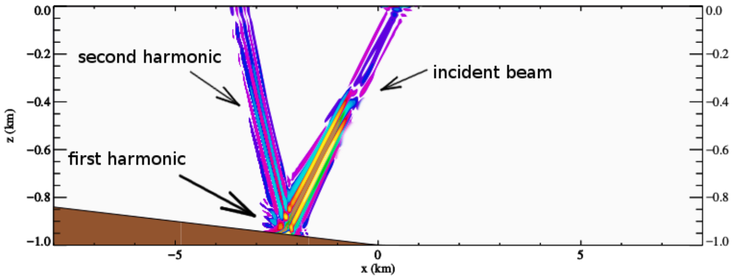

Figure 4.12: Result from numerical simulation with the same settings as in figure (4.11) but for a uniform slope $\beta = -0.02$ at t=321:20:00. The first harmonic reflected beam propagates at $9.53 \times 10^{-5}\mathrm{m\,s^{-1}}$ while the second harmonic propagates with group velocity $1.03 \times 10^{-3}\mathrm{m\,s^{-1}}$.

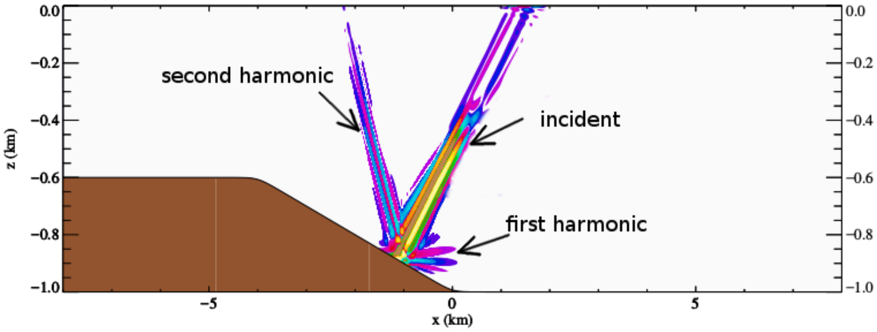

Figure 4.13: Again the same settings as in figure (4.11) but for a much steeper slope $\beta = -0.1$ at t=321:20:00. The reflected first harmonic is oriented horizontally to the right and propagates with group velocity $4.48 \times 10^{-4}\mathrm{m\,s^{-1}}$, while the second harmonic propagates with group velocity $9.3 \times 10^{-4}\mathrm{m\,s^{-1}}$.

Figures (4.14) and (4.15) show results from numerical simulations of reflection of wave beams of sub-inertial frequency $\omega = 0.95f$. We consider the case of a flat bottom and uniform slope $\beta = -0.1$. The incident beam propagate with group velocity $1.08 \times 10^{-3}\mathrm{m\,s^{-1}}$.

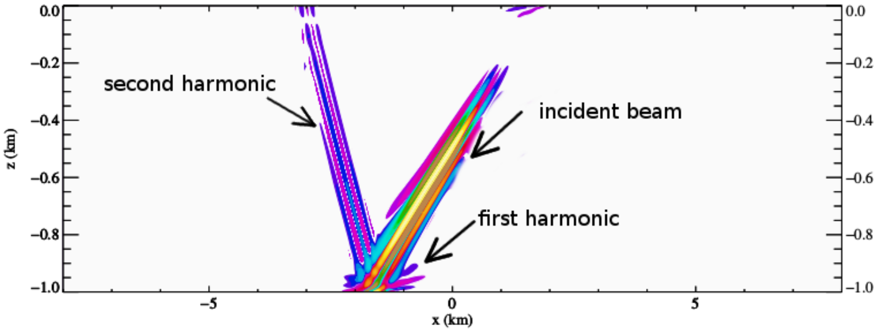

Figure 4.14: Reflection of sub-inertial wave beam from a flat bottom $\beta = 0$ at t=416:40:00. The first harmonic reflected beam propagates with group velocity $1.46 \times 10^{-4}\mathrm{m\,s^{-1}}$ while the second harmonic propagates with group velocity $1.1 \times 10^{-3}\mathrm{m\,s^{-1}}$.

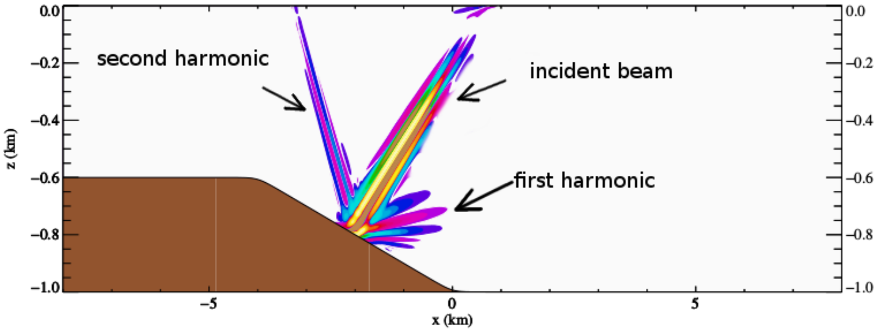

Figure 4.15: Reflection of sub-inertial wave beam from a sloping boundary $\beta = -0.1$ at t=416:40:40. The reflected first harmonic is oriented horizontally to the right and propagates at $6.04 \times 10^{-4}\mathrm{m\,s^{-1}}$ group velocity, whereas the second harmonic propagates at $9.66 \times 10^{-4}\mathrm{m\,s^{-1}}$ respectively.

Comparing group velocities (see figures (4.2a) - (4.3) for group velocity and phase velocity plots), we see that for inertial and sub-inertial frequencies increasing the bottom slope increases the group velocity of the first harmonic reflected beam while decreasing that of the second harmonic unlike in the super-inertial case where the group velocities of the first and second harmonic reflected beams are decreased when the bottom slope increases in magnitude. We also observe that inertial waves are associated with horizontal motion. This can be seen from figures (4.13) and (4.15) where the topography causes the reflected beam to propagate horizontally and opposite in direction to the second harmonic. Another thing to notice in the inertial and sub-inertial simulations is that the second harmonic beams are more pronounced for horizontal bottom than for a sloping boundary, thus sloping boundaries diminishes the generation of second harmonic beam because it is narrower. This is in contrast with the super-inertial waves where the slopping boundary enhances the generation of second harmonics.

From figure (4.1) we observed that for every wave frequency there are two values of the slope of a beam. Figure (4.16) shows results from a numerical simulation of the reflection of a super-inertial beam from a uniform slope $\beta = -0.06$. The run for this simulation is for a much longer time than in previous simulations. It shows the reflection of the second harmonic beam from the upper and lower boundaries. We observe that there are four distinct beam slopes. Two of these values (1.7 and -0.9) are associated with the steeper second harmonic beams and the other two values (0.4 and -0.06) are associated with the first harmonic beams. Note that the reflection of the second harmonic doesn't generate fourth harmonic beams because $4\omega > \omega_{\max}$. The values of the parameters used for this simulation is given in table (4.2). The incident beam has frequency $\omega = 1.1 \times 10^{-4} \mathrm{rad\,s^{-1}}$. This is comparable to figure (4.1) which shows the plot of beam slope against frequency and in particular indicates the values of slope shown here.

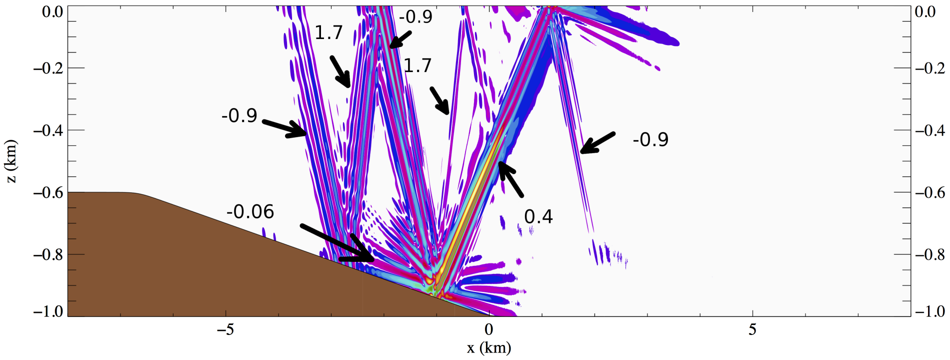

Figure 4.16: Numerical simulation showing reflection of a super-inertial beam from a sloping wall and the slope values for each beam. The arrows connect each of the beams to the corresponding value of slope. Time stamp for this simulation is t=300:00:00

4.3 Generation of Second Harmonics from Colliding beams

The basis for this section is the PhD thesis by Chung-Hsiang Jiang at the Department of Mechanical Engineering, University of Carlifornia, Berkely [18]. It is focused on colliding internal wave beams and generation of higher harmonics. A rule guiding the generation of higher harmonics from colliding internal wave beams depending on collision configuration is presented. The colliding beams considered in the work by Chung-Hsiang Jiang involves wave beams of the same frequency with $f \neq f_h$ in general. We went further to consider wave beams of different frequencies and assumed (in the numerical simulations) that f_h and f are equal as well as incoporating phase speed and group velocities in our analysis. The rule presented in our work is in agreement with the rule by Chung-Hsiang Jiang. The section starts with a three-dimensional analysis of group velocity and phase speed.

Let $\vec{f}$ represent the complete rotation vector,

$$\vec{f} = f_x \mathbf{e}_x + f_y \mathbf{e}_y + f_z \mathbf{e}_z, \tag{4.11}$$

where f_x, f_y, f_z are constants. For a constant buoyancy frequency N the general dispersion relation has the form

$$\omega^2 = \frac{\kappa_h^2}{\kappa^2} N^2 + \frac{(\vec{\kappa} \cdot \vec{f})^2}{\kappa^2} = \frac{k^2 + l^2}{k^2 + l^2 + m^2} N^2 + \frac{(k f_x + l f_y + m f_z)^2}{k^2 + l^2 + m^2}, \tag{4.12}$$

all variables retain their usual meaning. We can derive the phase velocity $\vec{v}_p$ and group velocity $\vec{v}_g$ from (4.12).

Phase velocity is given by

$$\vec{v}_p = \frac{\omega}{\kappa} \frac{\vec{\kappa}}{\kappa} = \left[\frac{\kappa_h^2}{\kappa^2} N^2 + \frac{(\vec{\kappa} \cdot \vec{f})^2}{\kappa^2} \right] \frac{\vec{\kappa}}{\omega \kappa^2} \tag{4.13}$$

The group velocity in three-dimensions may be obtained using,

$$\vec{v}_g = \left(\frac{\partial \omega}{\partial k}, \frac{\partial \omega}{\partial l}, \frac{\partial \omega}{\partial m} \right). \tag{4.14}$$

To obtain the x-directional group velocity we take the k-derivative of (4.12) and simplify to get

$$\omega \frac{\partial \omega}{\partial k} = \frac{k[N^2 m^2 - (\vec{\kappa} \cdot \vec{f})^2]}{\kappa^4} + \frac{f_x (\vec{\kappa} \cdot \vec{f})}{\kappa^2}. \tag{4.15}$$

Multiplying both side of equation (4.15) by $\omega\kappa^2$ gives

$$\omega^2\kappa^2\frac{\partial\omega}{\partial k} = \frac{\omega k[N^2m^2 - (\vec{\kappa}\cdot\vec{f})^2]}{\kappa^2} + \omega f_x(\vec{\kappa}\cdot\vec{f}). \tag{4.16}$$

From (4.12) we have that

$$\frac{(\vec{\kappa}\cdot\vec{f})^2}{\kappa^2} = \omega^2 - \frac{\kappa_h^2}{\kappa^2}N^2. \tag{4.17}$$

Applying this to (4.16) and simplifying gives

$$\frac{\partial\omega}{\partial k} = \frac{(N^2-\omega^2)k + f_x(\vec{\kappa}\cdot\vec{f})}{\omega\kappa^2}. \tag{4.18}$$

In the same fashion $\dfrac{\partial\omega}{\partial l}$ and $\dfrac{\partial\omega}{\partial m}$ may be expressed as

$$(\frac{\partial\omega}{\partial l}, \frac{\partial\omega}{\partial m}) = \left(\frac{(N^2-\omega^2)l + f_y(\vec{\kappa}\cdot\vec{f})}{\omega\kappa^2}, \frac{-\omega^2 m + f_z(\vec{\kappa}\cdot\vec{f})}{\omega\kappa^2}\right). \tag{4.19}$$

So far we have been able to determine the phase and group velocities of internal gravity waves including the full effect of rotation. In what follows we will assume all beams lie in the same vertical plane and hence the problem is two-dimensional. Thus we assume uniformity in the y directions so that the focus is now on the x and z directions. The group velocity then reduces to

$$\vec{v}_g = \frac{1}{\omega\kappa^2}\Big([(N^2-\omega^2)k + f_x(\vec{\kappa}\cdot\vec{f})], [-\omega^2 m + f_z(\vec{\kappa}\cdot\vec{f})]\Big)(\mathbf{e}_x, \mathbf{e}_z). \tag{4.20}$$

For uniformity of rotation constants we let $f_x = f_h$ and $f_z = f$.

Define $\hbar$ such that

$$\hbar = -\frac{k}{m}, \tag{4.21}$$

where $\hbar$ is the beam slope. Using the dispersion relation (2.181) and dividing through by m^2 gives a quadratic equation in $\hbar$,

$$(N^2 - \omega^2 + f_h^2)\hbar^2 - 2ff_h\hbar + (f^2 - \omega^2) = 0. \tag{4.22}$$

The discriminant Δ after division by 4 is given by

$$\Delta \equiv f^2f_h^2 + (N^2 + f_h^2 - \omega^2)(\omega^2 - f^2) = (N^2-\omega^2)(\omega^2-f^2) + f_h^2\omega^2 \geq 0. \tag{4.23}$$

As was derived in section (2.3.7), we have the following interval

$$\omega_{\text{min}}^2 \leq \omega^2 \leq \omega_{\text{max}}^2, \tag{4.24}$$

where ω_{min} and ω_{max} is given by (2.145) representing the minimum and maximum possible internal wave frequencies for the non-traditional approximation.

4.3.1 Collision Configuration

To study generation of second harmonics from colliding beams, we will be interested in two configurations namely: beams with vertical group velocity of the same sign (Figure (4.17)) and beams with horizontal group velocity of the same sign (Figure (4.18)). In figure (4.17) the colliding beams are forced in quadrants **I** and **II** whereas in figure (4.18) the beams are forced in quadrants **I** and **IV**. In sections (4.3.3) and (4.3.4) we will see that not every collision configuration results in the generation of second harmonic beams. Each of the two interacting beams represent one of two characteristics (ξ or η) defined by equation (2.131). The rule determining the generation of second harmonic beams from colliding wave beams may be determined using,

$$\begin{cases} \frac{k^H}{m^H} = \frac{k_1+k_2}{m_1+m_2} \quad \text{for} \quad \omega_1+\omega_2 \text{ frequency waves,} \\ \\ \frac{k^H}{m^H} = \frac{k_2-k_1}{m_2-m_1} \quad \text{for} \quad \omega_2-\omega_1 \text{ frequency waves} \end{cases} \tag{4.25}$$

where k_n and m_n $(n = 1, 2)$, represent the horizontal and vertical wave numbers of each of the colliding beams and $\omega_2 > \omega_1$. To justify equation (4.25), notice that given two plane waves the nonlinear terms contain terms of the form $\cos(k_1x + m_1z - \omega_1t) \times \cos(k_2x + m_2z - \omega_2t)$ which, using double angle formulas, gives cosine or sine terms with phase $(k_1+k_2)x+(m_1+m_2)z-(\omega_1+\omega_2)t$ and $(k_1-k_2)x+(m_1-m_2)z-(\omega_1-\omega_2)t$. So $\omega_1+\omega_2$ goes with k_1+k_2 and m_1+m_2 while $\omega_1-\omega_2$ goes with k_1-k_2 and m_1-m_2.

A beam from quadrant **I** is an $\hbar^+$ beam while that from other quadrant is an $\hbar^-$ beam. $\hbar_1^\pm$ are the slopes of the ω_1 wave beam while $\hbar_2^\pm$ are the slopes of the ω_2 wave beam. We also encounter $\hbar_{1,2}^\pm$ at some point in the thesis, it mean that a given expression or equation (where it is used) is true for both $\hbar_1^\pm$ and $\hbar_2^\pm$ wave beams. When we consider beams with the same wave frequency then the subscripts are dropped. The harmonics are defined using $\hbar^{H,\pm}$.

Parameter settings for figures (4.17)–(4.18) is defined in table (4.2), $\omega_1 = \omega_2 = 1.1 \times 10^{-4}\,\mathrm{rad\,s^{-1}}$.

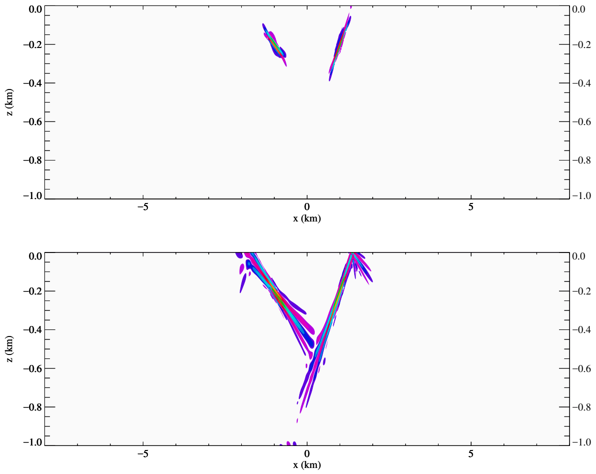

Figure 4.17: Numerical simulation showing the forcing of two beams with vertical group velocity of the same sign. As the beams propagate they collide at some time t as we see from the second panel. In the first panel t=15:00:00, second panel t=25:00:00.

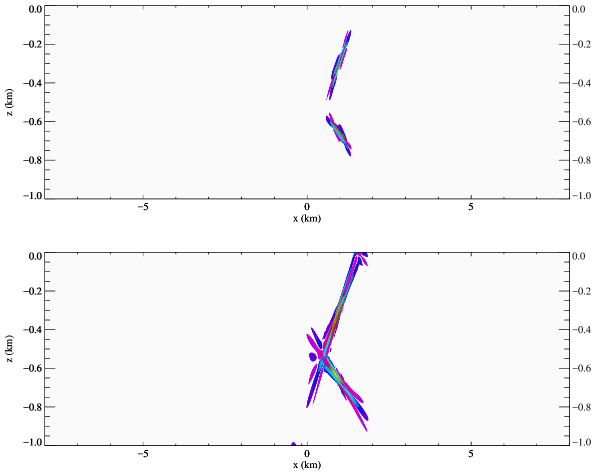

Figure 4.18: Numerical simulation showing the forcing of two beams with same sign horizontal group velocity. As the beams propagate they collide at some time t as the second panel show, In the first panel t=15:00:00, second panel t=41:40:00.

4.3.2 Formation Rules for Higher Harmonics

In line with the work done by Chung-Hsiang Jiang, this section derives the formation rule for the generation of higher harmonics from colliding wave beams. We will be concerned with internal waves with frequency defined in the interval

$$\omega_{\text{min}}^2 < f^2 < N^2 + f_h^2 < \omega_{\text{max}}^2. \tag{4.26}$$

Solving the quadratic equation (4.22) gives two real roots for $\hbar$ namely

$$\hbar^{\pm} = \frac{f f_h \pm \sqrt{\Delta}}{N^2 + f_h^2 - \omega^2} = \tan\theta^{\pm} = -\frac{k}{m}, \tag{4.27}$$

where $\hbar^{\pm}$ represent beams propagating at angles $\theta^{\pm}$ to the positive x-axis. From equation (4.27) the following relation may be established between the discriminant Δ and $f^2 f_h^2$;

- $\Delta > f^2 f_h^2$ and $\hbar^+\hbar^- < 0,$ if $f^2 < \omega^2 < N^2 + f_h^2,$
- $\Delta = f^2 f_h^2$ and $\hbar^+\hbar^- = 0,$ if $\omega^2 = f^2,$
- $\Delta < f^2 f_h^2$ and $\hbar^+\hbar^- > 0,$ if $\omega_{\text{min}}^2 < \omega^2 < f^2,$
- $\Delta < f^2 f_h^2$ and $\hbar^+\hbar^- > 0,$ if $\omega_{\text{max}}^2 > \omega^2 > N^2 + f_h^2,$

These gives four bounded ranges of possible internal wave frequencies for internal wave propagation namely, $f^2 < \omega^2 < N^2 + f_h^2,$ $\omega_{\text{max}}^2 > \omega^2 > N^2 + f_h^2,$ $\omega_{\text{min}}^2 < \omega^2 < f^2,$ and $\omega^2 = f^2$, in this thesis we will be concerned with the first two intervals.

From (4.18) and using the expression for $N^2 - \omega^2 + f_h^2$ from equation (4.27) we can express $\dfrac{\partial \omega}{\partial k}$ as

$$v_{g_x} = \omega k (\omega^2 \kappa^2)^{-1} (\pm\sqrt{\Delta}) (\hbar^{\pm})^{-1}. \tag{4.28}$$

Similarly $\frac{\partial \omega}{\partial m}$ may be expressed as

$$v_{g_z} = -\omega m (\omega^2 \kappa^2)^{-1} (\pm\sqrt{\Delta}) (\hbar^{\pm}). \tag{4.29}$$

Notice that dividing equation (4.28) by (4.29) gives $-(\hbar^{\pm})^{-1} = -\cot\theta^{\pm}$. The sign convention for $\hbar^{\pm}$ is obtained from equation (4.27). The group velocity vector $\vec{v}_g$ and the wave vector $\vec{\kappa}$ for internal gravity waves are related by the following sign rule

$$\text{sgn}\{v_{g_x}\} = \text{sgn}\{\omega k\}, \text{ and } \text{sgn}\{v_{g_z}\} = -\text{sgn}\{\omega m\}. \tag{4.30}$$

	$f^2 < \omega_1^2 <$ and $= \omega_2^2 < N^2 + f_h^2$	$\omega_{\max}^2 > \omega_1^2 >$ and $= \omega_2^2 > N^2 + f_h^2$
$\hbar^+$	> 0	< 0
$\hbar^-$	< 0	< 0
$\mathrm{sgn}\{v_{g_x}^+\}$	+ $\mathrm{sgn}\{\omega k^+\}$	- $\mathrm{sgn}\{\omega k^+\}$
$\mathrm{sgn}\{v_{g_z}^+\}$	- $\mathrm{sgn}\{\omega m^+\}$	+ $\mathrm{sgn}\{\omega m^+\}$
$\mathrm{sgn}\{v_{g_x}^-\}$	+ $\mathrm{sgn}\{\omega k^-\}$	+ $\mathrm{sgn}\{\omega k^-\}$
$\mathrm{sgn}\{v_{g_z}^-\}$	- $\mathrm{sgn}\{\omega m^-\}$	- $\mathrm{sgn}\{\omega m^-\}$

Table 4.3: Shows the sign of $\hbar^\pm$ and how the phase velocity $\vec{v}_p$ relates to the group velocity $\vec{v}_g$ depending on the frequency intervals.

Equation (4.30) may be deduced from (4.28) and (4.29), although this relation depends on the frequency intervals for which the solvability condition is satisfied, see table (4.3) which was created using equations (4.27), (4.28) and (4.29).

Figure (4.19) illustrates four incoming beams, from four different quadrants. We name the beams first (I), second (II), third (III) and fourth (IV) accordingly.

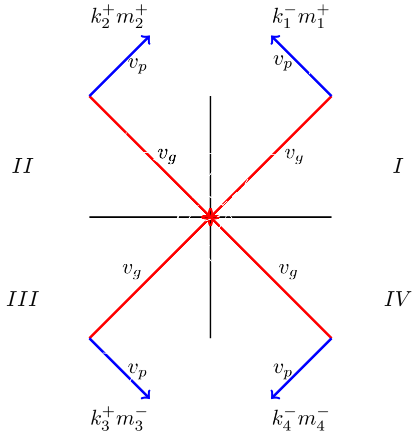

Figure 4.19: Schematic showing propagating incoming beams from all quadrants of a 2-D plane and the signs of their corresponding wave number vectors assuming $\omega > 0$.

If we consider beams from the first and second quadrant we observe the following relations

$$\begin{cases} \mathbf{I}: & \omega_1 k_1 < 0 \quad \omega_1 m_1 > 0 \\ \mathbf{II}: & \omega_2 k_2 > 0 \quad \omega_2 m_2 > 0 \end{cases}. \tag{4.31}$$

where $\omega > 0$. Since the generated harmonics comprise the sum and difference frequencies of the interacting beams it may be represented as follows,

$$\begin{cases} (|\omega_1 \pm \omega_2|)k^H & = (|\omega_1 \pm \omega_2|)(k_1 \pm k_2) \\ (|\omega_1 \pm \omega_2|)m^H & = (|\omega_1 \pm \omega_2|)(m_1 \pm m_2). \end{cases} \tag{4.32}$$

The wave vectors of the $\omega_1 + \omega_2$ second harmonics may be defined using equation (4.21) as follows

$$\frac{k^H}{m^H} = \frac{k_1 + k_2}{m_1 + m_2} = \frac{\hbar^+ m_1 + \hbar^- m_2}{m_1 + m_2} = \hbar^{H,\pm}. \tag{4.33}$$

From equation (4.33), we obtain

$$\hbar^{H,\pm}(m_1 + m_2) = \hbar^+ m_1 + \hbar^- m_2. \tag{4.34}$$

Further simplification gives

$$\frac{m_1}{m_2} = -\frac{\hbar^{H,\pm} - \hbar^-}{\hbar^{H,\pm} - \hbar^+}. \tag{4.35}$$

If we consider $\omega_2 - \omega_1$ harmonics then,

$$\frac{k^H}{m^H} = \frac{k_2 - k_1}{m_2 - m_1} = \frac{\hbar^+ m_2 - \hbar^- m_1}{m_2 - m_1} = \hbar^{H,\pm}, \tag{4.36}$$

after doing some algebra we find that

$$\frac{m_1}{m_2} = \frac{\hbar^{H,\pm} - \hbar^+}{\hbar^{H,\pm} - \hbar^-}. \tag{4.37}$$

Equations (4.35) and (4.37) are the conditions for the generation of higher harmonics corresponding to $\omega_1 + \omega_2$ and $\omega_2 - \omega_1$ frequencies respectively. The $\omega_1 + \omega_2$ rule requires that for second harmonics to be generated the signs on both sides of equation (4.35) must be the same. However, the $\omega_2 - \omega_1$ rule requires that the sign on both sides of equation

(4.37) must be the same with respect to the higher frequency wave ω_2 for the harmonics to be generated. (4.37) is only applicable when we consider interacting wave beams of different frequencies since $\omega_2 - \omega_1 = 0$ when $\omega_2 = \omega_1$. We will use the symbols (> 0) and (< 0) to represent the sign convention of subsequent expressions involving the formation rules, where (> 0) means positive and (< 0) implies negative.

To determine the magnitude of $\hbar^{H,\pm}$ in relation to $\hbar^{\pm}$ we specify an equivalence relation given by

$$\hbar^{H,\pm} \equiv \frac{f f_h \pm \sqrt{\Delta^H}}{N^2 + f_h^2 - (\omega_1 \pm \omega_2)^2} \tag{4.38}$$

where

$$\Delta^H = f^2 f_h^2 + [N^2 + f_h^2 - (\omega_1 \pm \omega_2)^2][(\omega_1 \pm \omega_2)^2 - f^2]. \tag{4.39}$$

Equation (4.38) represents the second harmonics generated from the collision of the $\hbar^+$ and $\hbar^-$ beams. Hence the group velocities and phase speed of the second harmonics can be determined from figures (4.2a) and (4.4) by specifying the frequencies of the beams. Note that except otherwise stated the values of the parameters f_h, f, m, θ, and ϕ are given in table (4.1). In the case of colliding beams the magnitude of the vertical wave numbers of the beams involved in the collision are the same, thus $m_1 = m_2 = m$ (except where otherwise stated). The goal of the simulations that follow is to show that in the specified intervals and according to the prediction of the formation rule that second harmonics are generated from the collision of two internal wave beams. All simulations presented here are in the context of the non-traditional approximation. The arrows indicate direction of propagation of the colliding wave beams.

4.3.3 Forcing Frequency Interval $f^2 < \omega_1^2 = \omega_2^2 < N^2 + f_h^2$

Here we consider internal gravity waves in the interval $f^2 < \omega_1^2 = \omega_2^2 < N^2 + f_h^2$, the outgoing second harmonic (if generated) should propagate if its frequency satisfies $f^2 < (2\omega)^2 < \omega_{\max}^2$. Based on the collision configuration, first consider the two colliding beams to have vertical group velocity of the same sign (for example beams propagating from quadrant **I** and **II** towards the origin) and secondly the colliding beams have horizontal group velocity of the same sign(beams propagating into quadrant **I** and **IV**). The arrows indicate the direction of propagation of the incident beams. In all cases of the numerical simulations presented here, the aim is to show the generation of second harmonics in the specified range of frequencies.

For $f^2 < (2\omega)^2 < N^2 + f_h^2$, the following relation holds

$$\hbar^{H,+} > \hbar^{+} > 0 > \hbar^{-} > \hbar^{H,-}. \tag{4.40}$$

Considering the first configuration where the colliding beams propagate from quadrant **I** and **II** towards the origin, from (4.31), (4.35)and (4.40) we find that

$$\underbrace{\frac{m_1}{m_2}}_{(>0)} = -\frac{\overbrace{\hbar^{H,+} - \hbar^{-}}^{(>0)}}{\underbrace{\hbar^{H,+} - \hbar^{+}}_{(>0)}} \quad (<0) \qquad \text{and} \qquad \underbrace{\frac{m_1}{m_2}}_{(>0)} = -\frac{\overbrace{\hbar^{H,-} - \hbar^{-}}^{(<0)}}{\underbrace{\hbar^{H,-} - \hbar^{+}}_{(<0)}} \quad (<0). \tag{4.41}$$

Note that the (>0) and (<0) symbols represents the sign the associated expressions resolves to. So for example (>0) on the R.H.S of equation (4.41) means that the R.H.S simplifies to a negative value. Now since the sign on both sides of equation (4.41) do not agree no second harmonic is generated. See figure (4.20).

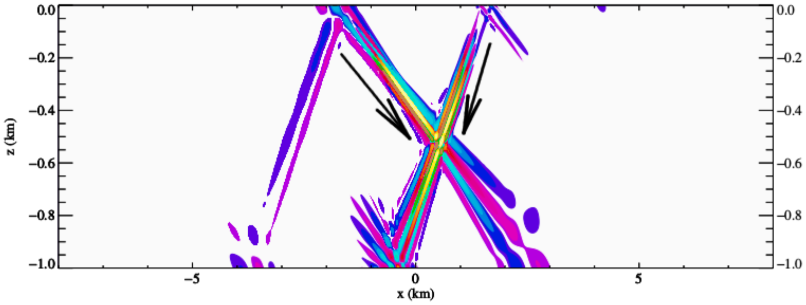

Figure 4.20: Numerical simulation of two wave beams propagating from angles 64° and 102.7° respectively with the positive x-axis at time t=135:20:00. Parameter settings are $\omega_1 = \omega_2 = 1.4 \times 10^{-4}\mathrm{rad\,s^{-1}}$, $N = 3.0 \times 10^{-4}\mathrm{rad\,s^{-1}}$.

Consider beams propagating from quadrant **I** and quadrant **IV** towards the origin.

$$\begin{cases} \mathbf{I}: & \omega k_1 < 0 \quad \omega m_1 > 0 \\ \mathbf{IV}: & \omega k_2 < 0 \quad \omega m_2 < 0 \end{cases}, \tag{4.42}$$

from (4.42) we observe that,

$$\begin{cases} (2\omega)k^H & = 2\omega(k_1 + k_2) < 0 \\ (2\omega)m^H & = 2\omega(m_1 + m_2) \end{cases}. \tag{4.43}$$

Applying the sign convention to equation (4.43) gives

$$\underbrace{\frac{m_1}{m_2}}_{(<0)} = -\frac{\overbrace{\hbar^{H,+} - \hbar^-}^{(>0)}}{\underbrace{\hbar^{H,+} - \hbar^+}_{(>0)}} \quad (<0), \qquad \text{and} \qquad \underbrace{\frac{m_1}{m_2}}_{(<0)} = -\frac{\overbrace{\hbar^{H,-} - \hbar^-}^{(<0)}}{\underbrace{\hbar^{H,-} - \hbar^+}_{(<0)}} \quad (>0). \tag{4.44}$$

Second harmonics corresponding to $\hbar^{H,\pm}$ are allowed to propagate since the sign convention is satisfied. $\hbar^{H,-}$ represents beam propagating into quadrant **II**, while $\hbar^{H,+}$ represents beam propagating into quadrant **III**. See figure (4.21), showing two beams of the same frequency propagating with different group velocities, beam $\hbar^+$ propagates with group velocity $2.95 \times 10^{-3}\mathrm{m\,s^{-1}}$ while beam $\hbar^-$ propagates with group velocity $3.2 \times 10^{-3}\mathrm{m\,s^{-1}}$. The $\hbar^{H,+}$ (quadrant **III**) beam propagates with group velocity $9.17 \times 10^{-4}\mathrm{m\,s^{-1}}$, while the $\hbar^{H,-}$ (quadrant **II**) beam propagates with group velocity $1.37 \times 10^{-3}\mathrm{m\,s^{-1}}$.

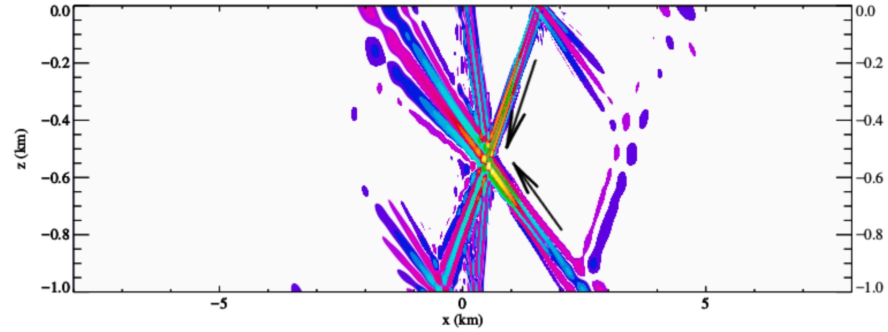

Figure 4.21: Collision of two wave beams propagating from quadrant **I** and quadrant **IV** and makes angles 64° and 283° respectively with respect to the positive x-axis at time t=135:20:00. Parameter values are $\omega_1 = \omega_2 = 1.4 \times 10^{-4}\text{rad}\,\text{s}^{-1}$, $N = 3.0 \times 10^{-4}\text{rad}\,\text{s}^{-1}$. Two second harmonic beams propagating into quadrant **II** and **III** are generated.

Suppose the second harmonic frequency falls in the interval $\omega_{\max}^2 > (2\omega)^2 > N^2 + f_h^2$, then the order of magnitude relation becomes

$$\hbar^+ > 0 > \hbar^- > \hbar^{H,-} > \hbar^{H,+}. \tag{4.45}$$

For wave beams propagating from quadrant **I** and **II** towards the origin the relation gives,

$$\underbrace{\frac{m_1}{m_2}}_{(>0)} = -\frac{\overbrace{\hbar^{H,+} - \hbar^-}^{(<0)}}{\underbrace{\hbar^{H,+} - \hbar^+}_{(<0)}} \quad (< 0) \quad \text{and} \quad \underbrace{\frac{m_1}{m_2}}_{(>0)} = -\frac{\overbrace{\hbar^{H,-} - \hbar^-}^{(<0)}}{\underbrace{\hbar^{H,-} - \hbar^+}_{(<0)}} \quad (< 0). \tag{4.46}$$

The sign convention is not satisfied thus second harmonic beams are prohibited for this collision configuration see figure (4.22).

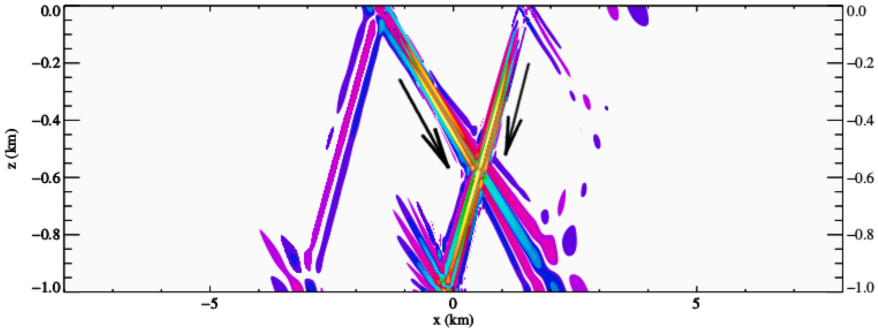

Figure 4.22: Numerical simulation of propagating wave beams. The frame shown was taken at at time t=135:20:00. Parameter values are $\omega_1 = \omega_2 = 1.45 \times 10^{-4}\mathrm{rad\,s^{-1}}$, $N = 2.7 \times 10^{-4}\mathrm{rad\,s^{-1}}$.

Secondly for beams propagating from quadrant **I** and **IV** we find that the ratio of the vertical wavenumbers m_1 and m_2 always have a negative sign convention thus the sign rule is satisfied,

$$\underbrace{\frac{m_1}{m_2}}_{(<0)} = -\frac{\overbrace{\hbar^{H,+} - \hbar^{-}}^{(<0)}}{\underbrace{\hbar^{H,+} - \hbar^{+}}_{(<0)}} \quad (<0) \quad \text{and} \quad \underbrace{\frac{m_1}{m_2}}_{(<0)} = -\frac{\overbrace{\hbar^{H,-} - \hbar^{-}}^{(<0)}}{\underbrace{\hbar^{H,-} - \hbar^{+}}_{(<0)}} \quad (<0). \tag{4.47}$$

Hence second harmonics are generated from this collision. See figure (4.23) for which beam from quadrant **I** propagates with group velocity $2.58 \times 10^{-3}\mathrm{m\,s^{-1}}$ while beam from quadrant **IV** propagates with group velocity $2.92 \times 10^{-3}\mathrm{m\,s^{-1}}$. The second harmonics (corresponding to the $\hbar^{H,+}$ and $\hbar^{H,-}$ beams) generated from this collision are in the interval $\omega_{\max}^2 > (2\omega)^2 > N^2 + f_h^2$. The $\hbar^{H,+}$ (quadrant **III**) beam propagates with group velocity $1.266 \times 10^{-5}\mathrm{m\,s^{-1}}$, while the $\hbar^{H,-}$ (quadrant **II**) beam propagates with group velocity $1.23 \times 10^{-4}\mathrm{m\,s^{-1}}$.

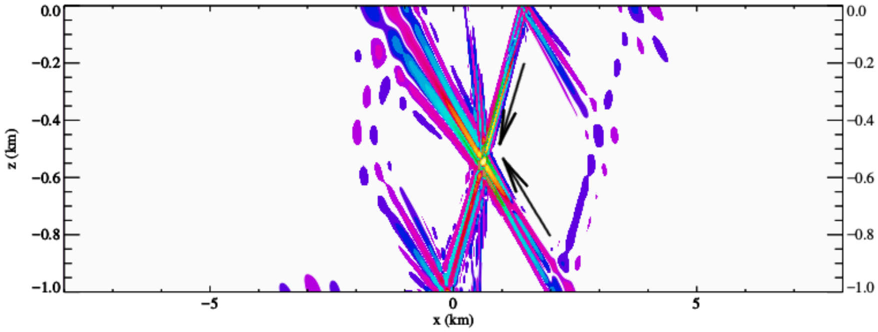

Figure 4.23: Numerical simulation of colliding beams propagating from quadrant **I** and quadrant **II**. Frame corresponds to time t=145:30:00. Parameter values are $\omega_1 = \omega_2 = 1.45 \times 10^{-4}\text{rad}\,\text{s}^{-1}$, $N = 2.7 \times 10^{-4}\text{rad}\,\text{s}^{-1}$.

4.3.4 Forcing Frequency Interval $f^2 < \omega_1^2 < \omega_2^2 < N^2 + f_h^2$

Here we consider beams of different forcing frequency. The frequency interval for this case is $f^2 < \omega_1^2 < \omega_2^2 < N^2 + f_h^2$. Any second harmonic beam generated from nonlinear interactions of the incident beams will have frequency ω in the range $f^2 < (\omega_1 + \omega_2)^2 < N^2 + f_h^2$, $f^2 < (\omega_2 - \omega_1)^2 < N^2 + f_h^2$, or $\omega_{\max}^2 > (\omega_1 + \omega_2)^2 > N^2 + f_h^2$. Since the beams are of different forcing frequencies we re-define the equivalence relation given in equation (4.38) as follows

$$\hbar_+^{H,\pm} \equiv \frac{f f_h \pm \sqrt{\Delta_+^H}}{N^2 + f_h^2 - (\omega_1 + \omega_2)^2} \text{ and } \hbar_-^{H,\pm} \equiv \frac{f f_h \pm \sqrt{\Delta_-^H}}{N^2 + f_h^2 - (\omega_2 - \omega_1)^2}, \tag{4.48}$$

where

$$\Delta_+^H \equiv f^2 f_h^2 + [N^2 + f_h^2 - (\omega_1 + \omega_2)^2][(\omega_1 + \omega_2)^2 - f^2]. \tag{4.49}$$

$$\Delta_-^H \equiv f^2 f_h^2 + [N^2 + f_h^2 - (\omega_1 - \omega_2)^2][(\omega_2 - \omega_1)^2 - f^2]. \tag{4.50}$$

Consider beams propagating from quadrant **I** and **II** towards the origin

$$\begin{cases} \textbf{I}: & \omega_1 k_1 < 0 \quad \omega_1 m_1 > 0 \\ \textbf{II}: & \omega_2 k_2 > 0 \quad \omega_2 m_2 > 0 \end{cases}. \tag{4.51}$$

The second harmonic beams have the form

$$\begin{cases} (|\omega_2 \pm \omega_1|)k^H & = (|\omega_2 \pm \omega_1|)(k_1 \pm k_2) \\ (|\omega_2 \pm \omega_1|)m^H & = (|\omega_2 \pm \omega_1|)(m_1 \pm m_2) \end{cases} . \tag{4.52}$$

As in previous cases no second harmonic is generated from this collision configuration since the formation rule is not satisfied. To see this consider the radiation condition $f^2 < (\omega_1 + \omega_2)^2 < N^2 + f_h^2$ then the following order of magnitude relation hold

$$\hbar_+^{H,+} > \hbar_2^+ > \hbar_1^+ > 0 > \hbar_1^- > \hbar_2^- > \hbar_+^{H,-}. \tag{4.53}$$

Applying this to the formation rule (4.35) gives

$$\underbrace{\frac{m_1}{m_2}}_{(>0)} = -\frac{\overbrace{\hbar_+^{H,+} - \hbar_{1,2}^-}^{(>0)}}{\underbrace{\hbar_+^{H,+} - \hbar_{1,2}^+}_{(>0)}} \quad (< 0) \quad \text{and} \quad \underbrace{\frac{m_1}{m_2}}_{(>0)} = -\frac{\overbrace{\hbar_+^{H,-} - \hbar_{1,2}^-}^{(<0)}}{\underbrace{\hbar_+^{H,-} - \hbar_{1,2}^+}_{(<0)}} \quad (< 0) \tag{4.54}$$

The sign convention is not satisfied thus no second harmonic is generated.

In the same vein, consider $\omega_2 - \omega_1$ frequency beam such that

$$\omega_1^2 \leq (\omega_2 - \omega_1)^2 < \omega_2^2. \tag{4.55}$$

Using the allowed frequency interval

$$f^2 < (\omega_2 - \omega_1)^2 < N^2 + f_h^2. \tag{4.56}$$

The following order of magnitude relation holds

$$\hbar_2^+ > \hbar_-^{H,+} > \hbar_1^+ > 0 > \hbar_1^- > \hbar_-^{H,-} > \hbar_2^-. \tag{4.57}$$

Applying equation (4.57) to (4.37) for the lower frequency wave (ω_1) we find that

$$\underbrace{\frac{m_1}{m_2}}_{(>0)} = \frac{\overbrace{\hbar_-^{H,+} - \hbar_1^+}^{(>0)}}{\underbrace{\hbar_-^{H,+} - \hbar_1^-}_{(>0)}} \quad (> 0) \text{ and } \underbrace{\frac{m_1}{m_2}}_{(>0)} = \frac{\overbrace{\hbar_-^{H,-} - \hbar_1^+}^{(<0)}}{\underbrace{\hbar_-^{H,-} - \hbar_1^-}_{(<0)}} \quad (> 0), \tag{4.58}$$

and for the higher frequency wave (ω_2) we get that

$$\underbrace{\frac{m_1}{m_2}}_{(>0)} = \frac{\overbrace{\hbar_-^{H,+} - \hbar_2^+}^{(<0)}}{\underbrace{\hbar_-^{H,+} - \hbar_2^-}_{(>0)}} \quad (< 0) \text{ and } \underbrace{\frac{m_1}{m_2}}_{(>0)} = \frac{\overbrace{\hbar_-^{H,-} - \hbar_2^+}^{(<0)}}{\underbrace{\hbar_-^{H,-} - \hbar_2^-}_{(>0)}} \quad (< 0). \tag{4.59}$$

Since the sign convention is not satisfied with respect to the higher frequency wave ω_2 no harmonics are generated for this collision configuration. See figure (4.24).

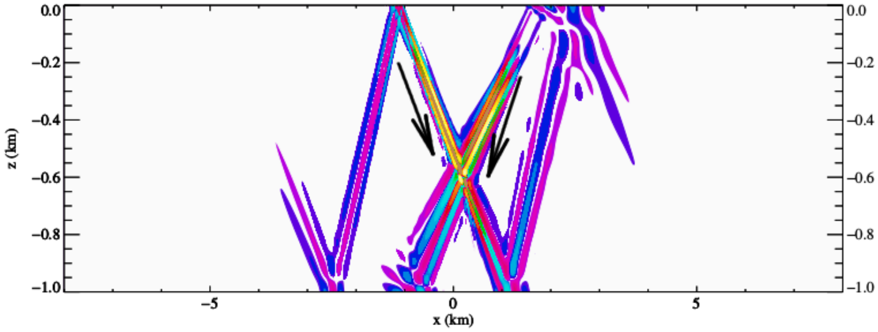

Figure 4.24: Numerical simulation of the collision of internal wave beams propagating at angles 70° and 161° that is from quadrant **I** and quadrant **II** respectively, the frame shown here was taken at time t = 145:50:00. Parameter values are $\omega_1 = 1.2 \times 10^{-4}\text{rad}\,\text{s}^{-1}$ propagating from quadrant **I**, $\omega_2 = 1.8 \times 10^{-4}\text{rad}\,\text{s}^{-1}$ propagating from quadrant **II**, $N = 3.0 \times 10^{-4}\text{rad}\,\text{s}^{-1}$.

For beams propagating from quadrant **I** and **IV**, the ratio of the vertical wave numbers m_1 and m_2 now has a negative sign since the two wavenumbers are directed opposite to each other. Now applying the formation rule (4.35) to the ($\omega_1 + \omega_2$) frequency wave we find that the sign convention is satisfied and thus second harmonics are allowed to propagate. See figures (4.25), (4.26).

Also applying the formation rule (4.37) to $\omega_2 - \omega_1$ waves we observe that the sign convention is now satifified (with respect to the ω_2 frequency waves) and the harmonics represented by $\omega_2 - \omega_1$ are allowed to propagate. This can be observed in figure (4.27) where harmonics corresponding to the frequency difference $\omega_2 - \omega_1$ are generated. The frequency belongs in the interval $f^2 < (\omega_2 - \omega_1)^2 < N^2 + f_h^2$.

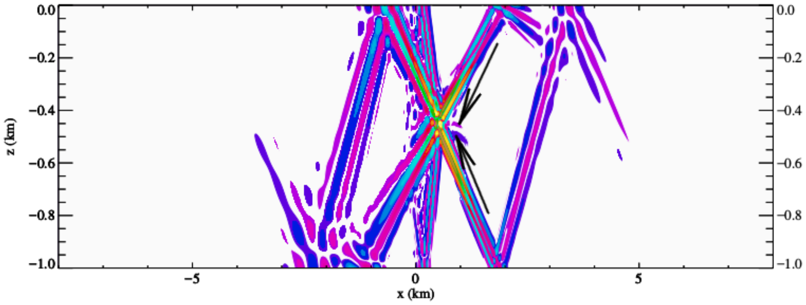

Figure 4.25: Numerical simulation of colliding beams propagating from quadrant **I** and quadrant **IV**. Frame at t=145:50:00. Parameter values are $\omega_1 = 1.2 \times 10^{-4}\mathrm{rad\,s^{-1}}$, propagating with group velocity $2.84 \times 10^{-3}\mathrm{m\,s^{-1}}$, $\omega_2 = 1.8 \times 10^{-4}\mathrm{rad\,s^{-1}}$, propagating with group velocity $3.69 \times 10^{-3}\mathrm{m\,s^{-1}}$, $N = 3.3 \times 10^{-4}\mathrm{rad\,s^{-1}}$. The $\hbar^{H,+}$ (quadrant **III**) beam propagates with group velocity $1.16 \times 10^{-3}\mathrm{m\,s^{-1}}$, while the $\hbar^{H,-}$ (quadrant **II**) beam propagates with group velocity $1.6 \times 10^{-3}\mathrm{m\,s^{-1}}$.

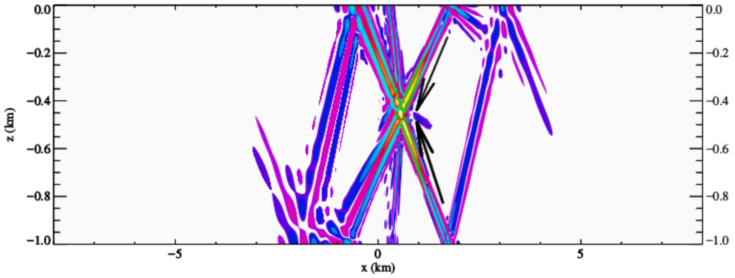

Figure 4.26: Same settings as in (4.25) but with a reduced buoyancy frequency. Time of frame t=145:50:00, $\omega_1 = 1.2 \times 10^{-4}\mathrm{rad\,s^{-1}}$ propagating from quadrant **I** with group velocity $2.6 \times 10^{-3}\mathrm{m\,s^{-1}}$, $\omega_2 = 1.8 \times 10^{-4}\mathrm{rad\,s^{-1}}$ propagating from quadrant **IV** with group velocity $3.24 \times 10^{-3}\mathrm{m\,s^{-1}}$, $N = 3.0 \times 10^{-4}\mathrm{rad\,s^{-1}}$. The $\hbar^{H,+}$ (quadrant **III**) beam propagates with group velocity $4.08 \times 10^{-4}\mathrm{m\,s^{-1}}$, while the $\hbar^{H,-}$ (quadrant **II**) beam propagates with group velocity $7.66 \times 10^{-3}\mathrm{m\,s^{-1}}$.

In figure (4.27) we show results from a case for which the forcing frequency of one of the beams is twice the other. $N = 3.65 \times 10^{-4}\mathrm{rad\,s^{-1}}$, $\omega_1 = 1.2 \times 10^{-4}\mathrm{rad\,s^{-1}}$, propagating from quadrant **I** with group velocity $3.12 \times 10^{-3}\mathrm{m\,s^{-1}}$, $\omega_2 = 2.4 \times 10^{-4}\mathrm{rad\,s^{-1}}$ propagating from quadrant **IV** with group velocity $3.63 \times 10^{-3}\mathrm{m\,s^{-1}}$. We observe the generation of second harmonics of $\omega_1+\omega_2$ frequency (i.e the second harmonic propagating into quadrant **II** and **III** and $\omega_2-\omega_1$ frequency waves (propagating into quadrants **II** and **IV**. The $\hbar^{H,+}$ (quadrant **III**) beam propagates with group velocity $4.89\times10^{-4}\mathrm{m\,s^{-1}}$, while the $\hbar^{H,-}$ (quadrant **II**) beam propagates with group velocity $7.706\times10^{-3}\mathrm{m\,s^{-1}}$.

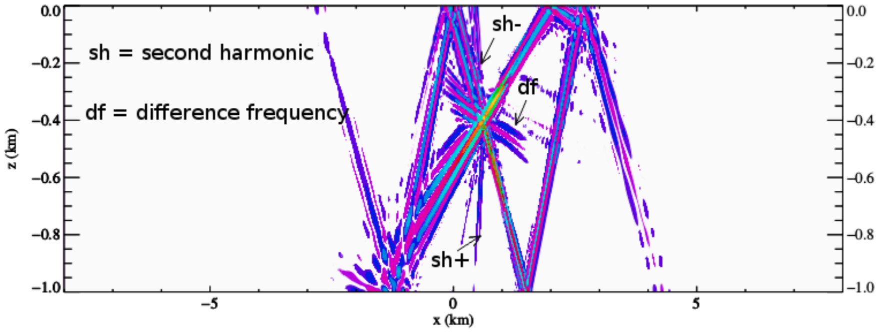

Figure 4.27: Frame taken at time t=150:00:00. The $\omega_1+\omega_2$ frequency component propagates at $7.71\times10^{-4}\mathrm{m\,s^{-1}}$ group velocity while the $\omega_2-\omega_1$ frequency waves propagates with group velocity $3.22\times10^{-3}\mathrm{m\,s^{-1}}$. For this numerical simulation $m_1=\frac{2\pi}{30}\mathrm{m}^{-1}$, $m_2=\frac{2\pi}{50}\mathrm{m}^{-1}$, $a=10\mathrm{m}$, $b=200\mathrm{m}$.

Secondly we investigate the case where the frequency of the second harmonic falls in the interval

$$\omega_{\max}^2>(\omega_1+\omega_2)^2>N^2+f_h^2. \tag{4.60}$$

The order of magnitude relation for this radiation condition is given by

$$\hbar_2^+>\hbar_1^+>0>\hbar_1^->\hbar_2^->\hbar^{H,-}>\hbar^{H,+}. \tag{4.61}$$

For beams propagating from quadrant **I** and **II** towards the origin the following relation holds

$$\underbrace{\frac{m_1}{m_2}}_{(>0)}=-\frac{\overbrace{\hbar^{H,+}-\hbar_{1,2}^-}^{(<0)}}{\underbrace{\hbar^{H,+}-\hbar_{1,2}^+}_{(<0)}}\quad(<0)\qquad\text{and}\qquad\underbrace{\frac{m_1}{m_2}}_{(>0)}=-\frac{\overbrace{\hbar^{H,-}-\hbar_{1,2}^-}^{(<0)}}{\underbrace{\hbar^{H,-}-\hbar_{1,2}^+}_{(<0)}}\quad(<0). \tag{4.62}$$

No second harmonic is permitted since the sign convention defined by equation (4.35) is violated, see figure (4.28).

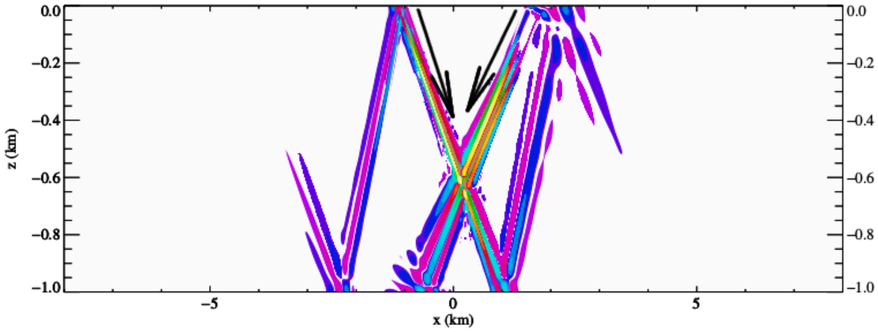

Figure 4.28: $N = 2.8 \times 10^{-4}\mathrm{rad\,s^{-1}}$, $\omega_1 = 1.2 \times 10^{-4}\mathrm{rad\,s^{-1}}$ propagating from quadrant **I**, $\omega_2 = 1.8 \times 10^{-4}\mathrm{rad\,s^{-1}}$ propagating from quadrant **II**.

Consider beams propagating from quadrant **I** and **IV** then the sign convention is satisfied, higher harmonics corresponding to $\hbar^{H,+}$ and $\hbar^{H,-}$ are permitted to propagate.

$$\underbrace{\frac{m_1}{m_2}}_{(<0)} = -\frac{\overbrace{\hbar^{H,+} - \hbar^{-}_{1,2}}^{(>0)}}{\underbrace{\hbar^{H,+} - \hbar^{+}_{1,2}}_{(>0)}} \quad (<0) \qquad \text{and} \qquad \underbrace{\frac{m_1}{m_2}}_{(<0)} = -\frac{\overbrace{\hbar^{H,-} - \hbar^{-}_{1,2}}^{(<0)}}{\underbrace{\hbar^{H,-} - \hbar^{+}_{1,2}}_{(<0)}} \quad (<0) \tag{4.63}$$

See figure (4.29) showing the generation of two beams, the upward propagating second harmonic beam $\hbar^{H,-}$ with group velocities $v^{H,-}_{g_x} < 0$ and $v^{H,-}_{g_z} > 0$ and the downward propagating second harmonic beam $\hbar^{H,+}$, with group velocity $v^{H,-}_{g_x} > 0$, and $v^{H,-}_{g_z} < 0$. The $\hbar^{H,+}$ (quadrant **III**) beam propagates with group velocity $1.82 \times 10^{-4}\mathrm{m\,s^{-1}}$, while the $\hbar^{H,-}$ (quadrant **II**) beam propagates with group velocity $7.25 \times 10^{-5}\mathrm{m\,s^{-1}}$

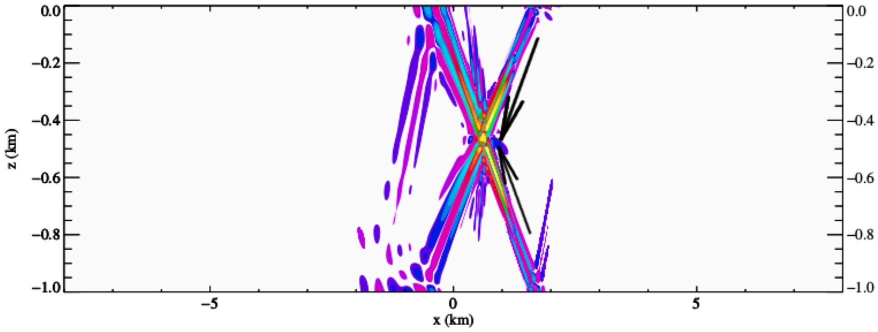

Figure 4.29: Simulation showing collision of two wave beams. Parameter values are $\omega_1 = 1.2 \times 10^{-4}\mathrm{rad\,s^{-1}}$ beam propagating with group velocity $2.43 \times 10^{-3}\mathrm{m\,s^{-1}}$, $\omega_2 = 1.8 \times 10^{-4}\mathrm{rad\,s^{-1}}$ wave beam propagating with group velocity $2.95 \times 10^{-3}\mathrm{m\,s^{-1}}$, $N = 2.8 \times 10^{-4}\mathrm{rad\,s^{-1}}$. The generated harmonics are propagating with group velocity $7.25 \times 10^{-5}\mathrm{m\,s^{-1}}$. Time of frame t=133:20:00

Notice that in the interval specified by equation (4.60) the $\omega_2 - \omega_1$ frequency beam is not valid since $(\omega_2 - \omega_1)^2 < N^2 + f_h^2$, which takes us back to the case already treated.

4.4 Internal Wave Reflection as a Time Series

In this section we report some results from spectral analysis of time series obtained from moorings fixed at several locations in the flow field of an internal wave beam reflecting off a flat bottom (figure (4.30)). We are interested in determining the dominant frequency from the time series at different locations. The time series are obtained in the time domain, using the fast Fourier transform we transform the data into the frequency domain which provides information about the relative magnitude of the power in each frequency that make up the signal. We use the matlab Welch algorithm to estimate the power spectral density. The unit of the power spectral density adopted in this thesis is the decibel which uses a log scale for easier comparison of the various frequencies in the time series.

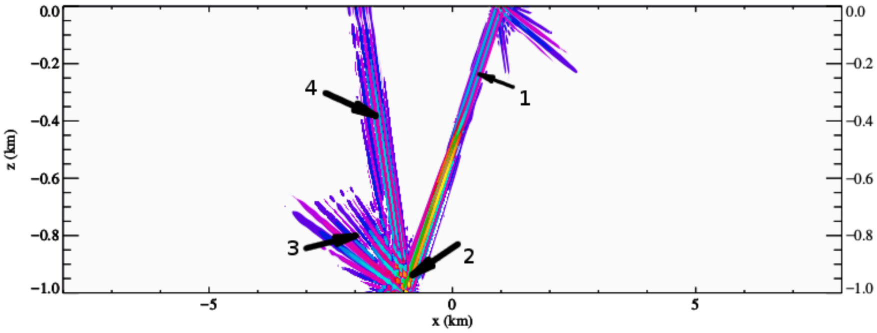

Figure 4.30: Numerical simulation showing the horizontal velocity profile of an internal wave beam reflecting off a flat bottom $\beta = 0$. The arrows point to mooring locations from which time series data were obtained. Parameter settings are for this simulation are defined in table (4.1) the frequency of the incident wave beam is $\omega = 1.2 \times 10^{-4}\,\mathrm{rad\,s^{-1}}$.

Figures (4.31), (4.32), (4.33), and (4.34) show the time series data in the time domain, frequency decomposition and power spectrum of the time series obtained from mooring locations marked by arrows on figure (4.30). Mooring **1** is located on the upward propagating first harmonic. Nonlinear interactions occur at the region marked **2**, the incident and reflected first harmonic waves interact at this region causing the generation of second harmonic wave beam. Mooring **3** is in the first harmonic reflected beam while mooring **4** obtains time series from the second harmonic beam.

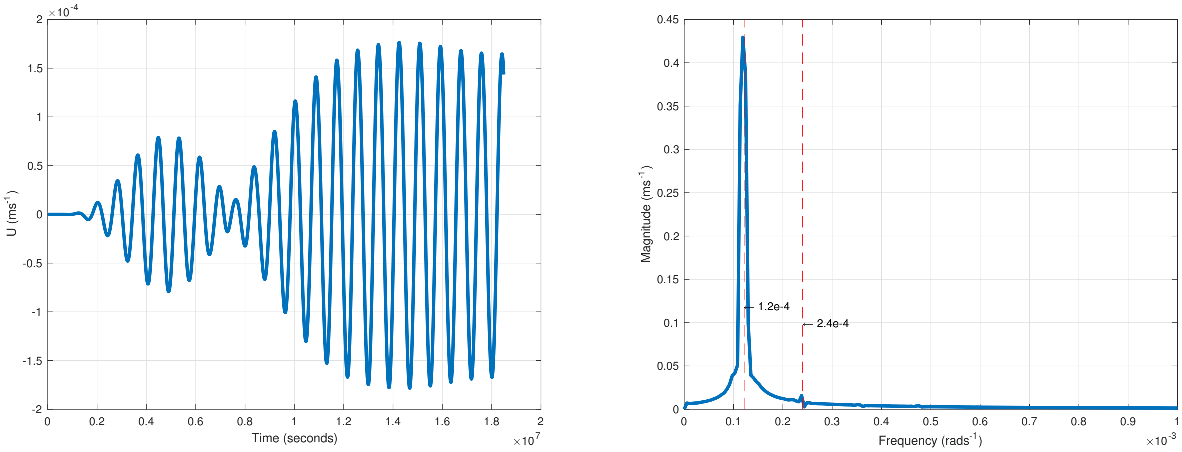

(a) Observed signal at mooring-1.

(b) Frequency response at mooring-1

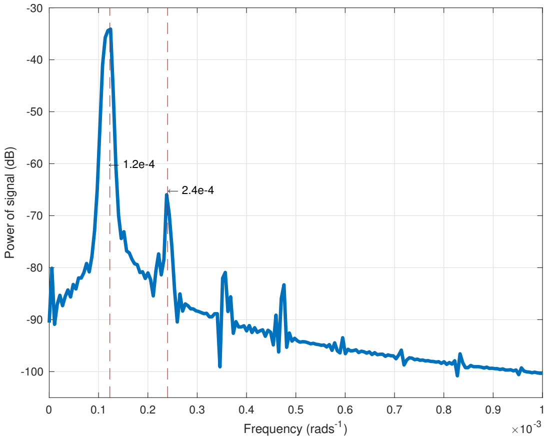

(c) PSD at mooring-1

Figure 4.31: (4.31a) illustrates the signal in the time domain. (4.31b) represents the frequency response, from the frequency response it can be observed that the dominant frequency is the first harmomnic frequency. In figure (4.31c) the power spectral density shows that the strength of the signal is strongest at the first harmonic frequency $\omega = 1.2 \times 10^{-4} \mathrm{rad\,s}^{-1}$.

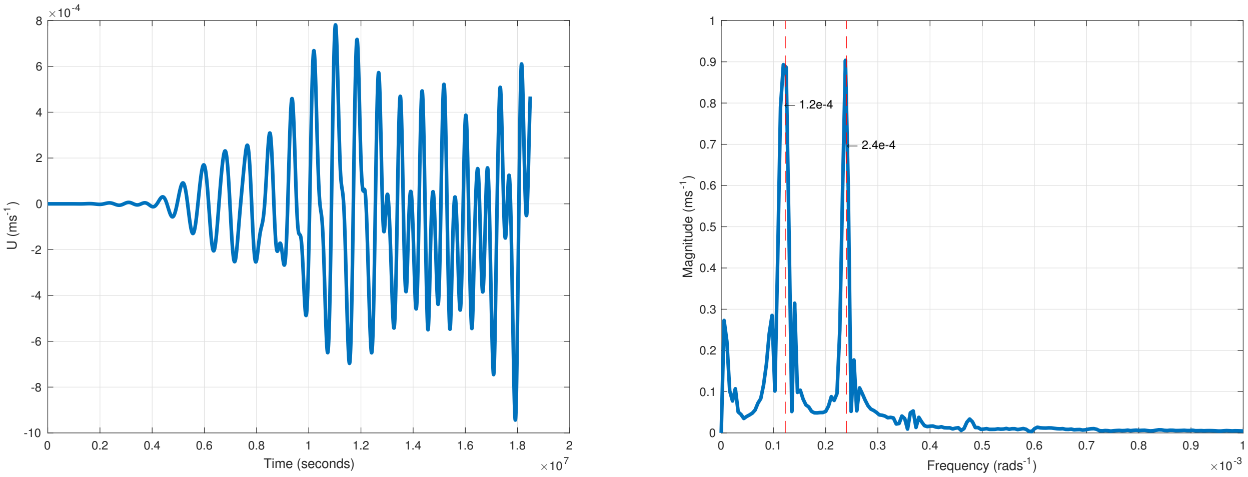

(a) Observed signal at mooring-2 (b) Frequency response at mooring-2

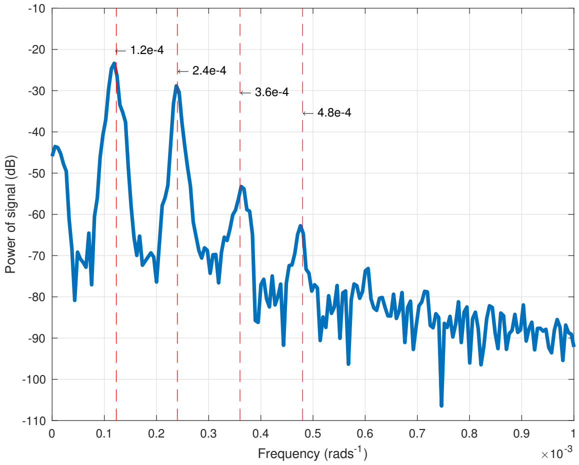

(c) PSD at mooring-2

Figure 4.32: Time series obtained from mooring **2** where the nonlinear interaction occurs. The frequency domain shows sharp peaks of about the same magnitude at the first and second harmonic frequency. We also observe a significant spectral line at the zero frequency value. From the power spectral density plot we see that most of the power in the time series is contained in the first and second harmonics. There is a significant signal at the third and fourth harmonic frequencies which are non-propagating.

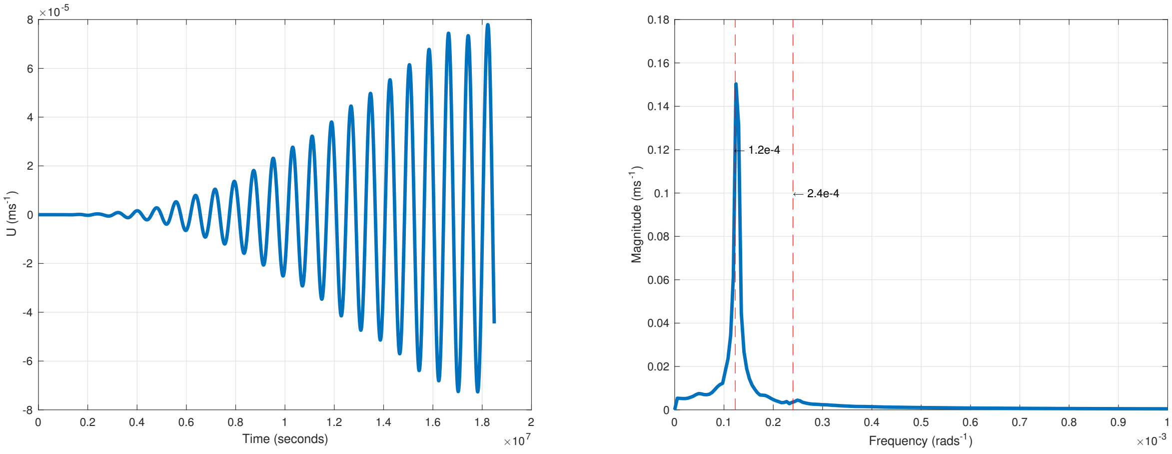

(a) Fig:4.10a Observed signal at mooring-3

(b) Frequency response at mooring-3

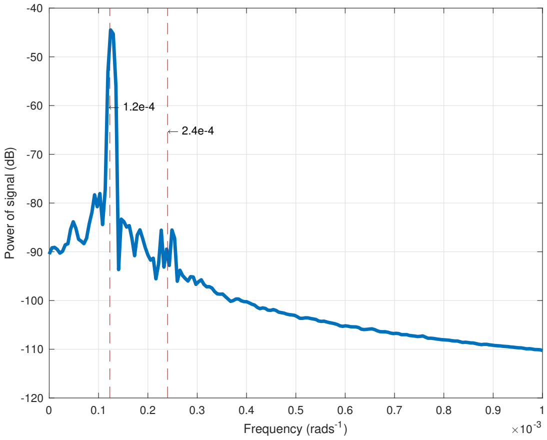

(c) PSD at mooring-3

Figure 4.33: Mooring **3** (Figure (4.30)) is in the first harmonic reflected beam with frequency ω. The time domain plot shows an increasing amplitude of the horizontal current in this region which decays in time. The frequency response and power spectral density estimate show that the first harmonic frequency ω is the dominant frequency.

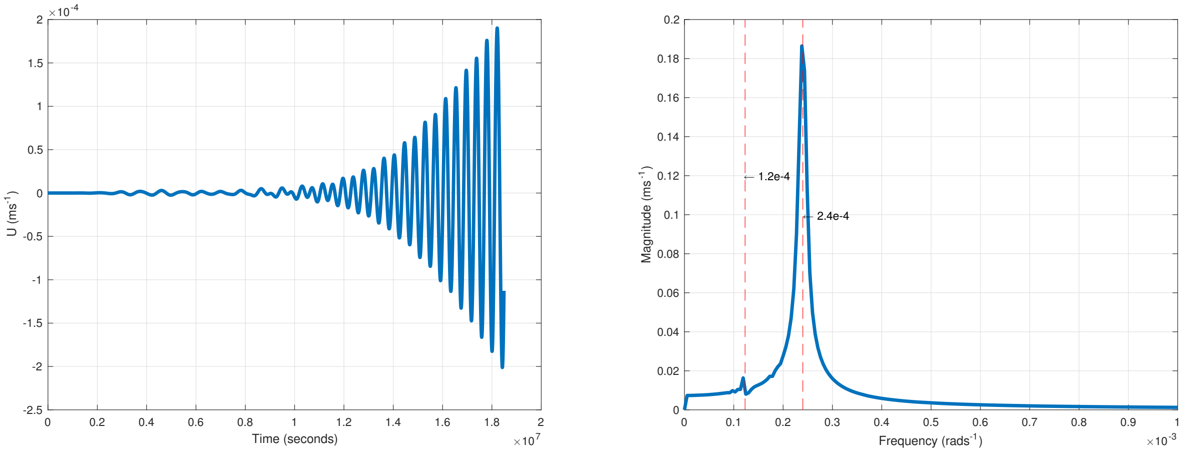

(a) Observed signal at mooring-4

(b) Frequency response at mooring-4

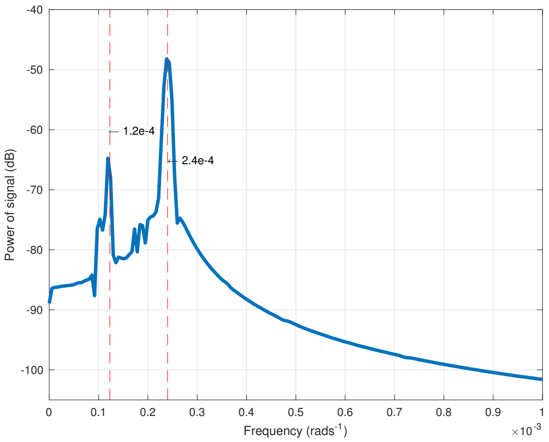

(c) PSD at mooring-4

Figure 4.34: The dominant frequency at Mooring-**4** is the second harmonics. This beam was generated by the nonlinear interaction of the incident and reflected first harmonic beams. The frequency response shows a dominant spectral line at the second harmonic frequency $2\omega = 2.4 \times 10^{-4}\mathrm{rad\,s^{-1}}$.

4.5 Colliding Beams as a Time Series

In this section we are interested in determining dominant frequencies for some cases of colliding beams. The aim is to check dominant frequencies and also to observe how beams of varying frequencies interact and how these frequencies are distributed among the generated harmonics. Moorings at several locations in the internal wave beams are used to obtain time series data which we analyse using Fourier methods. The arrows on each figure indicate mooring locations. At the region where the two beams collide we present both the frequency response and the power spectral density. For all other cases only the frequency response is shown.

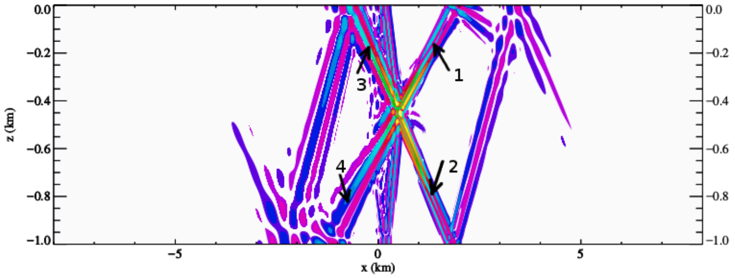

Figure 4.35: Numerical simulation showing collision of two internal wave beams. Parameter values are $\omega_1 = 1.2 \times 10^{-4} \mathrm{rad\,s^{-1}}$, $\omega_2 = 1.8 \times 10^{-4} \mathrm{rad\,s^{-1}}$, $N = 3.3 \times 10^{-4} \mathrm{rad\,s^{-1}}$.

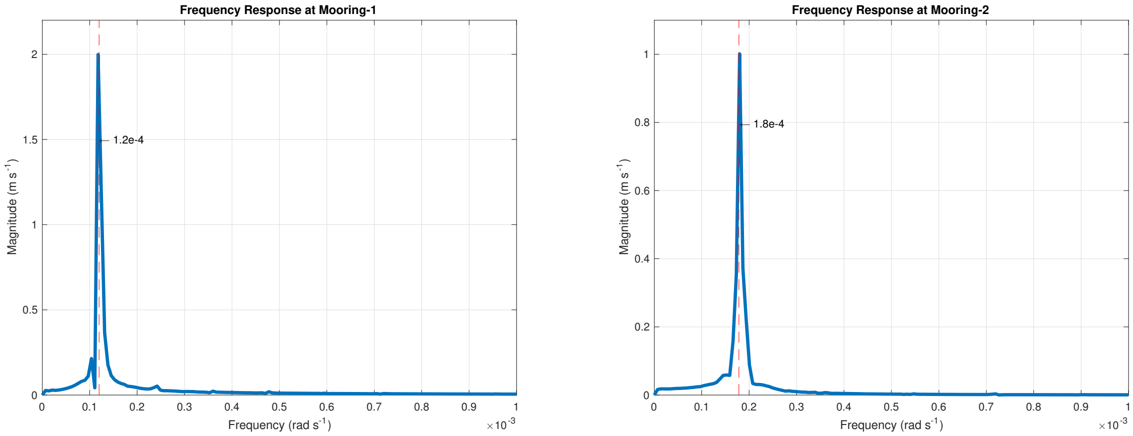

(a) Frequency response at Mooring 1

(b) Frequency response at Mooring 2

Figure 4.36: Magnitude of frequency response before collision for figure (4.35).

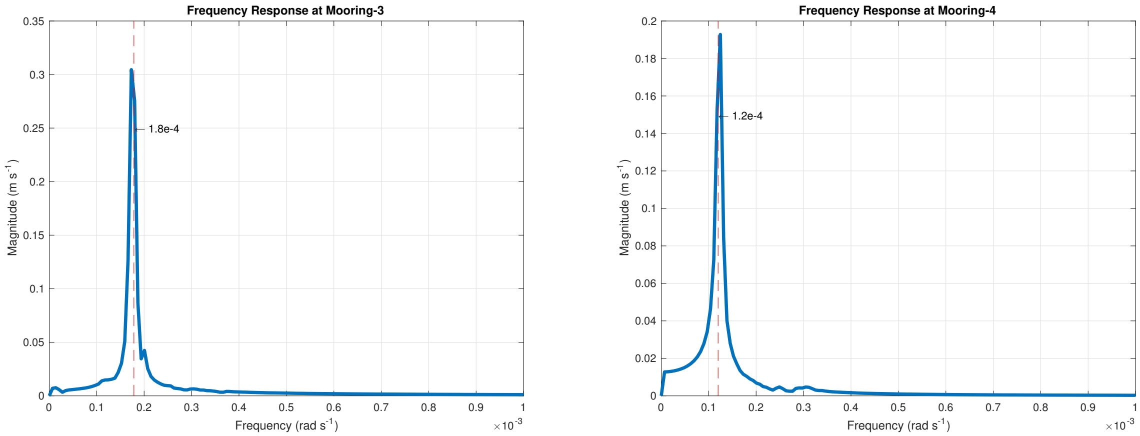

(a) Frequency response at Mooring 3

(b) Frequency response at Mooring 4

Figure 4.37: Magnitudes of frequency response after collision for figure (4.35).

We see that the dominant frequencies are not altered after collision, however the magnitude of the frequency of each of the colliding beams decreases after collison. This may be attributed to numerical dissipation and shear at the region of collision as well as energy loss due to the nonlinear transfer to other beams.

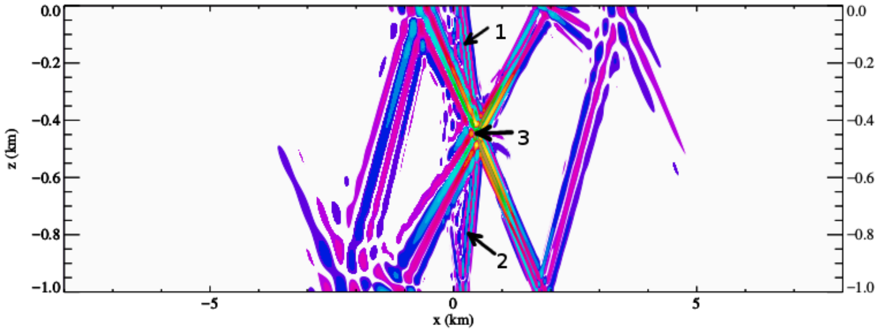

Figure 4.38: Parameter values are $\omega_1 = 1.2 \times 10^{-4} \mathrm{rad\,s^{-1}}$, $\omega_2 = 1.8 \times 10^{-4} \mathrm{rad\,s^{-1}}$, $N = 3.3 \times 10^{-4} \mathrm{rad\,s^{-1}}$.

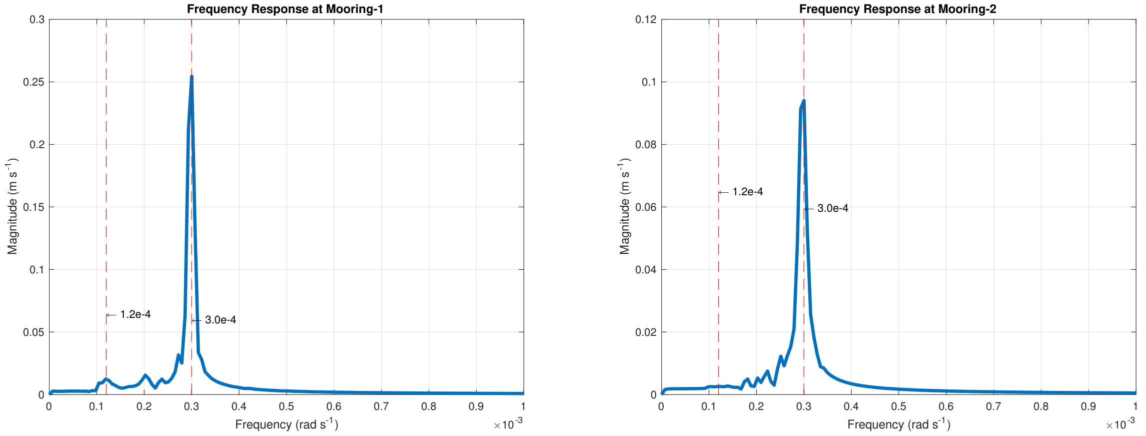

(a) Frequency response at Mooring 1

(b) Frequency response at Mooring 2

Figure 4.39: Magnitude of the frequency response at moorings **I** and **II**, for figure (4.38). Peaks occurring at the second harmonic frequency.

The dominant frequency at moorings **I** and **II** is the second harmonic frequency which is equal to the sum of the individual frequencies of the interacting wave beams. The second harmonic beams were generated from the nonlinear interaction of the incident beams. The frequency response at the region marked **3** where nonlinear interaction occur show peaks at frequencies corresponding to the incident wave beam frequency and second harmonic frequency. Also we see peak corresponding to $(\omega_2 - \omega_1)$ frequency, however, this component

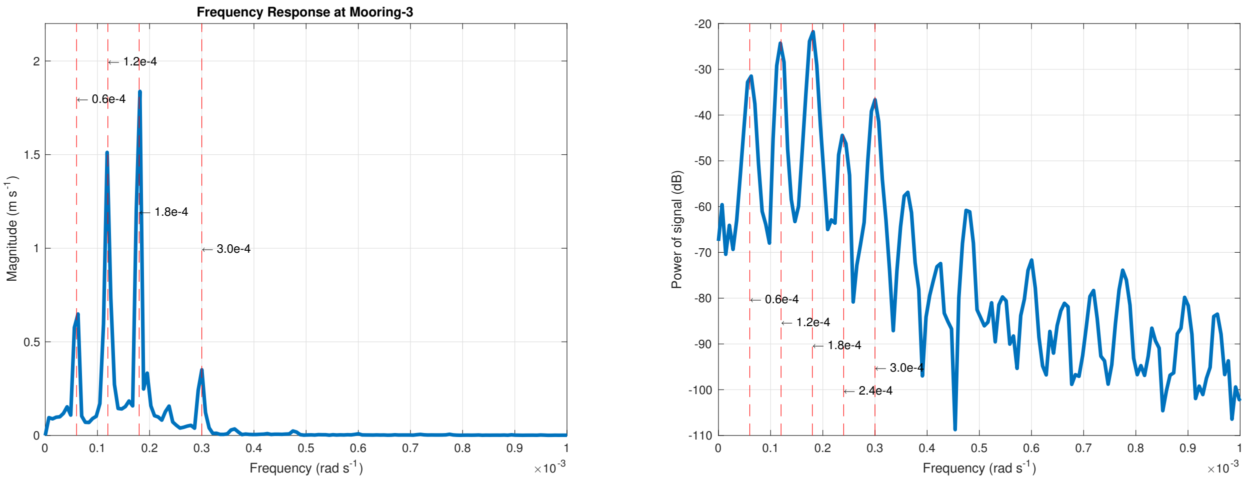

(a) Frequency response at Mooring 3

(b) PSD at Mooring 3

Figure 4.40: Magnitude of the frequency response and the power spectral density at mooring **3** for figure (4.38). This is the region where the nonlinear interaction occur. Peaks corresponding to dominant frequencies can by seen from the two figures. The power spectral density gives a clearer indication of the harmonics present in this region.

does not propagate because its frequency is less than the minimum frequency $\omega_{\min}$ for wave propagation.

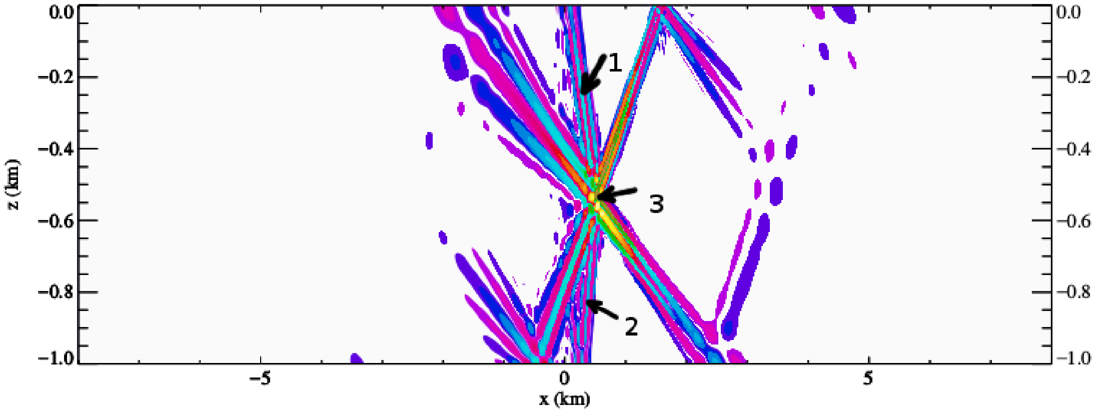

Figure 4.41: Parameter values are $\omega_1 = \omega_2 = 1.4 \times 10^{-4}\mathrm{rad\,s^{-1}}$, $N = 3.0 \times 10^{-4}\mathrm{rad\,s^{-1}}$. Arrows indicate where the moorings are located.

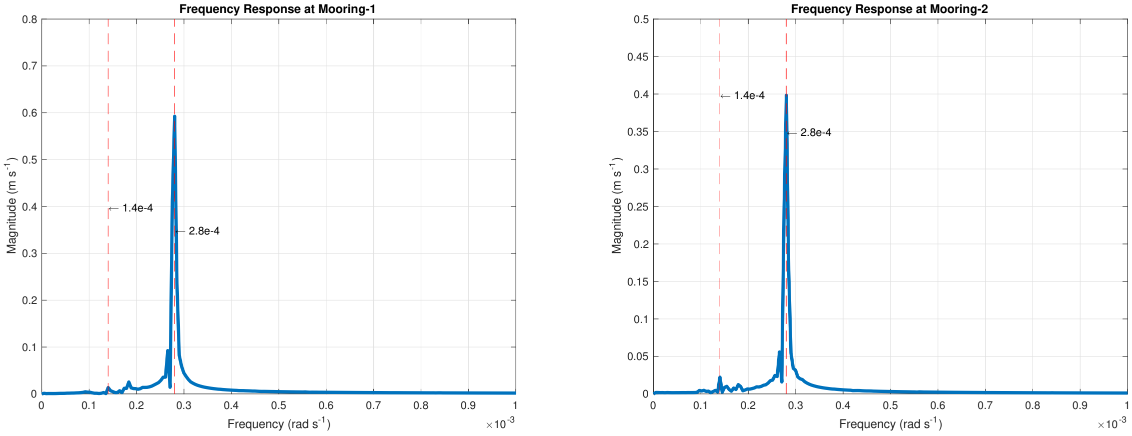

(a) Frequency response at Mooring 1

(b) Frequency response at Mooring 2

Figure 4.42: Spectra for figure (4.41). The dominant frequency component is the second harmonic with frequency $\omega = 2.8 \times 10^{-4}\mathrm{rad\,s^{-1}}$. There is some influence from the first harmonic as we see from the two plots but this is relatively negligible.

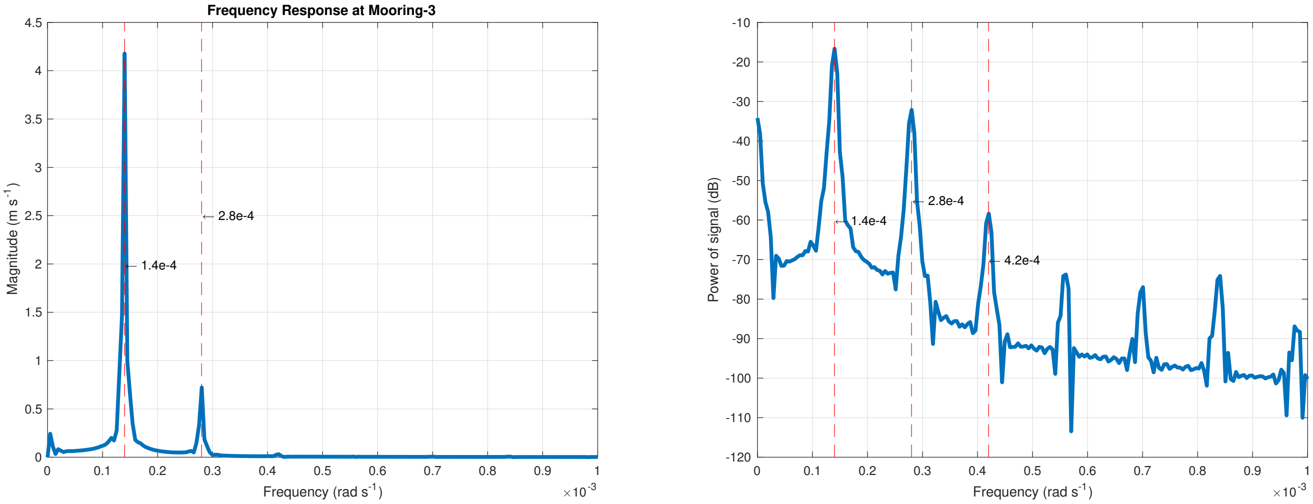

(a) Frequency response at Mooring 3

(b) PSD at Mooring 3

Figure 4.43: Spectra for figure (4.41). In the frequency domain we observe two peaks corresponding to the first and second harmonics. From the power spectral density we can observe contributions up to the 7th harmonics. Thus nonlinear interaction of beams is not restricted to first and second harmonics, but also involves higher harmonics.

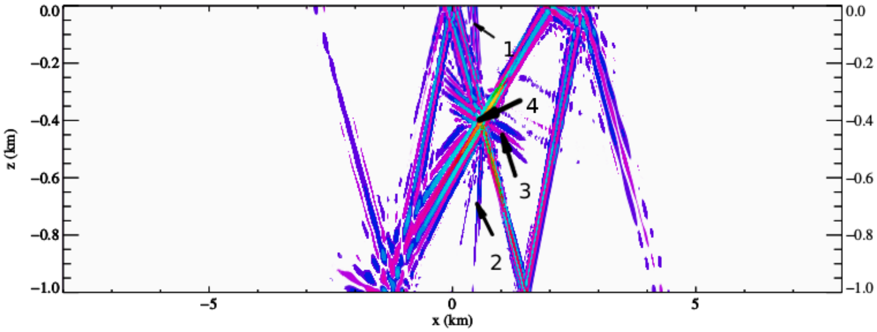

Figure 4.44: Numerical simulation of colliding beams for which the forcing frequency of one of the beams is twice the other. The beam propagating from quadrant **I** has frequency $\omega_1 = 1.2 \times 10^{-4}\mathrm{rad\,s}^{-1}$, while the beam propagating from quadrant **IV** has frequency $\omega_2 = 2.4{\times}10^{-4}\mathrm{rad\,s}^{-1}$, $N = 3.65{\times}10^{-4}\mathrm{rad\,s}^{-1}$, $f = f_h = 1.0338{\times}10^{-4}\mathrm{rad\,s}^{-1}$, $m_1 = \frac{2\pi}{30}\mathrm{m}^{-1}$, $m_2 = \frac{2\pi}{50}\mathrm{m}^{-1}$, $a = 10\mathrm{m}$, $b = 200\mathrm{m}$.

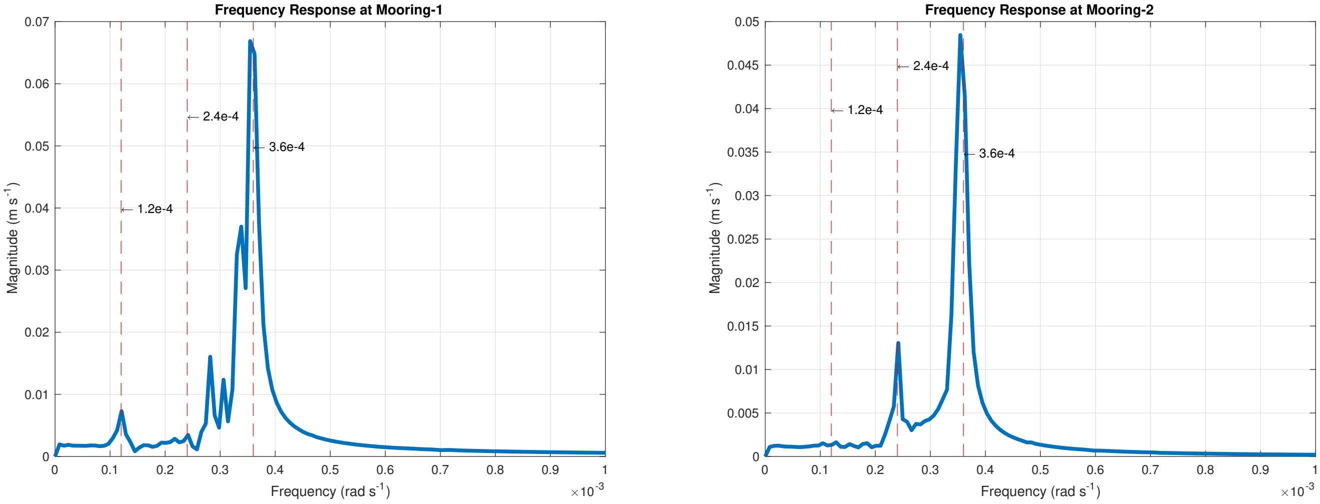

(a) Frequency response at Mooring 1

(b) Frequency response at Mooring 2

Figure 4.45: Again the dominant frequency component from moorings 1 and 2 is the second harmonic frequency which corresponds to $\omega_1 + \omega_2$.

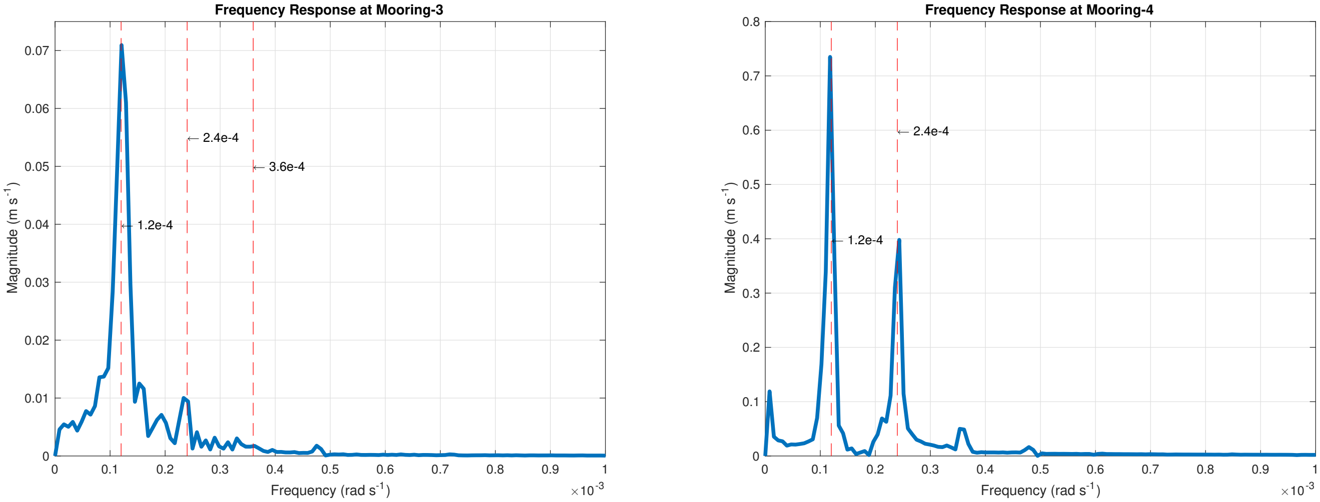

(a) Frequency response at Mooring 3

(b) Frequency response at Mooring 4

Figure 4.46: Frequency response at morings **3** and **4**. Mooring **3** is located at the region occupied by waves of frequency $\omega_2 - \omega_1$. Waves at this frequency propagate away from the generation site because it is within the interval of allowable frequencies. At the 4th mooring where nonlinear interaction occur the dominant frequencies are the first and second harmonic frequencies. The first harmonic exerts greater influence than the second harmonic, due to the extra contribution from the $(\omega_2 - \omega_1)$ waves.

Chapter 5

Conclusion

5.1 Summary

In this thesis, an account of nonlinear interaction of internal waves in the ocean without the traditional approximation is presented. A number of comparisons between the traditional and non-traditional approximation were made with respect to dispersion relation, group velocity, phase speed and beam slope. We saw that making the non-traditional approximation modifies the dynamics of internal waves due to changes to the dispersion relation. Certain peculiarities were made for the non-traditional approximation for example, non-traditional effects are more pronounced for near inertial waves and for weak stratification. In terms of slope orientation it was observed that non-traditional effect decreases the critical slope of wave beams (making it less steep) for slopes oriented northwards and increases the critical slope (making it steeper) for slopes oriented southwards. We also observed that in the non-traditional regime waves exist at inertial and sub-inertial frequencies.

Reflection of internal waves from flat and sloping boundaries and the generation of second harmonic wave beams in the process was treated and tested using numerical simulations. It was observed that due to the non-traditional (f_h) term colliding beams of equal frequencies propagating along ξ and η characteristics do not possess the same amount of energy. We also discussed the generation of higher harmonics from colliding beams. We found that when internal wave beams undergo nonlinear interaction higher harmonics with frequency equal to the sum of the frequencies of the individual incident beams is generated. The generation of these higher harmonics depend on the collision configuration of the incident beams. For example beams with horizontal group velocity of the same sign generate second harmonics after collision while wave beams with vertical group velocity of the same sign do not. A formation rule governing this process is presented. In all of the numerical simulations, the vertical (f) and horizontal (f_h) Coriolis parameters were assumed to be equal. This was guaranteed by fixing the angle of latitude $\theta = \frac{\pi}{4}$ radians and also fixing the angle the x-axis is rotated at $\phi = \frac{\pi}{2}$ radians. We observed that the width of sub-inertial range becomes smaller for smaller values of f_h and for stronger stratification. Secondly, negative slope topography generally reduces the group velocity of first and second harmonic reflected super-inertial waves. However in inertial and sub-inertial waves negative slope bottom topography increases the group velocity of the first harmonic reflected wave but reduces that of the second harmonic.

Spectral analysis of wave beams in the frequency domain was carried out to determine dominant frequencies. Internal wave spectra for several numerical simulations with different parameter settings were plotted. Sharp peaks indicate dominant frequencies. For some cases of reflection from a flat bottom and colliding wave beams, power spectral densities were determined using the method developed by Peter D. Welch in 1967 to observe the distribution of power at a number of locations in the flow field as a function of frequency. It was observed that colliding beams retain the dominant frequency after collision but with a reduced magnitude. Secondly, at the region where beams collide higher harmonics are generated, however only the harmonics that fall within the allowable frequencies are allowed to propagate away from this region of nonlinear interaction.

5.2 Future Work

- Only cases for which $f = f_h$ are tested using numerical simulations. Cases with $f \neq f_h$ could be investigated.
- Viscosity can be included in the equations of motion for purpose of comparison with already obtained results. Moreover, to adequately treat the notion of critical reflection it is imperative to include viscous effects.
- We have basically considered only the generation of second harmonics, higher harmonics may also be accounted for by considering the interaction of the primary and secondary waves. Numerical simulations can then be performed to see how these higher harmonics are generated.
- One particular forcing Ψ function was adopted in the simulations done to generate the wave beams. Other Ψ routines for example using the Gaussian profile can be used to see how this compares with the results obtained.

- In all of the numerical simulations presented in this thesis we have used three values of the slope, $\beta = 0, -0.02, -0.06, -0.1$. The topography in reality is more complicated and not usually uniform. Different slopes can be used to see how the group velocity and phase speed differ with changing values of β.
- In the section on colliding beams we have only considered two radiation conditions. As part of future work the remaining radiation conditions could be addressed using theoretical arguements and numerical simulations.

References

[1] A Azevedo, JCB Da Silva, and AL New. On the generation and propagation of internal solitary waves in the southern bay of biscay. *Deep Sea Research Part I: Oceanographic Research Papers*, 53(6):927–941, 2006.

[2] SI Badulin, VM Vasilenko, and MI Yaremchuk. Interpretation of quasi-inertial motions using megapoligon data as an example. *Izv. Atmos. Oceanic Phys*, 27(6):446–452, 1991.

[3] John B Bell, Phillip Colella, and Harland M Glaz. A second-order projection method for the incompressible navier-stokes equations. *Journal of Computational Physics*, 85(2):257–283, 1989.

[4] John B Bell and Daniel L Marcus. A second-order projection method for variable-density flows. *Journal of Computational Physics*, 101(2):334–348, 1992.

[5] ST Cole, DL Rudnick, BA Hodges, and JP Martin. Observations of tidal internal wave beams at kauai channel, hawaii. *Journal of Physical Oceanography*, 39(2):421–436, 2009.

[6] Thomas M DeCarlo, Kristopher B Karnauskas, Kristen A Davis, and George TF Wong. Climate modulates internal wave activity in the northern south china sea. *Geophysical Research Letters*, 42(3):831–838, 2015.

[7] David Farmer, Qiang Li, and Jae-Hun Park. Internal wave observations in the south china sea: The role of rotation and non-linearity. *Atmosphere-Ocean*, 47(4):267–280, 2009.

[8] Lee-Lueng Fu. Observations and models of inertial waves in the deep ocean. *Reviews of Geophysics*, 19(1):141–170, 1981.

[9] Chris Garrett. Oceanography: Mixing with latitude. *Nature*, 422(6931):477–477, 2003.

[10] Chris Garrett and Louis St Laurent. Aspects of deep ocean mixing. *Journal of oceanography*, 58(1):11–24, 2002.

[11] T Gerkema. Internal-wave reflection from uniform slopes: higher harmonics and coriolis effects. *Nonlinear Processes in Geophysics*, 13(3):265–273, 2006.

[12] Theo Gerkema, Frans-Peter A Lam, and Leo RM Maas. Internal tides in the bay of biscay: conversion rates and seasonal effects. *Deep Sea Research Part II: Topical Studies in Oceanography*, 51(25):2995–3008, 2004.

[13] Theo Gerkema and Victor I Shrira. Near-inertial waves in the ocean: beyond the traditional approximation. *Journal of Fluid Mechanics*, 529:195–219, 2005.

[14] Theo Gerkema and Victor I Shrira. Non-traditional reflection of internal waves from a sloping bottom, and the likelihood of critical reflection. *Geophysical research letters*, 33(6), 2006.

[15] Theo Gerkema, Chantal Staquet, and Pascale Bouruet-Aubertot. Decay of semidiurnal internal-tide beams due to subharmonic resonance. *Geophysical Research Letters*, 33(8), 2006.

[16] Karl R Helfrich and WK Melville. On long nonlinear internal waves over slope-shelf topography. *Journal of Fluid Mechanics*, 167(1):285–308, 1986.

[17] Wanjun Huang and Duncan L MacFarlane. Fast fourier transform and matlab implementation. *The University of Texas at Dallas. Dr. Duncan L. MacFarlane. Web*, 24, 2016.

[18] Chung-Hsiang Jiang and Philip Marcus. *Selection Rules for the Nonlinear Interactions of Internal Gravity Waves and Inertia-Gravity Waves.* PhD thesis, 2010.

[19] Chung-Hsiang Jiang and Philip S Marcus. Selection rules for the nonlinear interaction of internal gravity waves. *Physical review letters*, 102(12):124502, 2009.

[20] Alexander S Korobov and Kevin G Lamb. Interharmonics in internal gravity waves generated by tide-topography interaction. *Journal of Fluid Mechanics*, 611:61–95, 2008.

[21] Pijush K Kundu and Ira M Cohen. Fluid mechanics. *Academic Press: San Diego, CA*, 2008.

[22] Kevin G Lamb. Numerical experiments of internal wave generation by strong tidal flow across a finite amplitude bank edge. *Journal of Geophysical Research: Oceans*, 99(C1):843–864, 1994.

[23] Kevin G Lamb. A numerical investigation of solitary internal waves with trapped cores formed via shoaling. *Journal of Fluid Mechanics*, 451:109–144, 2002.

[24] Kevin G Lamb and David Farmer. Instabilities in an internal solitary-like wave on the oregon shelf. *Journal of Physical Oceanography*, 41(1):67–87, 2011.

[25] KG Lamb. Nonlinear interaction among internal wave beams generated by tidal flow over supercritical topography. *Geophysical Research Letters*, 31(9), 2004.

[26] PH LeBlond and LA Mysak. Waves in the ocean, 602 pp, 1978.

[27] R-C Lien and MC Gregg. Observations of turbulence in a tidal beam and across a coastal ridge. *Journal of Geophysical Research: Oceans*, 106(C3):4575–4591, 2001.

[28] DE Mowbray and BSH Rarity. A theoretical and experimental investigation of the phase configuration of internal waves of small amplitude in a density stratified liquid. *Journal of Fluid Mechanics*, 28(1):1–16, 1967.

[29] Walter Munk. Once again: once againtidal friction. *Progress in Oceanography*, 40(1):7–35, 1997.

[30] Fridtjof Nansen. *The oceanography of the north polar basin*, volume 3. Longmans, Green, and Company, 1902.

[31] Gerald R North, John A Pyle, and Fuqing Zhang. *Encyclopedia of atmospheric sciences*, volume 1. Elsevier, 2014.

[32] Dirk J Olbers. Models of the oceanic internal wave field. *Reviews of Geophysics*, 21(7):1567–1606, 1983.

[33] Thomas Peacock and Ali Tabaei. Visualization of nonlinear effects in reflecting internal wave beams. *Physics of Fluids*, 17(6):061702, 2005.

[34] Bernard Saint-Guily. On internal waves. effects of the horizontal component of the earth's rotation and of a uniform current. *Deutsche Hydrografische Zeitschrift*, 23(1):16–23, 1970.

[35] Samantha A Siedlecki, Neil S Banas, Kristen A Davis, S Giddings, Barbara M Hickey, Parker MacCready, T Connolly, and S Geier. Seasonal and interannual oxygen variability on the washington and oregon continental shelves. *Journal of Geophysical Research: Oceans*, 120(2):608–633, 2015.

[36] Ali Tabaei, TR Akylas, and Kevin G Lamb. Nonlinear effects in reflecting and colliding internal wave beams. *Journal of Fluid Mechanics*, 526:217–243, 2005.

[37] Peter D Welch. The use of fast fourier transform for the estimation of power spectra: A method based on time averaging over short, modified periodograms. *IEEE Transactions on audio and electroacoustics*, 15(2):70–73, 1967.

[38] HP Zhang, B King, and Harry L Swinney. Experimental study of internal gravity waves generated by supercritical topography. *Physics of Fluids*, 19(9):096602, 2007.